DESIGN OF SOLID CATALYSTS FOR BIOMASS UPGRADING

A Dissertation
Presented to
The Academic Faculty

by

Sarah McNew Schimming

In Partial Fulfillment
of the Requirements for the Degree
Doctor of Philosophy in the
School of Chemical and Biomolecular Engineering

Georgia Institute of Technology
December 2014

DESIGN OF SOLID CATAYLSTS FOR BIOMASS UPGRADING

Approved by:

Dr. Carsten Sievers, Advisor
School of Chemical and Biomolecular Engineering
Georgia Institute of Technology

Dr. Charles Liotta
School of Chemistry and Biochemistry
Georgia Institute of Technology

Dr. Pradeep Agrawal
School of Chemical and Biomolecular Engineering
Georgia Institute of Technology

Dr. Francis Schork
School of Chemical and Biomolecular Engineering
Georgia Institute of Technology

Dr. Yulin Deng
School of Chemical and Biomolecular Engineering
Georgia Institute of Technology

Date Approved: August 20, 2014

To Brian for all of his support over the years.

ACKNOWLEDGEMENTS

I would like to thank my advisor, Dr. Carsten Sievers, for accepting me into his research group and for providing me with the resources I needed to learn and grow in graduate school. Without your input and knowledge, my graduate research career would not have been the same. I would also like to thank my Thesis Committee for all of their support and encouragement. I would like to thank the Sievers Group members who have helped me along the way, especially John Copeland, Ryan Ravenelle, Jessica Ewbank and Guo Shiou Foo. Assistance in the lab from John and Ryan was invaluable to my start into research, and their advice kept me from making countless mistakes early on. Jessica Ewbank helped me build at least one flow reactor from the start as well as Labview programming and troubleshooting help. Guo Shiou helped me with operation of the HPLC and the batch reactor. I would have surely been lost without all of your help. Not only have my lab group members provided me with research guidance, but they have become friends over the past four years. My research would not have been the same without the help of many other people including Michael König, Onaje LaMont, Tiorra Ross and Andrew D'Amico. I will always appreciate the support and contributions of the faculty, staff and students of Georgia Tech. I would like to thank the Institute of Paper Science and Technology for the Paper Science Fellowship as well as Norman Marsolan, Lloyd Williams for financial support.

I would also like to thank my family for all of their support during my time in graduate school. To my mother and father, thank you for all the love and support you provided while I furthered my education. To my brother, thank you for being a friend. I love you all very much.

TABLE OF CONTENTS

LIST OF TABLES

LIST OF FIGURES

LIST OF SYMBOLS AND ABBREVIATIONS

HDO	Hydrodeoxygenation
TPR	Temperature-programmed reduction
H_2-D_2	Hydrogen-Deuterium
FTIR	Fourier Transform Infrared
OSC	Oxygen Storage Capacity
XRD	X-ray Diffraction
SEM	Scanning Electron Microscopy
TEM	Transmission Electron Microscopy
HDS	Hydrodesulfurization
GC	Gas Chromatograph
HPLC	High Pressure Liquid Chromatograph
PIXE	Photon Induced X-ray Emissions
BJH	Barrett-Joyner-Halenda
BET	Brunauer-Emmett-Teller
TCD	Thermal Conductivity Detector
W/F	Weight to feed ratio
GC-MS	gas chromatograph-mass spectrometer
MS	mass spectrometer
EDX	energy dispersive x-ray spectroscopy

SUMMARY

Transportation fuels and many chemical precursors in the United States come from nonrenewable, petroleum sources. Petroleum is diminishing in supply and has negative environmental effects, so it is important to find alternative feedstocks to produce transportation fuels and chemicals. Ligno-cellulosic biomass is an attractive option because it is sustainable, carbon neutral and readily available. Heterogeneous catalysts, specifically metal oxides and supported metal oxides, have been used in petroleum refining successfully and are likely candidates for upgrading biomass to fuels and chemicals in a bio-refinery.

Bio-refineries have the potential to increase the economic viability of the biofuel industry. The purpose of a bio-refinery is to use a small fraction of the feedstock or by-products of biofuel synthesis to produce high value, small-market chemicals. Larger revenue from the bio-based chemicals can help to offset the cost of biofuel production, making it possible to synthesize more biofuels for a lower cost. Therefore, to make biofuels more cost effective in a bio-refinery, it is necessary to examine methods of improving biomass upgrading strategies to produce biofuels as well as value-added chemicals from by-products.

Biomass upgrading can be challenging due to its high oxygen content compared to coal or oil. Specifically, flash pyrolysis of biomass produces bio-oils, but the resulting product mixture has a low heating value, high polarity, high acidity and high viscosity compared to petroleum based fuels. Most of the unfavorable characteristics of pyrolysis oils are associated with oxygen containing compounds. One method of upgrading pyrolysis oils is hydrodeoxygenation (HDO). HDO can be performed using traditional hydrodesulfurization catalysts, which require metals and the use of toxic H_2S to stay catalytically active. Chapters 2 and 3 of the thesis focus on sulfur free, metal free catalyst design for biofuels produced from flash pyrolysis using hydrodeoxygenation.

Chapter 2 focuses on fundamental studies to characterize the properties that ceria-zirconia mixed metal oxides must possess to perform HDO. The two main requirements for oxide-based HDO catalysts are the presence of defect sites to bind oxygenates and the ability to adsorb and dissociate hydrogen. Defect site formation was characterized with temperature-programmed reduction (TPR) and oxygen storage capacity (OSC) measurements. Hydrogen-deuterium (H_2-D_2) exchange, at varying hydrogen and deuterium concentrations, was used to understand the kinetics of hydrogen adsorption/dissociation. Fourier Transform Infrared (FTIR) spectroscopy of H_2-D_2 exchange was used to identify surface species close to reaction conditions. It was found that a catalyst with 60 mol% ceria and 40 mol% zirconia had the largest quantity of exchangeable hydrogen at typical temperatures for HDO reaction. Two types of sites were identified for exchange of hydrogen and deuterium. The activation energy for one type of site was ~24 $kJ*mol^{-1}$ and was associated with H_2-D_2 exchange through oxygen defect sites. The activation energy for the second type of site was associated with H_2-D_2 exchange through hydroxyl groups and correlated with crystallite size.

Chapter 3 describes hydrodeoxygenation activity of ceria-zirconia mixed metal oxides and correlates the reactivity to characterization data. Ceria-zirconia can convert guaiacol, a model pyrolysis oil compound, with a high selectivity to phenol, an HDO product. The characterization methods discussed in the previous section were used to correlate reactivity with structure. The key property of highly active HDO catalysts was surface oxygen defect sites. Ceria-zirconia catalysts had a higher conversion of guaiacol to deoxygenated products as well as a higher selectivity towards phenol than pure ceria. They did not deactivate over the course of 72 hours on stream, whereas coking or the presence of water in the feed can cause serious decay of common HDO catalysts HDO. Therefore, ceria-zirconia catalysts are promising HDO catalysts for the first step of deoxygenation.

Upgrading by-products to value-added chemicals can also be achieved by removing oxygen containing functional groups. A common by-product in a bio-refinery is glycerol produced from bio-diesel. Currently, bio-diesel is more expensive to produce than traditional petroleum-based diesel, and the transformation of glycerol into a more valuable bio-based chemical could help improve the economics of bio-diesel production. Many metals supported on oxides have been studied in laboratory conditions for upgrading glycerol to ethylene and propylene glycol. However, they have been studied at neutral pH. Crude glycerol is basic, and in order for catalysts to be usable in a bio-refinery they must be stable in reaction conditions. The last chapter of this thesis focuses on hydrothermal stability of a typical catalyst used for upgrading crude glycerol in acidic or basic solutions.

Chapter 4 demonstrates synthesis and characterization of supported Ru/ ZrO_2 metal oxides, and the effects of exposure to acidic or basic environments at reaction temperature on structure and reactivity. Physicochemical properties of Ru/ZrO_2 were studied using x-ray diffraction (XRD), nitrogen physisorption, H_2 chemisorption, scanning electron microscopy (SEM) and transmission electron microscopy (TEM). Stability tests were conducted at reaction temperature in acidic and basic pHs and reactivity was compared between the fresh catalyst and hydrothermally treated samples. In this study, the ruthenium dispersion is greatly increased by hydrothermal treatment in acidic and basic pH without alterations to the surface area, pore volume, pore size or crystal structure. An increase in Ru dispersion showed an increase in the selectivity to propylene glycol relative to ethylene glycol. A decrease in total Lewis acid site concentration was correlated with a decrease in the ethylene glycol yield. The conclusions of this study indicate that stability of catalysts in realistic industrial environments is crucial to the design of catalysts for a reaction.

CHAPTER 1

INTRODUCTION

1.1 Biomass for the production of fuels and chemicals

Our culture relies heavily on the consumption of energy and chemicals for daily life, and our dependence is only increasing [1]. Currently, transportation energy and many chemicals and chemical precursors in the United States come from nonrenewable fossil fuel sources [2-5]. Approximately three-quarters of the world's energy consumption come from oil, coal and natural gas sources [5, 6]. As crude-oil reserves decrease, it becomes increasingly important to research alternative sources. In fact, the Biofuels Directive of the European Union (EU) requires 20% biofuel use relative to fossil-based fuels by 2020 [7].

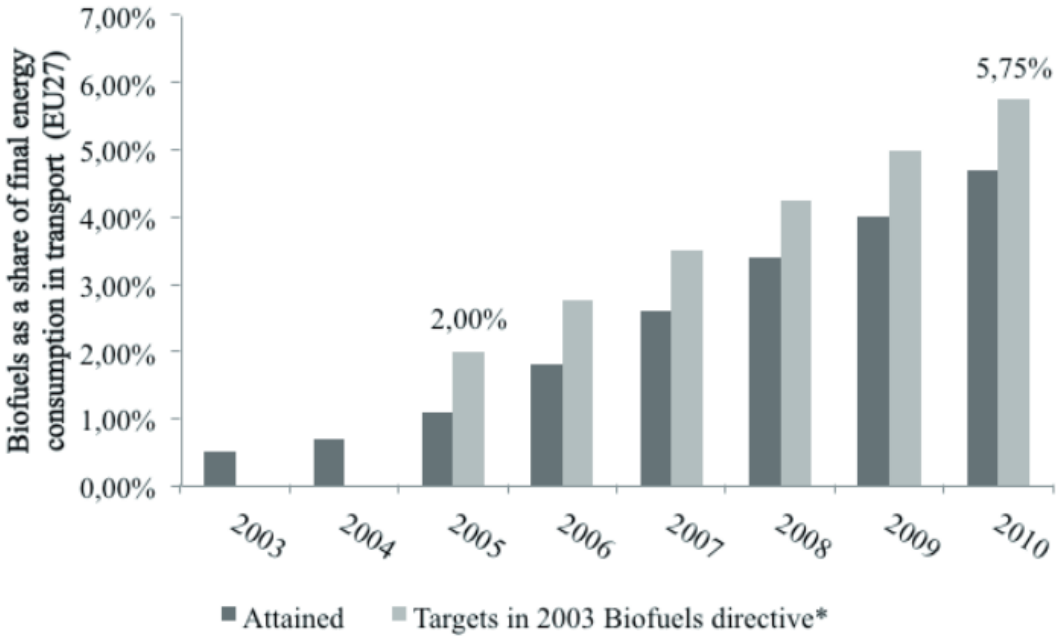

Figure 1.1 Biofuels as a share of final energy attained and targets up to 2010 [7].

Figure 1.1 shows the goals of the percentage of biofuels as a share of final energy up to 2010 along with the attained energy of the European Union. The goal for each year continues to rise, but the attained energy always falls short of the goal. Thus, it is important to increase production of biofuels, as well as research alternative sources to produce fuels and chemical precursors for a more sustainable economy [4, 8].

Current alternatives to nonrenewable energy sources are biomass (13%), hydropower (6%) and nuclear power (5%), which is approximately one-quarter of the world's primary energy consumption [5]. Of these alternatives, biomass is particularly promising because it can produce liquid fuels that can be combined and integrated into the current infrastructure, as well as be compatible with existing transportation technology. Many processes exist to convert biomass into fuels and chemicals, but implementing individual processes is not always cost effective and can create problems with the disposal of by-products. Thus, it has been recommended that the best solution to maximize economic benefits and minimize pollution and waste products is the implementation of a bio-refinery [9].

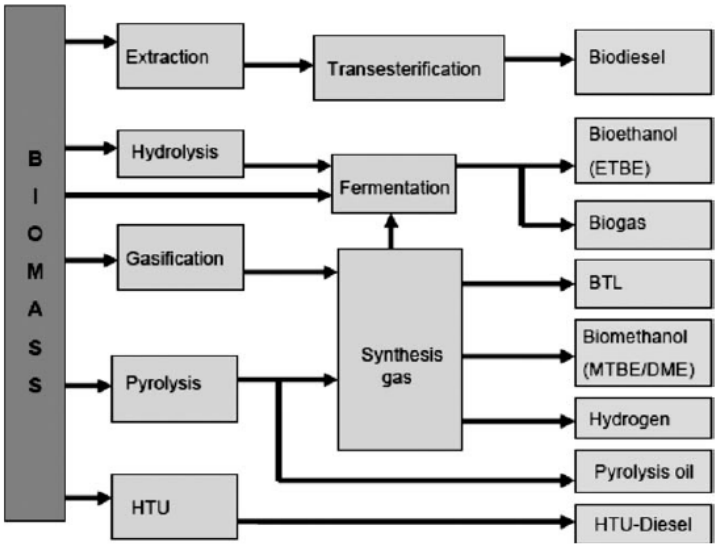

Figure 1.2 A simplified process flow diagram of a lingo-cellulosic bio-refinery [5].

Figure 1.2 shows a simplified process flow diagram of a ligno-cellulosic (non-edible biomass) bio-refinery. The purpose of a bio-refinery is to integrate multiple upgrading processes for the production of biofuels and chemicals in an economical way that would not be possible if the products were synthesized individually.

Biofuels currently commercially available are bioethanol and biodiesel. Both biodiesel and bioethanol can be used directly as a substitute for conventional fuels. Bioethanol has been used in Brazil as part of the National Alcohol Program (PRO-ALCOOL) that began in 1975 [10]. The PRO-ALCOOL was implemented to increase alcohol production for fuel purposes and establishes a minimum quality of ethanol-fuel blends. Currently, biodiesel is considered to be one of the most promising alternative fuels for petroleum derived diesel [11]. Biodiesel is produced via a reversible transesterification reaction to create methyl esters with glycerol as a by-product (Figure 1.3) [12].

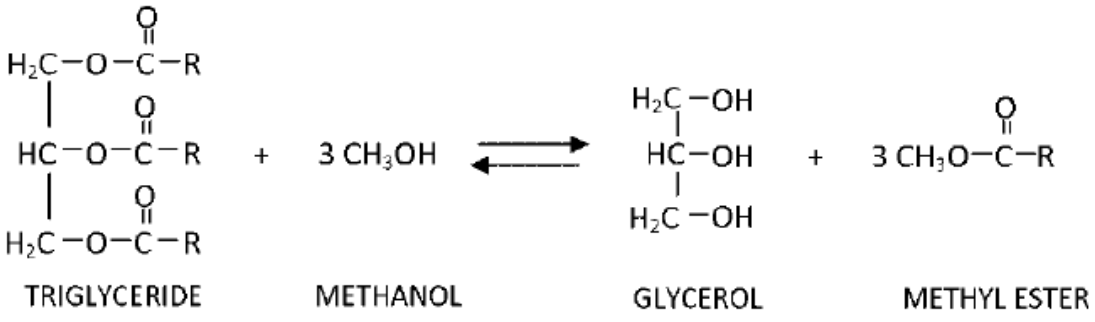

Figure 1.3 Biodiesel production reaction to produce methyl esters and glycerol [11].

As the demand for biodiesel increases, more will be produced. As more biodiesel is produced, more glycerol by-product is produced. Glycerol was identified by the Department of Energy (DOE) as a top-12 building block chemical that can be converted

to a high-value biomass derived chemical [13]. The removal of oxygen from glycerol through hydrogenolysis occurs through selective cleavage of a carbon-carbon or carbon-oxygen bond to produce ethylene glycol or propylene glycol [14]. Industrially, propylene glycol is a high added-value chemical that is primarily produced from nonrenewable petroleum based sources, and, it is highly desired to find an alternative production route [15]. Thus, it is important to study glycerol upgrading to improve the economics of a bio-refinery in an effort to make biodiesel production more cost effective.

Another method to produce biofuels in a bio-refinery is the thermochemical conversion of biomass. One example of thermochemical conversion of biomass is through fast pyrolysis into bio-oils [12]. Pyrolysis produces bio-oils by heating biomass in the absence of oxygen to temperatures of 375-525 °C and pressures of 1-5 atm. These bio-oils can be produced from any carbonaceous material including agricultural waste, sewage sludge and chicken litter, but they must be upgraded before use as a fuel [16]. Flash pyrolysis, the most economically feasible pyrolysis at an industrial level, occurs at the above conditions at a residence time of only a few seconds [17, 18]. As an energy densification technique, pyrolysis increases the ratio of energy to volume for a given feedstock [9, 19]. The initial products are gases, which then condense to a liquid product. These bio-oils are obtained in high yields of up to 80 wt% dry feed with 10-40 wt% oxygen and 10-30 wt% water depending on the feed [12, 20, 21].

Pyrolysis oils require the removal of oxygen to be useable as a fuel. Oxygen is removed from pyrolysis oils via hydrodeoxygenation (HDO). HDO has four basic requirements in a solid catalyst (Figure 1.4).

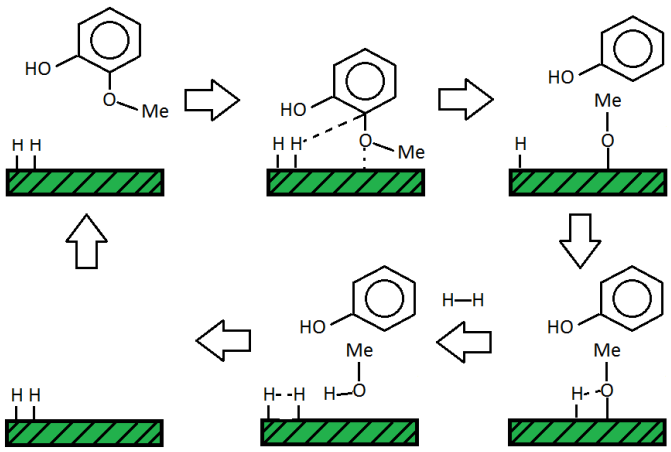

Figure 1.4 Possible mechanism for HDO of guaiacol over solid catalyst.

The first requirement is that the oxygen containing compound of interest must be able to attach the oxygen group to the surface of the catalyst. Once the oxygen is bound to the surface, hydrogen must be able to dissociate on the surface and break the oxygen-carbon bond. Next, compound of interest must detach from the surface with one less oxygen than it had previously. Finally, the catalyst must be able to remove the oxygen from the surface by combining it with hydrogen and leaving as water. If the catalyst is unable to regenerate itself, it is useless as a catalyst [14,15,19].

1.2 Development of catalysts for biomass conversion

Traditional hydrodesulfurization (HDS) catalysts that contain cobalt and nickel supported on alumina can be used for HDO [22, 23]. While these catalysts are well studied, they require the co-feeding of H_2S to remain in their active form. H_2S is highly toxic, explosive when mixed with air and can poison noble metal catalysts that could be downstream in a bio-refinery. Due to these reasons, it is important to design a sulfur-free catalyst for HDO. Supported noble metals can perform HDO, but they are expensive to

use on an industrial scale [16]. It is important to identify ways to decrease the cost of the catalyst used for HDO. This can be done by using cheaper metal oxides and by synthesizing metal free solid catalysts with high selectivity and conversion to HDO products. In order to design such catalysts, it is necessary to determine the appropriate characteristics of such catalysts and link them to reactivity. This will create a method to tune the properties of the catalysts to be highly selective for HDO products.

Another important aspect of catalyst design for use in bio-refineries is the stability of catalytic properties under the influence of realistic reaction conditions. Glycerol hydrogenolysis is well studied [15, 24-26]. However, as is common in literature, hydrothermal studies are carried out with pure glycerol in neutral pH environments. After a quick study, these catalysts are deemed stable under reaction conditions, and the issue is not readdressed over the course of the study. In reality, crude by-product streams, such as crude glycerol from biodiesel, have many impurities which alter the pH. Therefore, it is important to study the effects of pH on the stability of catalysts if they are to be implemented in a bio-refinery.

1.3 Characterization techniques for mixed metal oxides

Characterization of catalysts is important for design and synthesis. Reactions can be correlated with surface and bulk properties to allow for efficient design of future catalysts. Knowing how catalyst properties correlate with reactivity can help show what needs to be changed in the catalyst to improve reactivity and conversion. Reactivity and conversion are determined with product identification and quantification using a gas chromatograph (GC) and a high pressure liquid chromatograph (HPLC). The primary methods of characterization in this thesis are temperature-programmed reduction (TPR), measurements of oxygen storage capacity (OSC) and hydrogen-deuterium (H_2-D_2)

exchange [27, 28]. TPR and OSC are useful in determining the concentration of defect sites on the surface of the catalyst. However, it is important to note that the defect sites produced at or below the HDO reaction temperatures are the only ones that will be active for HDO. Another critical technique is H_2-D_2 exchange. H_2-D_2 exchange determines the availability of dissociated hydrogen on the surface of the catalyst, which is crucial for oxygen removal and the regeneration of defect sites on the surface of the catalyst. Other techniques used to characterize catalysts include N_2 physisorption, x-ray diffraction (XRD), infrared spectroscopy (IR), scanning electron microscopy (SEM), transmission electron microscopy (TEM) and H_2 chemisorption [29, 30].These characterization techniques are used to assign descriptors to physicochemical properties and correlate them with reactivity to identify methods of improvement in catalyst design.

1.4 Research objectives and tasks

The purpose of this work is to study the development of heterogeneous catalysts for oxygen removal reactions in a bio-refinery. The focus of the first two-thirds of the thesis is on upgrading pyrolysis oil via hydrodeoxygenation over ceria-zirconia mixed oxides. Chapter 2 is focused on the identification of key properties of HDO including hydrogen dissociation and oxygen defect site creation. Chapter 3 is focused on proof of concept of HDO over ceria-zirconia and the correlation of reactivity with catalyst structure. Chapter 4 is focused on the hydrothermal stability of Ru/ZrO_2, a typical glycerol hydrogenolysis catalyst, at acidic or basic pH. The effects of hydrothermal treatments on the catalyst on reactivity are examined. The goals of each section are outlined below.

Chapter 2. Characterization of defect sites and availability of dissociated hydrogen

Objective: Analyze the mechanism of hydrogen dissociation and defect site formation on mixed metal oxides:

- TPR and OSC to analyze dissociative adsorption of hydrogen and formation of defect sites
- H_2-D_2 exchange to determine the availability of surface hydrogen
- FTIR of H_2-D_2 exchange to identify surface species and their reactivity

Chapter 3. HDO of pyrolysis oil model compound over mixed metal oxide catalyst

Objective: Development of HDO catalysts that is easier and cheaper to synthesize than traditional HDS catalysts or supported metal catalysts:

- Synthesis and characterization of mixed metal oxides
- Reactivity test in trickle bed reactor with online GC sampling
- Determine kinetic parameters and reaction pathway of HDO of reactant
- Determine effect of reaction conditions on HDO reactions to achieve high conversion and selectivity

Chapter 4. Stability studies of Ru/ZrO_2 for glycerol hydrogenolysis

Objective: Development of metal supported on metal oxides for glycerol hydrogenolysis

- Synthesis and characterization of supported metal catalysts
- Stability studies in acidic and basic hydrothermal treatments
- Use batch reactor and HPLC to analyze products of glycerol test reaction
- Determine effects of hydrothermal treatments at different pH on structure and reactivity

CHAPTER 2

KINETICS OF HYDROGEN ACTIVATION ON CERIA-ZIRCONIA CATALYSTS

2.1 Introduction

Ceria can be used for a variety of catalytic reactions that involve Lewis acid-base sites, redox sites or a combination of these functionalities [31]. Acid-base reactions, such as ketonization, can be performed with pure ceria or with ceria supported on metal oxides like silica or titiania [32-34]. In addition to acid-base sites, redox sites are necessary for reactions like ethylbenzene dehydrogenation to produce styrene [31, 32]. The redox properties of cerium based oxides are also leveraged in three-way catalysts for automotive pollution control and fluid catalytic cracking due to the high affinity of ceria to oxygen and sulfur [31, 32, 35, 36]. Other applications of pure or supported ceria for redox reactions include selective hydrogenation reactions, oxidation of CO and toluene as well as catalytic wet oxidation of methane [37-39]. Ceria combined with gadolinium, copper, or yttrium stabilized zirconia has been extensively studied for alternative solid oxide fuel cells [40-43]. Often, ceria is utilized as a promoter or co-catalyst but not as the component responsible for the primary functionality. Many of these reactions involve supported metals such as ruthenium, palladium, gold, nickel or cobalt as well as a dopant such as zirconia or praseodymia to increase oxygen storage capacity and thermal stability and promote hydrogen dissociation and spillover [35, 37-47].

Pure ceria can also perform reactions with dissociated hydrogen in the absence of reduced metal particles. Selective hydrogenation of propyne to propene was observed on pure ceria at 1 bar and 250 °C [48]. The limiting factor in this selective hydrogenation reaction was thought to be availability of hydrogen on the surface, and the best catalyst

for the reaction was oxidized CeO_2, with no reductive pretreatment. It was proposed that some surface oxygen vacancies are necessary to stabilize dissociatively adsorbed hydrogen, but too many oxygen vacancies may result in complete hydrogenation of the reactant and reduced selectivity towards the desired product. Adsorbed hydrogen is also necessary for the reduction of ceria and the creation of anionic oxygen vacancies [49]. These sites are relevant in three-way catalysis, where oxygen is removed from NO_X to produce N_2 and O_2 [36].

Recent literature has shown that oxides with vacancies can catalyze hydrodeoxygenation of biomass-derived oxygenates [50, 51]. To design a highly efficient ceria-based catalyst for this reaction, it is important to obtain quantitative insight of the amount of reactive hydrogen on the surface under reaction conditions as well as the kinetics and types of active sites necessary for dissociative adsorption of hydrogen.

Doping ceria with zirconia is known to increase the oxygen storage capacity and to lower the temperature of surface and bulk reduction [52, 53]. During surface reduction with hydrogen, an oxygen atom is removed from the surface, and water is formed. When oxygen defect sites are present, hydrogen engages in interactions that are not observed without oxygen vacancies [54]. Thus, it is possible that the availability of hydrogen on reduced ceria-zirconia will exceed that on pure ceria in the same environment. Theoretical studies on oxygen vacancies in reduced ceria are not comprehensive because the added complexity of an additional metal in ceria-zirconia makes computational research much more difficult, resulting in a large deviation between computational and experimental data [55]. In an effort to quantify the number of oxygen vacancies, oxygen uptake has been studied. However, as most studies are motivated by automotive exhaust catalysis they typically do not contain experiments below 770 K [47].

The purpose of this study is to provide a comprehensive picture of hydrogen dissociation on ceria-zirconia catalysts and the influence of the composition and structure of these materials on their reactivity. The effect of composition and calcination

temperature of the catalysts on their performance is studied. The ability to dissociate hydrogen is described by the activation energies for isotopic hydrogen exchange and the amount of exchangeable hydrogen on the surface of each catalyst. Temperature-programmed reduction (TPR) and oxygen storage capacity (OSC) measurements are performed to analyze the consumption of hydrogen during reduction and quantify the number of oxygen vacancies that are formed below 450 °C. Finally, infrared spectroscopy is used to identify the sites contribution to hydrogen exchange activity at different temperatures.

2.2 Experimental

2.2.1 Chemicals

Cerium(III) nitrate hexahydrate (99% trace metals basis), zirconyl (IV) oxynitrate hydrate (99% trace metals basis) and ammonium hydroxide (A.C.S regent grade, 28-30% NH_3 content) were purchased from Sigma Aldrich. Gases (hydrogen, argon, helium and oxygen) with ultra-high purity (UHP Grade 5) were purchased from Airgas. Deuterium was purchased from Cambridge Isotope Laboratories, and the dry air was generated in house using a Parker Balston Gas Generator 1000. Deionized water was obtained from a Barnstead NANOpure ultrapure water system which purified to 18.2 MΩ/cm.

2.2.2 Catalyst synthesis

All catalysts were prepared by coprecipitation or precipitation of the precursors [56]. Cerium nitrate hexahydrate and zirconyl nitrate hydrate were dissolved in deionized water to form a 0.1 M solution. The coprecipitation or precipitation was performed by adding the 0.1 M precursor solution drop-wise to an aqueous ammonium hydroxide solution while stirring continuously. The precipitate was filtered, rinsed with deionized

water, and dried in an oven overnight at 100 °C. The catalysts were calcined for 4 hours in 200 mL/min zero grade air at 500 °C, 700 °C or 900 °C with a heating rate of 5 K/min.

2.2.3 Catalyst characterization

To determine the composition of each catalyst, proton induced x-ray emission **(**PIXE) analysis was performed by Elemental Analysis Inc. with a 95% confidence interval. Powder x-ray diffraction (XRD) patterns were measured on a Philips X'pert diffractometer equipped with an X'celerator module using Cu Kα radiation. Diffractograms were obtained for the range 2θ = 10-90° with a step size of 0.0083556°. The inter-planar spacing was calculated using the Bragg equation with a wavelength of 1.54 Å. The crystallite size was calculated using the Scherrer equation for the (111), (200), (220) and (311) planes and averaged to reduce the experimental error [57-59]. Nitrogen physisorption was performed on a Micromeritics ASAP2020 physisorption analyzer. For each sample, a quantity of ca. 0.150 g was degassed under vacuum at 200 °C for 4 hours. The Brunauer-Emmet-Teller (BET) surface area was calculated from the adsorption isotherm of nitrogen in the $0.05 \leq P/P_0 \leq 0.3$ pressure range [60]. Pore volumes were calculated from the adsorption branch using the Barrett-Joyner-Halenda (BJH) method [61]. Temperature programmed reduction (TPR) measurements were performed on a Micromeritics Autochem II 2920 using ca. 0.200 g of each catalyst. The catalysts were heated to 450 °C in flowing helium at 10 K/min and held at 450 °C for 1 hour before cooling to 0 °C at 15 K/min. Using a heating rate of 10 K/min, the catalysts were heated to 1000 °C in a 10 mol% hydrogen blend (argon balance), and the gas exiting the reactor was monitored using a thermal conductivity detector (TCD). A blank run with a pure helium flow was performed to ensure that the baseline TCD signal was zero over the entire temperature range. Oxygen storage capacity (OSC) measurements

were also performed on a Micromeritics Autochem II 2920 using ca. 0.200g of catalyst. The catalyst was heated to 450 °C while flowing a 10 mol% oxygen blend (helium balance). The sample was held at this temperature for an hour before being cooled to 200 °C, 300 °C or 450 °C. A 10 mol% hydrogen blend (argon balance) was used to reduce the sample. The sample temperature was held at 200, 300 or 450 °C for 30 minutes after which 10 mol% O_2 in He was pulsed over the sample until saturation (3 consecutive peaks of approximately equal area).

2.2.4 H_2-D_2 exchange experiments

The amount of exchangeable surface hydrogen was determined using a custom built flow reactor setup (Figure A.1). A fixed bed of ca. 200 mg of catalyst was placed on quartz wool in a quartz reactor. Gases were supplied by mass flow controllers (Brooks SLA5850s for hydrogen and deuterium and Brooks 4800 for argon). The composition of the gas stream was analyzed downstream by a Stanford Research Systems QMS300 gas analyzer. The partial pressures corresponding to mass to charge ratios recorded of 2 (H_2), 3 (HD) and 4 (D_2) were recorded over time. The mass flow controllers, a pressure transducer and the mass spectrometer were controlled by a custom made Labview program.

Prior to the isotopic exchange studies, the catalyst was pretreated in 5 vol% H_2 in argon at 450 °C for 1 hour. The catalyst was cooled slowly in flowing 5 vol% H_2 in argon to ensure that the surface of the catalyst remained in the reduced state. Once the temperature reached 110 °C, the gases were switched to 10 vol% D_2 in argon until a steady partial pressure of D_2 was measured. The quantity of deuterium consumed in this step is the amount of deuterium necessary to replace all exchangeable hydrogen on the surface of the catalyst. Next, the reactor was flushed with argon until no D_2 or H_2 was detected by the mass spectrometer. This indicated that all remaining H_2 and D_2 in the gas

stream had been removed, and any remaining hydrogen or deuterium must be present on the catalyst surface. Then, 10 vol% H_2 in argon was flowed over the catalyst to quantify the amount of deuterium present on the surface. The quantity of hydrogen consumed in this step is the amount of hydrogen necessary to replace all deuterium on the surface of the catalyst. The gas feed was switched to pure argon to flush the reactor as it was heated to 225 °C. The above steps were repeated at 225 °C and again at 325 °C. At the end of the experiment, the catalyst was heated to 800 °C in 5 vol% H_2 and 5 vol% D_2 in argon to reach equilibrium conversion, which served as a point for the calibration of the mass spectrometer (Figure A.2) [62]. A baseline for each mass to charge ratio was taken by flowing the reactant stream through an empty tube with quartz wool at room temperature.

The kinetics of H_2-D_2 exchange were studied using the same sample mass and activation procedure as described above. Once the activated catalyst had cooled to 30 °C, it was heated at 2 K/min to 800 °C in 5 vol% hydrogen and 5 vol% deuterium in argon (100 mL/min total flow) and the composition of the product stream was analyzed as a function of temperature.

2.2.5 In situ FTIR spectroscopic studies of H_2-D_2 exchange

In-situ FTIR experiments were performed on a Nicolet 8700 IR spectrometer with a MCT/A detector. For each spectrum, 64 scans were recorded at a resolution of 4 cm^{-1}. Each sample was pressed into a self-supported wafer and loaded into a vacuum transmission IR chamber. The sample was heated to 450 °C in vacuum at less than 10^{-6} mbar, and the chamber was filled with 10 mbar of H_2. Every 15 min, the chamber was evacuated and 10 mbar of H_2 were admitted to ensure that the sample was thoroughly reduced. After 1 hour, the chamber was evacuated again and the temperature was reduced to 350 °C. A spectrum of the activated sample was taken. D_2 was introduced at a pressure of 10 mbar for H_2-D_2 exchange to occur, and a spectrum was taken every 120 seconds for

1 hour. The experiment was repeated for H_2-D_2 exchange at 150 °C (after activation at 450 °C) with a new sample. All spectra were normalized by the area density of the wafer.

2.3 Results

2.3.1 Composition and morphology of catalysts

The physiochemical properties of all catalysts are summarized in Table 2.1. The abbreviations for the mixed metal oxides are defined based on their elemental composition as determined by PIXE analysis. Besides cerium, zirconium, and oxygen only a small amount of hafnium was detected (less than 0.3 mol% in all samples). Hafnium is a common impurity in zirconium precursors [63].

The morphology of all samples was characterized by N_2 (Figure A.3). The isotherm shapes of the pure oxides are quite different qualitatively indicating that pure zirconia had a higher surface area while pure ceria had larger pore volume (Table 2.1). Isotherms for the samples with more than 40% zirconia content exhibited hysteresis loops similar to a *Type H2* hysteresis [64], which is indicative of rapid desorption due to changes in the properties of the adsorbed fluid [65]. Therefore, only the adsorption branches of the isotherms were used for the BJH calculations. The desorption branches were excluded to avoid an artifact "pore" around 4.0 nm.

When the calcination temperature of Ce60 was increased, larger pores were formed, and the overall porosity of the material decreased (Table 2.1). The most notable changes occurred between 500 °C and 700 °C, but increasing the calcination temperature to 900 °C further affected the material. The average pore size increased from 2.7 nm to 4.3 nm, approximately 59%. The total pore volume increased by 74% when the calcination temperature was increased from 500 °C to 900 °C. The higher-temperature calcination decreased the surface area by 67% between 500 °C and 900 °C (Table 2.1).

Table 2.1 Physiochemical properties of different catalysts[a].

Composition of Mixed Oxide[b]	Abbreviation	BET surface area (m^2*g^{-1})	Pore width (nm)	Pore volume (cm^3*g^{-1})	Crystallite size (nm) [e]	Lattice parameter (Å) [e]
CeO_2	Ce100	63	9.3	0.123	9.3	2.34
$Ce_{0.82}Zr_{0.18}O_2$	Ce82	85	3.8	0.081	4.3	2.33
$Ce_{0.60}Zr_{0.40}O_2$	Ce60	93	2.7	0.019	3.2	2.30
$Ce_{0.46}Zr_{0.54}O_2$	Ce46	79	2.5	0.011	5.3	2.27
ZrO_2	Zr100	99	3.8	0.078	7.1	2.21
$Ce_{0.60}Zr_{0.40}O_2$[c]	Ce60-700	36	4.1	0.033	4.4	2.30
$Ce_{0.60}Zr_{0.40}O_2$[d]	Ce60-900	30	4.3	0.029	13.2	2.30

[a] All catalysts were calcined at 500 °C for 4 hours unless noted otherwise
[b] Composition of mixed oxide determined by PIXE analysis
[c] Catalyst was calcined at 700 °C
[d] Catalyst was calcined at 900 °C
[e] Calculated from XRD

2.3.2 Powder x-ray diffraction (XRD)

The x-ray diffractograms of all catalysts calcined at 500 °C are shown in Figure 2.1. The diffraction pattern of the cubic fluorite lattice of pure ceria is well known [66-68]. In agreement with literature, the length of the unit cell of ceria was determined to be 5.40 Å based on the average of the unit cell lengths calculated at the four prominent diffraction peaks associated with the (111), (200), (220) and (311) planes [69]. All peaks in the diffractogram were attributed to ceria, indicating that there are no crystalline impurities present.

The diffraction patterns of the tetragonal and cubic crystal structure of zirconia are more difficult to distinguish due to similar lattice parameters. However, by comparing the zirconia sample to reference diffractograms, I determined that the sample is tetragonal [70]. Specifically, the 2θ region of 70-76° was used to distinguish between one plane (400) present in a cubic zirconia, and two planes (400) and (004) for a tetragonal zirconia

phase. This region of the zirconia sample displayed a broad signal indicative of two ill-defined peaks from a tetragonal phase of zirconia. Further supporting this assignment, tetragonal zirconia is stable at calcination temperatures of 500 °C when the crystallite size is less than 30 nm [71]. Since the zirconia sample has a crystallite size of 7 nm, it is safe to expect the tetragonal phase was formed in the present study.

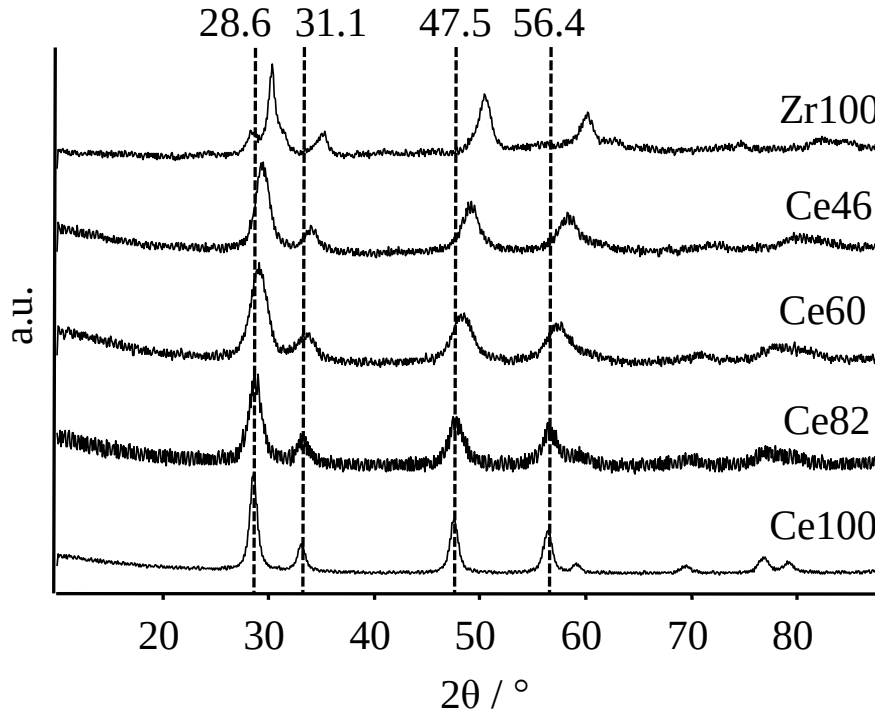

Figure 2.1 XRD of ceria-zirconia mixed oxides calcined at 500 °C.

The x-ray diffractograms of the mixed oxides were dominated by the same four prominent peaks as the diffractogram of pure ceria. All peaks in the diffractogram were attributed to the ceria-based fluorite lattice indicating the absence of bulk crystalline

impurities. Therefore, it is concluded that the crystal structure of ceria-zirconia mixed oxides is that of ceria [56]. Three small diffraction peaks in the 65-85° range belong to the (400), (331) and (422) planes in pure ceria [72, 73]. As more zirconia is incorporated into ceria-zirconia, these planes become less resolved. This indicated that the planes in this 2θ range do not show long range order with zirconia present in the crystal lattice. The four prominent diffraction peaks associated with the cubic structure of ceria gradually shifted to the higher diffraction angles as the zirconium content increased (Figure 2.1). This is indicative of a decrease in the distance between the lattice planes or the lattice parameter, d, which are reported in Table 2.1. The most intense peaks from pure ceria and pure zirconia were found at similar diffraction angles. A mixture of ceria and zirconia in separate phases would give rise to one broad peak that could be deconvoluted into two peaks corresponding to contributions from ceria and zirconia, respectively. The narrowness of the peaks indicated that the catalysts are a solid solution, not separate ceria and zirconia rich phases. The crystallite sizes calculated by the Scherrer equation were between 3.2 and 5.3 nm and reached a minimum for Ce60 (Table 2.1). All ceria-zirconia mixed oxides had smaller crystallite sizes than pure ceria or zirconia. When the calcination temperature was increased for the Ce60 samples, the intensity of peaks increased, but no shift of the peak position was observed (Figure A.4). This allows us to conclude that the size of the unit cell and distance between planes was the same regardless of the calcination temperatures tested (Table 2.1). The absence of a shift of the peak positions indicates that the cubic crystal phase of the Ce60 catalyst is stable for all calcination temperatures tested.

2.3.3 Temperature-programmed reduction (TPR)

The redox properties of ceria-based catalysts were assessed by temperature programmed reduction (TPR) (Figure 2.2). In particular, the formation of oxygen

vacancies by surface reduction under typical reactions conditions for the conversion of hydrocarbon feedstocks (i.e. below 450 °C) is expected to have a strong influence on the performance of these catalysts [44, 55, 74].

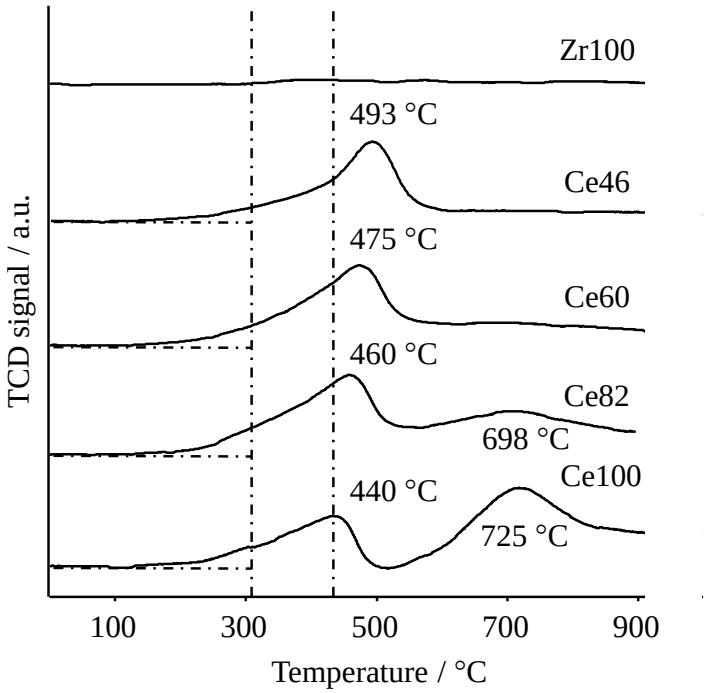

Figure 2.2 TPR of ceria-zirconia catalysts calcined at 500 °C.

No hydrogen consumption was observed for pure zirconia (Figure 2.2). Pure ceria had two main peaks from hydrogen consumption at 440 °C and 725 °C. The low temperature peak at 440 °C can be attributed to surface reduction, while the high temperature peak is assigned to bulk reduction [44]. It is important to take into account that dissociative adsorption of hydrogen is likely to contribute to the shoulder of the peak at 440 °C. Addition of zirconia caused the high temperature ceria peak to shift to lower temperatures. Consequently, bulk reduction was difficult to distinguish from surface

reduction in ceria-zirconia samples. A shoulder formed at the low temperature side of the first peak, and its intensity depended on the amount of zirconia that was incorporated into the crystal lattice. Specifically, the integral below 300 °C was highest for Ce60 and Ce82, whereas lower and approximately equal values were observed for Ce100 and Ce46. For the temperature range up to 450 °C, the largest amount of hydrogen consumed was by Ce82 followed by Ce60. Ce100 and Ce46 had similar values for hydrogen consumption. This indicates that surface reduction is occurring at lower temperatures with the incorporation of zirconia. The maximum of the low temperature peak shifted to higher temperatures as the amount of added zirconia increased due to an increasing contribution of bulk reduction to this peak.

In the reduction profiles of Ce60 calcined at different temperatures, only one reduction peak was resolved (Figure A.5). As the calcination temperature was increased, the reduction peak shifted from 475 °C for Ce60-500 to 730 °C for Ce60-900 and hydrogen consumption below 300 °C decreased markedly. The reduction peak at high temperature is attributed to an increasing contribution of bulk reduction as the surface area of for Ce60-900 is only 32% of the surface area of Ce60-500 °C.

2.3.4 Low temperature oxygen storage capacity

The concentration of oxygen vacancies formed during reduction at 200, 300 or 450 °C was quantified by titration with O_2 (Table 2.2). As expected, no oxygen vacancies were formed on zirconia over the entire temperature range. At 200 °C, no oxygen consumption was measured for any samples. However, in the TPR experiments, a certain amount of hydrogen was consumed by all ceria based samples below 200 °C. This observation is significant because it shows that hydrogen is adsorbed on the surface before the reduction of the surface begins. It also indicates that adsorbed hydrogen does not contribute to the consumption of O_2 during titration. At 300 °C, a notable amount of

oxygen vacancies was formed for ceria and all ceria-zirconia samples calcined at 500 °C. The concentration of oxygen vacancies (per mass of catalyst) was the highest for Ce82 and Ce60. At 450 °C, a significantly larger number of oxygen vacancies were formed for all samples (Table 2.2). The density of oxygen vacancies on the surfaces of ceria-zirconia samples calcined at 500 °C was at least 1.6 times that of ceria. The highest density was found for Ce60 and Ce46.

Table 2.2 Low temperature oxygen storage capacity of ceria-zirconia calcined at 500 °C.

Composition of Mixed Oxide	Concentration of oxygen vacancies ($\mu mol*g^{-1}$)			Density of oxygen vacancies (O^{2-} atoms$*nm^{-2}$)		
	200 °C	300 °C	450 °C	200 °C	300 °C	450 °C
Ce100	0	80	276	0	0.8	2.6
Ce82	0	146	596	0	1.0	4.2
Ce60	0	144	780	0	0.9	5.1
Ce46	0	92	656	0	0.7	5.0
Zr100	0	0	0	0	0	0

The oxygen storage capacity Ce60 calcined at 700 and 900 °C was low. Specifically, no sites were found at 200 °C, while Ce60-700 had a concentration of 21 $\mu mol*g^{-1}$ at 300 °C. Ce60-900 formed no vacancies at 300 °C. The decrease in the concentration of oxygen vacancies with increasing calcination temperature is most likely due to the decrease in surface area that also occurs with increase in calcination temperature.

2.3.5 Hydrogen-deuterium exchange

2.3.5.1 Quantification of exchangeable surface hydrogen

The quantity of exchangeable hydrogen on ceria-zirconia catalysts was analyzed using the test reaction of isotopic scrambling of hydrogen and deuterium to hydrogen-deuterium as shown in equation 2.1. Specifically, a hydrogen saturated surface was exposed to deuterium, while the quantitative composition of the product stream was monitored.

$$H_2 + D_2 \underset{k_{backward}}{\overset{k_{forward}}{\rightleftharpoons}} 2HD \qquad (2.1)$$

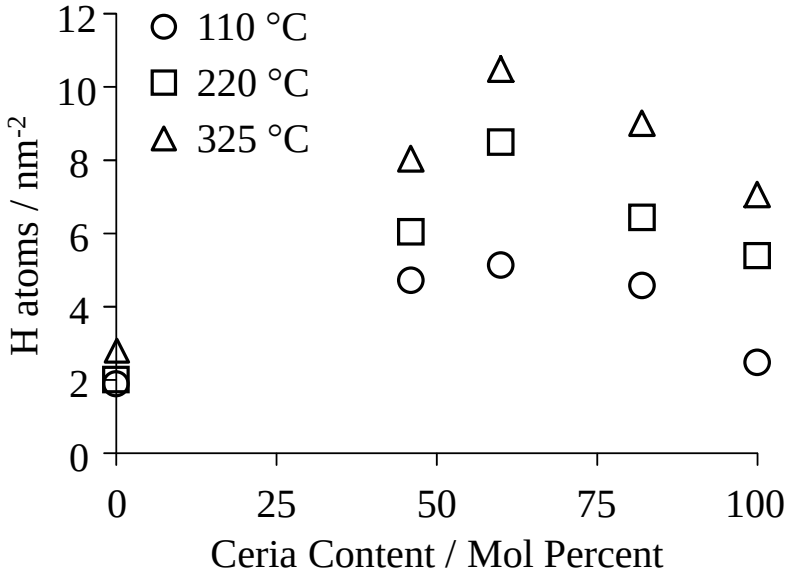

Figure 2.3 Quantity of exchangeable hydrogen on ceria containing catalysts.

The amount of exchangeable hydrogen for all catalysts calcined at 500 °C was determined at 110 °C, 220 °C and 325 °C (Figure 2.3). All catalysts dissociated hydrogen at all temperatures studied. Ceria-zirconia catalysts had a higher density of exchangeable hydrogen than pure ceria and pure zirconia at all temperatures. At 110 °C, the density of exchangeable hydrogen atoms per nm^2 was comparable for the mixed oxides. However, there were distinct differences in the density of activated hydrogen species on ceria-zirconia at 220 °C and 325 °C. Specifically, the highest density of exchangeable hydrogen was found for Ce60 followed by Ce82 and Ce46. While the density of exchangeable hydrogen increased significantly with increasing temperature for all ceria containing samples, only a minor increase was observed for zirconia.

2.3.5.2 Kinetics of isotopic hydrogen exchange

Before intrinsic kinetics of isotopic scrambling of hydrogen could be studied, mass and heat transport limitations were evaluated according to criteria given by Mears [75] and Boudart [76] . To probe for external mass or heat transfer limitations, the flow rate was varied at constant space velocity at 110, 220, and 325 °C. Since no variations in conversion were found, it was concluded that external heat and mass transfer limitations did not exist under the given experimental conditions (Figure A.6). To assess the impact of internal mass transfer limitations, the particle sizes were varied from less than 75 μm to 250-350 μm, and no appreciable change in reaction rate was found over the entire temperature range of interest (Figure A.7). Therefore, pore diffusion transport limitations were determined to be negligible. Heat transfer limitations were not expected to be an issue because the isotopic hydrogen exchange reaction is almost thermoneutral [62], but

the present experiments also explicitly verify that none of the reactions are limited by heat transfer.

The order of the reaction in H_2 and D_2 was determined under differential conditions, and a half order in each reactant (i.e. hydrogen and deuterium) was found (Figure A.8 and A.9). The hydrogen-deuterium exchange at 110, 220 and 325 °C was measured at steady state and compared to temperature programmed experiments (Table A.1). No significant deviations were found.

To gain further insight into the kinetics, H_2-D_2 exchange was studied as temperature programmed experiments (Figure 2.4). Pure ceria had the highest H_2-D_2 conversion over the entire temperature range tested. At temperatures lower than 300 °C, the H_2-D_2 conversion decreased in order of decreasing ceria content. However, when the temperature exceeded 300 °C, the H_2-D_2 conversion over zirconia exceeded that over Ce46. It is important to note that all catalysts were reduced at 450 °C prior to the experiment to avoid H_2 or D_2 consumption due to reduction.

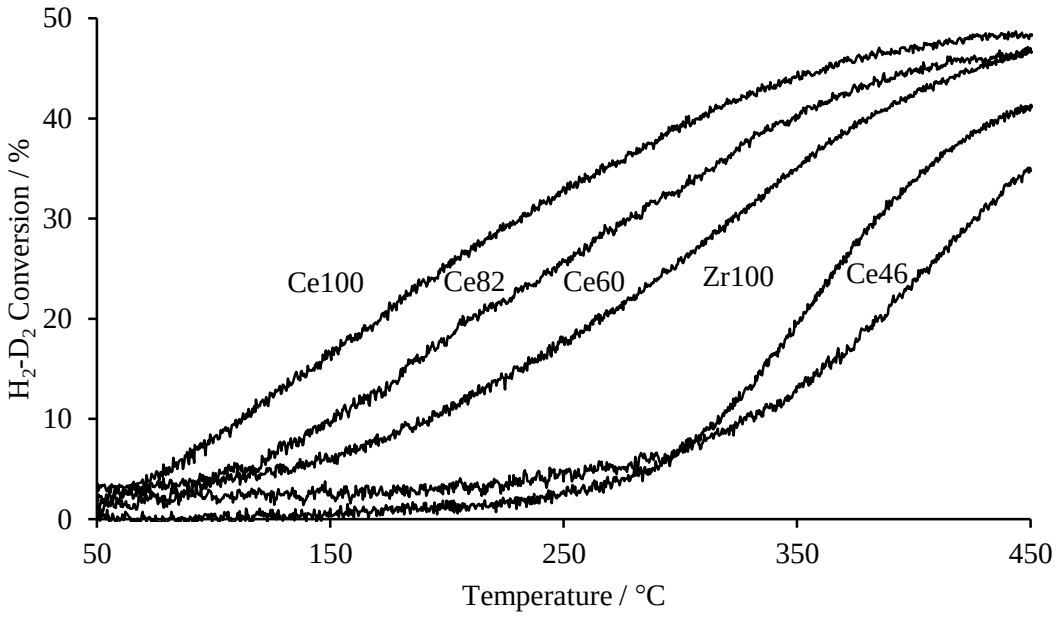

Figure 2.4 H_2-D_2 conversion over metal oxides as a function of temperature.

The data shown in Figure 2.4 was used to derive a model for the kinetics of the reaction. The simplifying assumptions of this model are the omission of isotope effects and the equality of all adsorption sites. Based on these assumptions, the rate of hydrogen consumption in an equimolar feed of H_2 and D_2 can be stated as:

$$-r_{H_2} = k_{forward}\left(C_{H_2} - K^{-1} * 2C_{HD}\right) \quad (2.2)$$

Where $k_{forward}$ is the rate constant of isotopic scrambling in forward direction (Equation 2.1), C_{H2} is the concentration of hydrogen, K^{-1} is the reciprocal of the equilibrium constant, which was calculated using thermodynamic data from literature

[62] (Figure A.10). C_{HD} is the concentration of hydrogen-deuterium. The rate of hydrogen consumption can be expressed in terms of conversion (X) as:

$$-r_{H_2} = k_{forward}\ ((C_{H_{2,in}} * (1 - X)) - K^{-1} * 4C_{H_{2,in}} X) \tag{2.3}$$

The rate of hydrogen consumption can be plugged into the integral form of the design equation for a fixed bed reactor.

$$\tau' = C_{H_{2,in}} \int_0^X \frac{dX}{-r_{H_2}} = C_{H_{2,in}} \int_0^X \frac{dX}{k_{forward}\ ((C_{H_{2,in}} * (1-X)) - K^{-1} * 4C_{H_{2,in}} X)} \tag{2.4}$$

Where τ' is:

$$\tau' = \frac{m_{catalyst}\ * C_{H_{2,in}}}{F_{H_{2,in}}} \tag{2.5}$$

Where $m_{catalyst}$ is the mass of catalyst in the reactor, $C_{H2,in}$ is the inlet concentration of hydrogen and $F_{H2,in}$ is the inlet flow rate of hydrogen.

Integration of equation 2.4 results in the following expression.

$$\tau' = \left(\frac{1}{k_{forward}}\right)\left(\frac{-\ln(-4*K^{-1}*X-X+1)}{-4*K^{-1}+1}\right) \quad (2.6)$$

Equation 2.6 was solved at each temperature for $k_{forward}$, and an Arrhenius plot was prepared to determine activation energy (Figure 2.5).

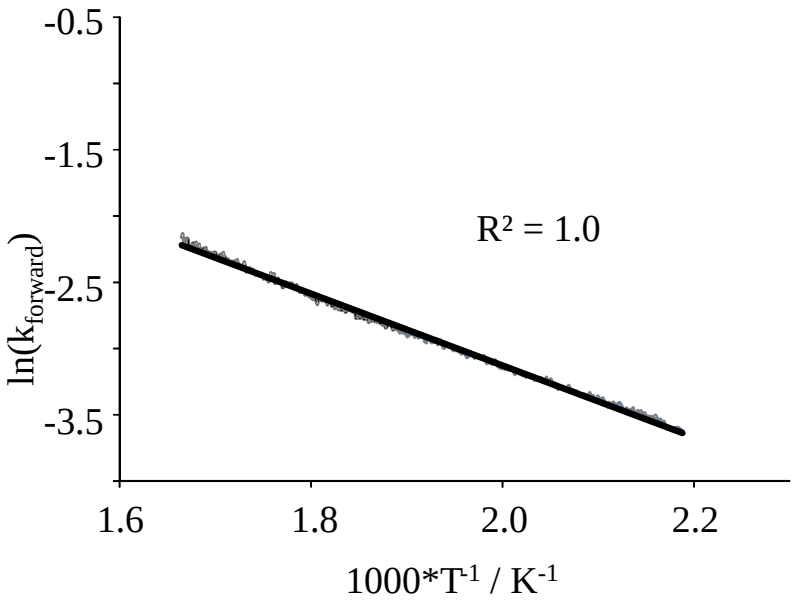

Figure 2.5 Arrhenius plot for H_2-D_2 exchange over ceria calcined at 500 °C.

For pure ceria and zirconia, the Arrhenius plot was linear up to the activation temperature of 450 °C. Higher temperatures were not investigated because the reduction of ceria containing samples would contribute to the consumption of H_2 and D_2. Activation energies of 22 and 66 $kJ \cdot mol^{-1}$ were determined for ceria and zirconia, respectively. These values are in agreement with literature values obtained in the same temperature range [77].

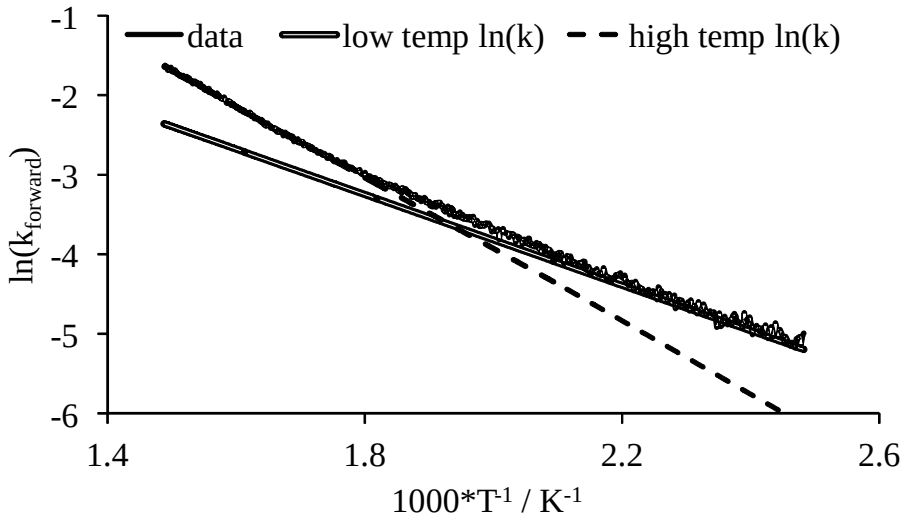

Figure 2.6 Arrhenius plot of Ce60 calcined at 500 °C.

The Arrhenius plot of ceria-zirconia samples followed a distinctly different behavior. The mixed oxides have a linear range below ca. 200 °C and a second linear range with a different slope at higher temperature (Figure 2.6). Since the slope is steeper at higher temperatures, the transition cannot be attributed to transport limitations becoming relevant. In addition the absence of such limitations was explicitly verified (vide supra). Instead, it is suggested that two types of active sites can contribute to the

observed reactivity [78]. Specifically, two types of active sites contribute to the observed reactivity at high temperature, whereas at low temperature only one of the sites shows measurable activity. Based on this theory, a new model involving two types of active sites was derived for isotopic hydrogen exchange over ceria-zirconia. This model is based on the same assumptions as the one involving a single type of active sites with the additional assumption that isotopic hydrogen exchange is only kinetically relevant on one type of sites at temperatures below the kink (i.e. around 200 °C) in the Arrhenius plot, whereas the reaction occurs to a significant extent on both types of sites at higher temperature. The rate of hydrogen consumption can be written in terms of conversion as:

$$-r_{H_2} = k_{f,1}\left(\left(C_{H_{2,in}} * (1-X)\right) - K^{-1} * 4C_{H_{2,in}}X\right) + k_{f,2}\left(\left(C_{H_{2,in}} * (1-X)\right) - K^{-1} * 4C_{H_{2,in}}X\right) \quad (2.7)$$

Where $k_{f,1}$ is the rate constant for the forward reaction over the first type of sites and $k_{f,2}$ is the rate constant for the forward reaction over the second type of sites. Note that terms for the concentration of each time of site are lumped into the respective rate constants. Using rate equation (2.7), the integrated form of the design equation for a fixed bed reactor becomes:

$$\tau' = \left(\frac{1}{k_{f,1}+k_{f,2}}\right)\left(\frac{-\ln(-4*K^{-1}*X-X+1)}{-4*K^{-1}+1}\right) \quad (2.8)$$

The activation energy and pre-exponential factor over the first type of sites was calculated using equation 2.6 in the low temperature range of the Arrhenius plot. Then, the contribution of these sites to the observed reactivity was projected over the entire temperature range of the experiment (i.e. up to 450 °C). The additional activity was attributed the second type of sites and the activation energy over these sites was calculated using equation 2.8. It was found that the model with two types of active sites accurately represent the conversion over all ceria-zirconia samples over the entire temperature range of interest (Figure 2.7). Specifically, the coefficient of determination (R^2) was greater than 0.99for all samples. The activation energy results for the high and low temperature sites are summarized in Table 2.3.

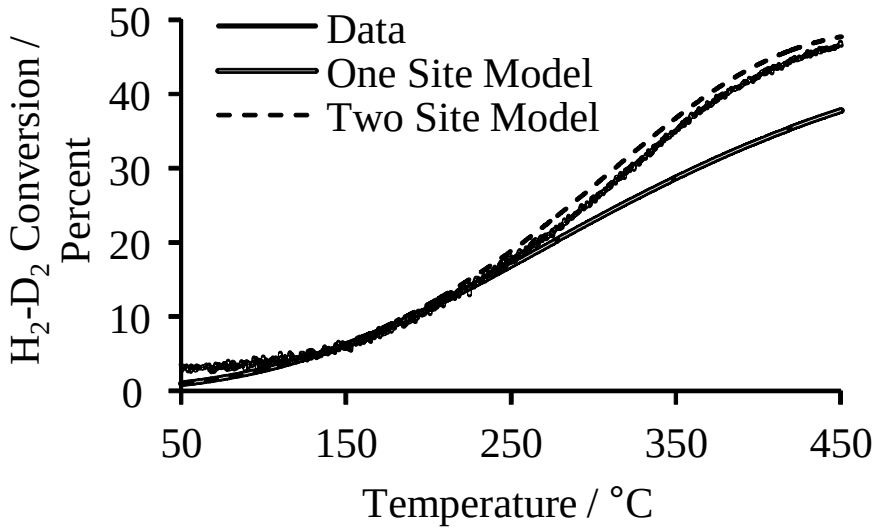

Figure 2.7 H_2-D_2 conversion over Ce60 compared with one and two site models.

Table 2.3 Site one and site two activation energies for each catalyst.

Mixed Oxide Content	Site One E_a (kJ/mol)	Site Two E_a (kJ/mol)
Ce100	22	N/A
Ce82	23	78
Ce60	25	62
Ce46	24	88
Zr100	N/A	66

2.3.6.3 IR spectroscopic analysis of hydrogen-deuterium exchange

In-situ FTIR spectroscopy was used to characterize the activity of different surface hydroxyl group in isotopic hydrogen exchange over ceria (Figure 2.8), zirconia (Figure A.11) and Ce-60 (Figure 2.9).

(a)

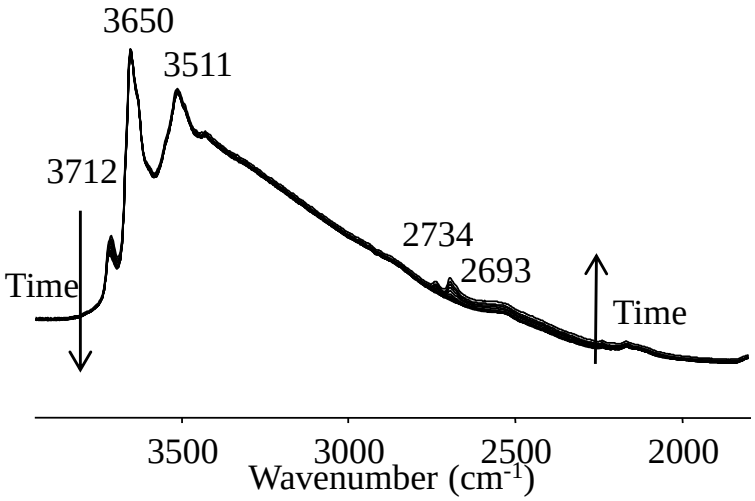

(b)

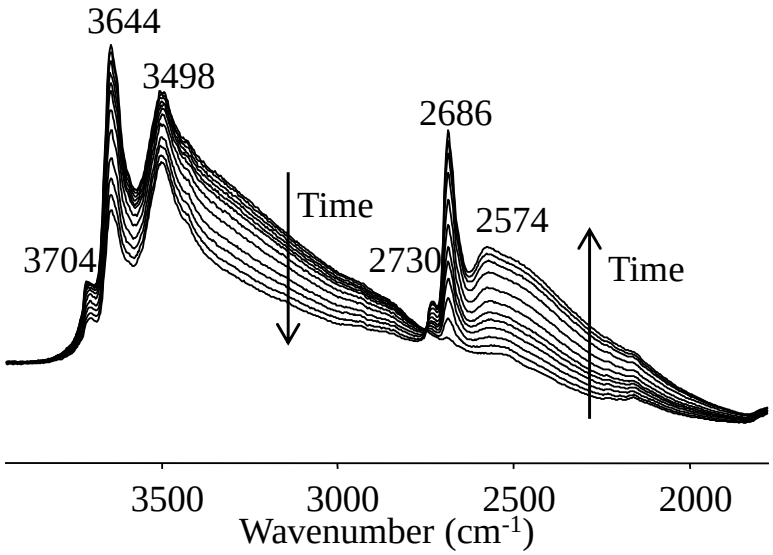

Figure 2.8 FTIR spectra of H_2-D_2 exchange on ceria at (a) 150 °C and (b) 350 °C.

When pure ceria was examined after reduction at 450 °C and cooling to 150 °C, three sharp peaks were observed at 3712 cm^{-1}, 3650 cm^{-1} and 3511 cm^{-1} along with a shoulder at 3631 cm^{-1} (Figure 2.8a). When the sample was cooled to 350 °C after the same activation procedure these peaks appeared at 3714 cm^{-1}, 3644 cm^{-1} and 3498 cm^{-1}, respectively, while the shoulder was observed at 3627 cm^{-1} (Figure 2.8b). The peak at 3712 cm^{-1} is attributed to stretching vibrations of singly bound hydroxyl groups (I), and the peak at 3650 cm^{-1} is assigned to bridging hydroxyl groups (II-A) [79-82]. The shoulder at 3631 cm^{-1} is attributed to bridging hydroxyl groups next to oxygen vacancies (II-B) [79, 80, 83]. The peak at 3511 cm^{-1} is attributed to oxyhydroxide species within small pores [79]. In additions to the sharp peaks, a broad feature ranging to approximately 2000 cm^{-1} was observed. It is assigned to hydroxyl groups engaged in hydrogen bonds [79, 84]. The slight red shift of the peaks at 350 °C relative to the experiment at 150 °C is attributed to a lower degree of reduction of the surface [79, 83]. It is suggested that the oxygen mobility at 350 °C is sufficiently high for some sub-surface O^{2-} anions to saturate oxygen vacancies on the surface. In addition to bands from surface hydroxyl groups, a peak at 2160 cm^{-1} was observed, which is assigned to the $2F_{5/2} \rightarrow 2F_{7/2}$ electronic transition of Ce^{3+} [80, 85]. Thus, this peak gives a semi-quantitative indication of the extent of reduction of cerium atoms in the sample.

When D_2 was pulsed over ceria at 150 °C, the intensity of the ν_{OH}-I peak at 3712 cm^{-1} decreased, while no changes were observed for the other bands. At the same time, two new peaks were observed at 2734 and 2693 cm^{-1} along with a shoulder at 2680 cm^{-1}. The peak at 2734 cm^{-1} and 2693 cm^{-1} are assigned to deuterated type I and type II-A groups, respectively, whereas the shoulder corresponds to deuterated type II-B hydroxyl groups next to an oxygen vacancy. The formation of OD groups at the expense of OH groups can be attributed to isotopic exchange. However, the bands of type II-A and II-B hydroxyl groups were larger than the peak at 2734 cm^{-1}. This can be explained by the

conversion of singly bound hydroxyl groups to bridging ones or by dissociative adsorption of D_2 forming additional hydroxyl groups.

When D_2 was pulsed over ceria at 350 °C, all ν_{OH} peaks from type I, II-A, II-B and hydrogen bonding hydroxyl groups decreased significantly, but they did not disappear completely (Figure 2.8b). The decrease of the band of the single bound hydroxyl groups was more pronounced than that of the bridging species (II-A and II-B), which decreased to about the same extent. The intensity of the ν_{OH} band of the oxyhydroxide species remained unchanged indicating that these species are not participating in any exchange reactions. In parallel to the decrease in intensity of most ν_{OH} bands, a small peak corresponding to type I OD groups (2730 cm^{-1}) appeared along with the more pronounced peaks from type II-A OD groups (2686 cm^{-1}) and the shoulder corresponding to type II-B OD groups (2670 cm^{-1}). Moreover, a broad ν_{OD} band from hydrogen bonding OD groups was observed at 2574 cm^{-1} [79]. The present experiments indicate that, singly coordinated hydroxyl groups and, to a slightly lesser extent, bridging hydroxyl groups exchanged at 350 °C. No strong preference the formation of bridging OD groups close to vacancies (II-B) or away from these sides (II-A) was observed.

Zirconia was treated under the same activation conditions, even though it is not a reducible metal oxide in this temperature range. When cooled from 450 °C to 150 °C, two peaks were observed at 3737 and 3677 cm^{-1}, which are attributed to singly bound and bridging hydroxyl groups, respectively (Figure A.11). In addition, the very broad band extending to about 2000 cm^{-1} is assigned to the ν_{OH} vibrations of hydrogen bonding OH groups [86]. A peak was observed at 2340 cm^{-1} and could be attributed to physisorbed linear CO_2 . When zirconia was reduced at 450 °C and cooled to 350 °C, the peaks of free OH groups appeared at 3739, and 3666 cm^{-1}. When D_2 was pulsed over zirconia at 150 °C, the peaks at 3737 and 3677 cm^{-1} decreased very slightly. This indicates that only a few of the hydroxyl groups were exchanged with deuterium at this temperature. Two new

peaks evolved at 2775 cm^{-1} and 2712 cm^{-1} and are assigned to singly bound and bridged OD groups, respectively. The pronounced shoulder at lower wavenumbers is indicative for the formation of hydrogen bonding OD groups. The formation of these deuterated hydroxyl groups is attributed to a combination of limited H-D exchange and dissociative adsorption of D_2 on the surface. When deuterium is pulsed over activated zirconia at 350 °C, the intensity of the bands corresponding to singly bond (3739 cm^{-1}) and bridging (3666 cm^{-1}) OH groups decreased substantially. In parallel, bands from ν_{OD} vibrations of singly bound and bridging OD groups developed at 2759 and 2701 cm^{-1}, respectively. In addition, a broad band formed around 2500 cm^{-1} which is indicative of hydrogen bonding between deuterated hydroxyl groups. The intensity of all OD bands was much higher compared to the experiment at 150 °C.

(a)

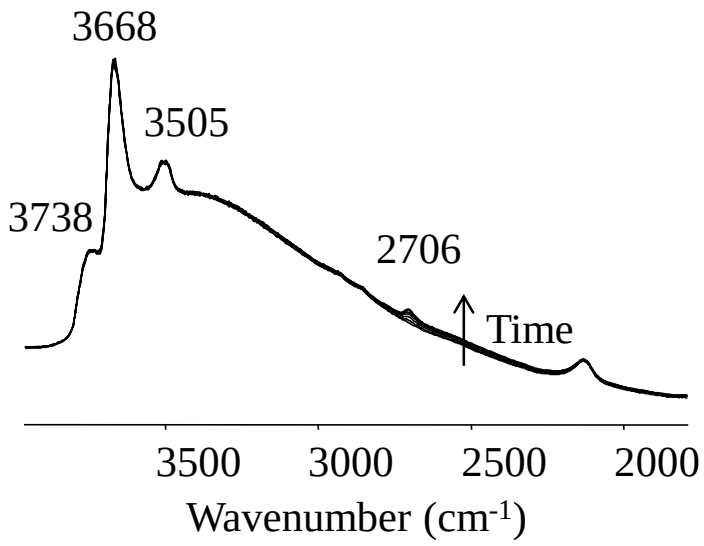

(b)

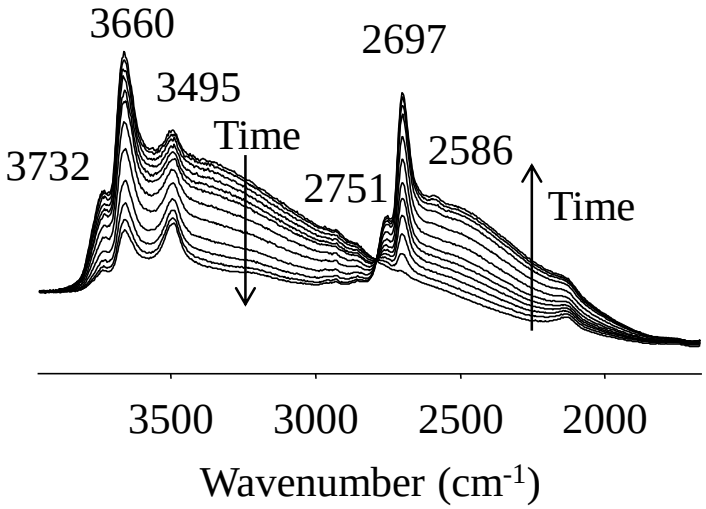

Figure 2.9 FTIR spectra of H_2-D_2 exchange on Ce60 at (a) 150 ℃ and (b) 350 ℃.

The spectra of Ce60 after activation at 450 °C (Figure 2.9) resembled those of pure ceria (Figure 2.8). When the temperature was decreased to 150 °C, bands were observed at 3738, 3668, 3640 (shoulder), and 3505 cm^{-1} (Figure 2.9a). The same bands appeared at 3732, 3660, 3634, and 3495 cm^{-1} when Ce60 was only cooled to 350 °C after activation (Figure 2.9b). The peak at 3738-3732 cm^{-1} is attributed to singly bound hydroxyl groups (I) [80, 83]. It is noted that the position of this peak was closer to that of singly bond ZrOH groups than that of CeOH groups. It is possible that hydroxyl groups bound to a single Ce atom exist, but the corresponding peak was not well-resolved. The assignment of the other peaks is analogous to the spectrum of pure ceria, namely, bridging hydroxyl groups (II-A) (3668-3660 cm^{-1}) [82, 83], bridging hydroxyl groups next to oxygen vacancies (II-B) (3640-3634 cm^{-1}) [82, 83], and oxyhydroxide groups (3505-3495 cm^{-1}) [79, 82]. Consistent with the observations for pure ceria (Figure 2.8), the peak positions shifted by up to 10 cm^{-1} due to changes in the degree of surface reduction [79, 83]. A broad feature corresponding to hydrogen bonding hydroxyl groups was observed between 3800 and 1900 cm^{-1}. The peak corresponding to the electronic $2F_{5/2} \rightarrow 2F_{7/2}$ transition (2128 cm^{-1}) was observed somewhat broader than in the case of pure ceria (Figure 2.8). This broadening is attributed to a slight anisotropy of the electronic states of cerium atoms in different local environments.

When deuterium was pulsed over ceria-zirconia at 150 °C, the II-A and II-B bands decreased minimally, and a small peak appeared at 2706 cm^{-1} with a shoulder at 2690 cm^{-1} (Figure 2.9a). These features are corresponding to deuterated II-A and II-B species, respectively. It is proposed that these species are formed by a combination of isotopic exchange and dissociative adsorption of D_2. No peaks from other deuterated hydroxyl groups were observed.

When D_2 was pulsed over ceria-zirconia at 350 °C, the I, II-A, and II-B peaks in the ν_{OH} region strongly deceased in intensity, but did not disappear entirely (Figure 2.9b). The band of the oxyhydroxide species (3495 cm^{-1}) became more resolved and appeared

somewhat more intense, but this is attributed to the decreasing intensity of the ν_{OH} band of hydrogen bonding hydroxyl groups. The peaks associated with deuterium containing I (2751 cm^{-1}) II-A (2697 cm^{-1}), and II-B (2674 cm^{-1}) hydroxyl groups were significantly more intense compared to the experiment at 150 °C. In the beginning of the exchange experiment, the peak corresponding to hydroxyl groups near vacancies (II-B) had almost the same intensity as the peak of the deuterated II-A species. However, the relative intensity of the latter increased as exchange proceeded. The appearance of a broad peak at 2586 cm^{-1} indicated that hydrogen bonding hydroxyl groups are susceptible to isotopic exchange at 350 °C.

2.4 Discussion

2.4.1 Structure-property relationships for ceria-zirconia

The physicochemical properties of ceria-zirconia catalysts vary widely depending on the elemental composition and the morphology of the material [49, 56, 87, 88]. When relationships between the synthesis conditions, the structure of the catalysts, and their performance in catalytic reactions are established, improvement of catalytic properties becomes possible. This study focuses on characterizing the properties of ceria zirconia catalysts with regard to their use as catalysts for hydrodeoxygenation (HDO) of oxygenates in biomass derived pyrolysis oils. Most importantly, the ability of these materials to dissociatively adsorb hydrogen is critical. In addition, the reducibility of surface sites under reaction conditions (300 – 450 °C) is a prerequisite.

A number of publications reported on the reduction of ceria-zirconia catalysts [32, 44, 52]. As temperature increases, physisorbed water is removed and singly-bound hydroxyl groups are eliminated by condensation leading to the formation of oxygen defect sites [81]. In this reaction, two unpaired electrons are left behind to reduce Ce^{4+}

species to Ce^{3+}. As the parts of the topmost layer of oxygen atoms are removed, more unsaturated surface cerium atoms are exposed, and the subsurface layers begin to be reduced [89]. Once the temperature is high enough, bulk oxygen atoms become mobile and migrate to the surface where they fill oxygen vacancies leaving behind oxygen defects in the bulk.

The present study illustrates that the structural and chemical properties of ceria-zirconia are related in a complex manner. The incorporation of zirconia into the cubic lattice of ceria causes a slight contraction of this structure. I speculate that this contraction in turn results in less efficient crystallization and, thus, a smaller average crystallite size. The crystallite size appears to be the most important descriptor of other physicochemical properties of the catalysts. Not surprisingly, the surface area increased with decreasing crystallite size. For the ceria and ceria-zirconia samples, this correlation was approximately inversely proportional. Zirconia deviated from this trend. However, this material possessed a distinct crystal lattice.

Smaller ceria crystallites are also known to reduce more readily at low temperatures than larger crystallites [44, 52]. Nano-crystalline ceria has a lower reduction enthalpy of 1.84 eV than bulk ceria (4.67 eV) and thus can be completely reduced at a lower temperature than bulk ceria [90]. In the present study, the density of oxygen vacancies (O^{2-} atoms*nm^{-2}) at 450 °C was found to be the largest for Ce60 followed by Ce46. However, the density of oxygen vacancies was somewhat lower for Ce82, which had smaller crystallites than Ce46. This indicates that the crystallite size alone is not a sufficient descriptor for the low temperature reducibility of these samples. Therefore, it is suggested that chemical and structural properties affect the oxygen storage capacity at 450 °C. Specifically, Ce46 has increased bulk or subsurface reduction compared to Ce82. Increased bulk reduction caused more oxygen vacancies to form in Ce46, but not all of the vacancies were located on the surface and available for reaction.

2.4.2 H_2-D_2 exchange kinetics

Ceria and ceria-zirconia catalysts have been used for a wide range of reactions involving activated hydrogen including hydrogenation and dehydrogenation [31, 47, 91, 92]. Activation of hydrogen by dissociative adsorption is commonly attributed to the metal particles that are present in these catalysts, but several studies showed that dissociated hydrogen can spillover onto ceria and ceria-zirconia supports once it is formed. In addition, evidence for direct dissociative adsorption of hydrogen on ceria was reported by Martin and Duprez [77]. In this context, it is not entirely surprising that pure ceria can selectively hydrogenate propyne to propene [93]. However, detailed insight into the kinetics of such reactions and the effect of zirconia is missing.

The kinetic study in the present work provides detailed insight into the activation of hydrogen on ceria, zirconia, and ceria-zirconia in the absence of supported metal particles in a reducing environment. The pre-reduction of the samples allows the study of ceria based oxides in typical reactions conditions and avoids the participation of H_2 or D_2 in reduction of the catalyst during H_2-D_2 exchange. The observation of a reaction order of 0.5 for H_2 and D_2 in isotopic scrambling experiments over all catalysts studied here is consistent with a mechanism, in which dissociative adsorption of the reactants is the rate limiting step, and activated H and D species are present on the surface. Thus, the exchange reaction is a valuable probe reaction for the ability of these materials to dissociatively adsorb hydrogen.

The intrinsic kinetics of H_2-D_2 exchange over pure ceria and pure zirconia are adequately described assuming that all active sites on these materials are equal (section 2.3.5.2). However, a significantly lower activation energy was found over ceria (Table 2.3) [77]. Very little literature exists for the activation energies of ceria over oxidized and reduced samples. Martin and Duprez found an activation energy for reduced ceria to be 26 kJ/mol while an oxidized ceria was 59 kJ/mol [77]. The difference between an oxidized ceria surface and a reduced ceria surface is the presence of defect sites on the

reduced surface. Therefore, the low activation energy can be attributed to the presence of such sites.

The Arrhenius plots for the ceria-zirconia samples showed a clear transition around 200 °C (Figure 2.6). A good fit for the data is obtained based on the assumption that these catalysts contain two types of sites. Below 200 °C, the observed conversion is achieved over one type of sites, whereas the second type starts to contribute significantly to the H_2-D_2 exchange activity above this temperature. An activation energy of about 24 kJ*mol^{-1} was found for the first type of site over all ceria-zirconia samples (Table 2.3). This value is equal to the activation energy over pure ceria. Thus, it is suggested that similar sites (i.e. oxygen vacancies) are present on all of these catalysts.

The activation energy over the second type of sites was in the same range as that over pure zirconia, but it varied with the zirconia content of the sample (Table 2.3). In agreement with the characterization by XRD (Figure 2.1), this indicates that the presence of a second type of sites is due to the incorporation of zirconium into the ceria crystal lattice rather than the added activity of separate ceria and zirconia domains. Specifically, the activation energy of the second type of site decreased with decreasing crystallite size as determined by XRD (Figure 2.10). In contrast, there was no monotonous correlation between the activation energy over these sites and the elemental composition of these sites. For all ceria-zirconia catalysts investigated here, the activation energy over the second type of sites remained in the range that is typical for oxidized ceria or zirconia surfaces without vacancies [94].

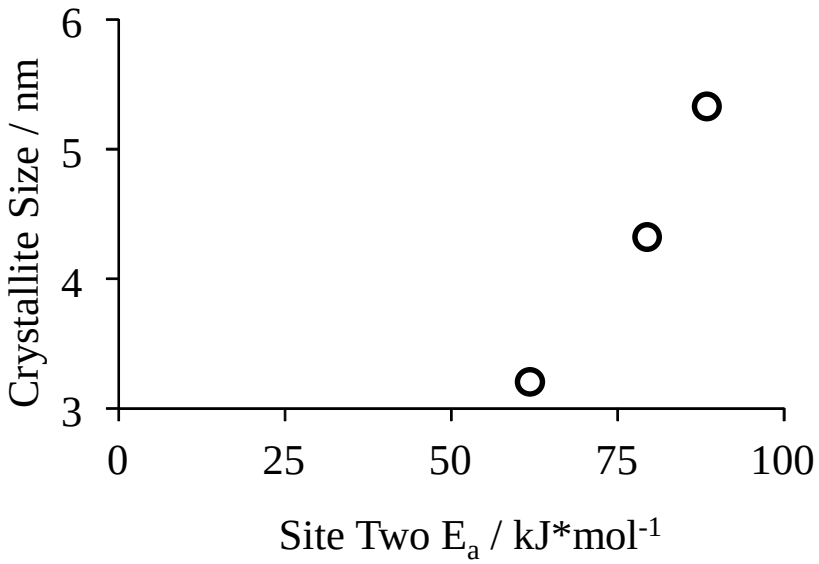

Figure 2.10 Site two E_a and crystallite size for ceria-zirconia calcined at 500 °C.

I propose that the activation energy over the second type of site depends on the chemical nature of oxidized surface sites in the samples. It was argued that small ceria crystallites can exchange hydrogen more effectively due to their larger number corner and edge sites [95]. While an increased contribution from such sites could account for an increase in conversion, it cannot be the sole reason for the gradual change of the activation energy over these sites. Therefore, I speculate that the decreasing particle size results in strains on the edges of the crystallites, which in turn lead to electronic effects that lower the activation energy for H_2-D_2 exchange.

2.4.3 Quantification of exchangeable surface hydrogen

The density of reactive hydrogen atoms on the surface a catalyst is an important descriptor for its activity in reactions involving hydrogen. Activated surface hydrogen must be available near the active site to on a relevant elementary reaction occurs [93].

Surface hydrogen on ceria, zirconia and ceria-zirconia was primarily studied in terms of hydrogen spillover from supported metals [45]. However, many studies overlook the importance of hydrogen dissociation on the support alone. To provide an assessment of the magnitude of this phenomenon, I quantified the amount of exchangeable surface hydrogen on ceria, zirconia and ceria-zirconia in a temperature range that is relevant for hydrogenation and HDO reactions (Figure 2.3) [93].

To my knowledge, the density of active surface hydrogen on ceria and zirconia in this temperature range was only quantified in one study [77]. Martin and Duprez reported that a monoclinic zirconia and a ceria sample reduced at 450 °C exchanged 1.4 and 2.8 hydrogen atoms per nm^2, respectively [77]. At similar temperatures, the tetragonal zirconia sample in this study exchanged about 2 hydrogen atoms per nm^2. Considering the difference in phase, the deviation is not surprising. In contrast, the pure ceria sample in this study exchanged around 7 hydrogen atoms per nm^2. The ceria used by in this study and Martin and Duprez have similar surface areas, but they may differ in other properties. Since Martin and Duprez used a commercial sample, it is impossible to compare the synthesis procedure used for the preparation of each sample. With the available information, the only clear difference is that the size of the catalyst particles in the present was 75-90 μm, which is smaller than the particles with sizes of 100 to 200 μm used by Martin and Duprez [46].

Ceria-zirconia had a higher density of exchangeable hydrogen than pure zirconia and pure ceria (i.e. 4.8-10.5 hydrogen atoms per nm^2). Specifically, Ce60 had the highest density at all temperatures. The density of exchangeable hydrogen atoms on ceria and ceria-zirconia appears to decrease with increasing crystallite size at all temperatures.

2.4.4 Identification of sites for H_2-D_2 exchange

Literature studies have identified singly-bound hydroxyls, bridging hydroxyls and hydroxyl groups next to oxygen vacancies as potential H_2-D_2 exchange sites for ceria and ceria-zirconia catalysts [79-81].However, surface exchange sites have not been quantified and studied along with reaction kinetics. In agreement with previous work, the kinetics over different catalysts in the present study indicated that the most active sites for H_2-D_2 exchange over ceria and ceria-zirconia are surface oxygen vacancies [77].

The in-situ FTIR spectra showed that bridging OD groups near vacancies were formed faster than other OD groups, when Ce60 was exposed to D_2. This observation confirms the role of oxygen vacancies in the dissociative adsorption of hydrogen/deuterium. However, even in the low temperature regime, in which the reaction appears to be limited to oxygen vacancies, other types of OD are formed.

It is well known that hydrogen can be very mobile on the surfaces of certain oxides , in some cases at temperatures as low as 25 ℃ [94, 96, 97]. Thus, it is suggested that hydrogen/deuterium atoms have substantial mobility on the surface of ceria and ceria-zirconia after dissociation at an oxygen vacancy. Martin and Duprez showed that diffusion of surface species plays a significant role in H_2/D_2 exchange over pure ceria and pure zirconia and that the acid-base properties of the oxide have a strong effect on the diffusion mechanism [77]. Basic oxides such as ceria have very mobile surface oxygen atoms, and hydroxyl groups can travel about the surface to adjacent oxygen vacancies. Zirconia is mildly acidic, and hydrogen can migrate across the surface in two ways depending on the degree of hydroxylation. At high hydroxylation hydrogen can transfer through an OH_2 intermediate between hydroxyl groups [77]. At low degrees of hydroxylation hydrogen can only transfer through hydrogen jumps from a hydroxyl group to a nearby oxygen atom without hydrogen. Due to the fast rate of diffusion of hydrogen/deuterium on the surface, it is only possible to gain insight into the nature of the first sites that activate H_2 and D_2. Once the temperature is high enough for the second

type of site to contribute, the migration of activated hydrogen/deuterium between different sites is so fast that it is impossible to identify which ones are the second type of active sites for the activation based on the FTIR spectra.

2.4.5. Implications for catalytic reactions

While understanding the kinetics and method of exchange for ceria and ceria-zirconia mixed oxides is important for the design of HDO heterogeneous catalysts (see chapter 3), it is also relevant for other catalytic reactions. Ceria-zirconia mixed oxides show a high activity for hydrogen-exchange that is approaching that of supported metals on oxides. For example, a house made 2 wt% Ni/Al_2O_3 catalyst exchanged 16 hydrogen atoms per nm^2 at 325 °C, while Ce60 exchanged 10.5 hydrogen atoms per nm^2 at the same temperature. Ceria-zirconia is certainly not a direct replacement for supported metal catalysts. For example, phenol derivatives mostly interact with ceria or ceria-zirconia through their functional groups, whereas the aromatic ring engages in significant interactions with metal sites [98]. However, the high activity of ceria-zirconia for isotopic H_2-D_2 exchange does show that these materials should be considered as more than inert supports for metal particles. In literature on supported metal on oxide catalysts, it is usually assumed that the dissociation of hydrogen only occurs on the metal particles, and the rate limiting step for exchange of hydrogen on the support is spillover (T < 75 °C) or diffusion onto the support (T > 75 °C) [45]. Since ceria-zirconia catalysts can dissociate hydrogen without metal sites, metal catalysts on ceria-zirconia supports should have increased availability of activated hydrogen because they do not need to rely exclusively on spillover.

Certain literature studies may appear in a new light following the results presented here. For example, reduced the surface hydrogen diffusion coefficient on Rh/CeO_2 was reported to be 7.7 times as fast as the one on Rh/Al_2O_3 under the same conditions [77].

The increase in the diffusion coefficient was attributed to the support. However, if dissociated hydrogen also originates from sites on the ceria support it is possible that the diffusion coefficient on Rh/CeO_2 was overestimated.

2.5 Conclusions

This study has found that the crystallite size of ceria-zirconia has a great impact on hydrogen exchange; however, crystallite size also affects other surface parameters which demonstrate the complexity of the surface of ceria-zirconia mixed oxides. The smaller crystallite size of ceria-zirconia causes an increase in surface area and low temperature oxygen vacancies when compared to pure ceria. More oxygen vacancies allow for more active sites for isotopic hydrogen exchange. Ceria-zirconia mixed oxides exchange hydrogen dissociatively through surface hydroxyl groups. At temperatures less than 200 °C, exchange occurs though singly bound hydroxyl groups next to oxygen vacancies. At temperatures above 200 °C, exchange also occurs through hydroxyl groups not adjacent to oxygen vacancies.

CHAPTER 3

HYDRODEOXYGENATION OF GUAIACOL

3.1 Background

Our society relies heavily on energy and chemicals to go about our daily lives. Transportation fuels in the United States come primarily from nonrenewable petroleum sources [2-4]. Petroleum is diminishing in supply, and it is important to find alternative feedstocks for producing transportation fuels and chemicals [4]. Fuels produced from alternative feedstocks must be compatible with our current infrastructure and technology [16]. This means that the fuels will need to be in liquid form, as well as mimic the properties of petroleum based fuels. The feedstock for both fuels and chemicals must be sustainable, limit the amount of CO_2 produced as a by-product and be as environmentally benign as possible. The feedstock should not create a competition between food and fuels or chemicals [21, 99]. Biomass can meet these requirements [4, 100].

Biomass can be processed many ways to create a useable intermediate feedstock. For example, pyrolysis of biomass can create a bio-oil similar to petroleum-based fuels from the thermochemical conversion of any carbonaceous material including agricultural waste, sewage sludge and chicken litter [12, 16]. Pyrolysis produces bio-oils by heating biomass in the absence of oxygen to temperatures of 375-525 °C and pressures of 1-5 atm. Flash pyrolysis, the most economically feasible pyrolysis at an industrial level, occurs at the above conditions at a residence time of only a few seconds [17, 18]. The initial products are gases which then condense to a liquid product. These bio-oils are obtained in high yields of up to 80 wt% dry feed with 10-40 wt% oxygen and 10-30 wt% water depending on the feed [12, 20, 21].

Flash pyrolysis produces bio-oils that have properties close to traditional petroleum based fuels with some major differences. These differences contribute to the

low heating value, high polarity, high acidity and high viscosity of the resulting oil compared to petroleum based fuels [9, 17-20]. Overall, most of the unfavorable characteristics of pyrolysis oils are associated with oxygen containing compounds. The oxygen in the bio-oil causes it to be much more acidic than crude oil. A low pH (2-4) is challenging for storage, transport and processing containers; traditional carbon steel and aluminum containers cannot be used due to high degrees of corrosion. The presence of very reactive organic compounds, which can polymerize in air, contributes to the instability of bio-oil [16, 22]. Over storage time, the average molecular weight, viscosity and water content increase and the oil yield decreases; phase separation can begin to occur. However, if the oxygen content of the oil is decreased, it is easier to mechanically separate the organic product from the water, the heating value increases and the oil becomes more stable. These issues indicate the necessary removal of at least some oxygen from pyrolysis oils before they are viable for replacement of petroleum based fuels [16, 22].

A currently evolving technology for oxygen removal is hydrodeoxygenation (HDO). In many cases, noble metal heterogeneous catalysts that were developed for hydrodesulfurization (HDS) are used in this process [22]. Moreover, sulfur, even in small concentrations, can poison noble metal catalysts in downstream reforming units [101-103]. Most commercial HDS catalysts are comprised of a supported MoS_2 with promoters such as Co^{2+} or Ni^{2+}. The Co^{2+}, or Ni^{2+}, works as a promoter that donates electrons to the Mo. The bond between the Mo and one adjacent S in the catalyst becomes weaker, and a defect site is formed. When the sulfur bonded to the feed molecule is positioned over the defect site, the carbon-sulfur bond can be broken [104-106]. Hydrogen is necessary to remove the sulfur from the surface of the catalyst, as H_2S, regenerating the defect site [106-109]. The defect sites in $CoMoS_2$ and $NiMoS_2$ can also bind oxygen and activate the oxygen-carbon bond [22, 23, 110].

In principle, HDO can be performed for a wide variety of feedstocks, and its flexibility gives it an advantage when working with pyrolysis oils. HDO requires a hydrogen source and combines the hydrogen with oxygen from functional groups in the feed to produce water. Some compounds have a low HDO reactivity and require a higher hydrogen pressure and temperature to remove all of the oxygen. Unfortunately, MoS_2 based catalysts will deactivate over time during HDO reactions because they transition to an oxide form instead of the active sulfide form. The sulfide form can be retained if H_2S is co-fed with the hydrogen. While, co-feeding works, it is not the best solution as sulfur contamination of sulfur free oil often results [111]. Due to the safety issues associated with H_2S, as well as the cost of noble metals catalysts in downstream processes; it is desirable to find affordable sulfur free catalysts for HDO.

This study aims to synthesize sulfur free, metal free, mixed metal oxides for HDO pyrolysis oil. The first requirement for HDO over a solid oxide catalyst is the oxygen in a molecule in the feed must attach to the surface. Adsorption on the surface, primarily occurs at defect sites. One way to create defects sites is to use transition metals with redox activity such as ceria, titania or vandia [31, 52, 112]. Ceria is known for easily transitioning from the 3+ to the 4+ oxidation state and is able to cycle back based on environmental conditions [113]. The final catalyst must activate the oxygen containing functional group of the compound. Finally, this catalyst must be able to dissociate hydrogen and add the hydrogen to break the carbon-oxygen bond and remove the oxygen from the catalyst surface as water [114]. To further complicate matters, the best catalysts for this reaction must be selective towards deoxygenated products while minimizing hydrogen consumption and coking and retain carbon [115].

In this study, the HDO activity of ceria-zirconia mixed oxides is demonstrated. The influence of temperature and reactant flow rates on conversion and product distribution are elucidated. The effect of the composition of the mixed oxide catalysts on the number of oxygen vacancy sites is discussed. The ceria-zirconia mixed oxides are

found to be selective towards HDO products at atmospheric pressure, while minimizing hydrogen consumption and maximizing carbon retention.

3.2 Materials and methods

3.2.1 Chemicals

Cerium(III) nitrate hexahydrate (99% trace metals basis), zirconyl (IV) oxynitrate hydrate (99% trace metals basis), ammonium hydroxide (A.C.S regent grade, NH_3 content 28-30%), octane, decane, guaiacol, methanol, and phenol were purchased from Sigma Aldrich. Gases (hydrogen, helium, 2000 ppm ammonia in helium, argon, and oxygen) were purchased from Airgas with ultra-high purity (UHP Grade 5). A VWR UHP air generator generated air for the gas chromatograph and calcination of the samples. Deionized water was purified to 18.2 $M\Omega*cm^{-1}$ with a Barnstead NANOpure ultrapure water system.

3.2.2 Catalyst preparation

All catalysts were prepared using precipitation or coprecipitation of cerium nitrate hexahydrate and/or zirconyl nitrate hydrate [56]. The precursors were dissolved in deionized water to form a 0.1 M solution. The synthesis method was modified by adding the precursor solution drop-wise to an aqueous ammonium hydroxide solution (28-30%) while stirring continuously. Precipitation occurred as soon as the precursor solution was added. The resulting precipitate was filtered, rinsed with deionized water, and subsequently dried in an oven at 100 °C overnight. The catalysts were calcined for 4 hours in 200 $mL*min^{-1}$ zero grade air at 500 °C with a ramp rate of 5 $°C*min^{-1}$.

3.2.3 Elemental analysis

Proton induced x-ray emission **(**PIXE) analysis was performed by Elemental Analysis Inc. to determine the quantity of cerium and zirconium in each catalyst.

3.2.4 X-ray diffraction

A Philips X'pert diffractometer equipped with an X'celerator module using Cu Kα radiation (λ = 1.54 Å) was used to measure powder x-ray diffraction (XRD) patterns. Diffractograms were measured in the range 2θ = 10-90° with 0.0083556° as the step size. The Bragg equation was used to calculate the inter-planar spacing. The Scherrer equation was used to calculate crystallite size based on the diffractions for the (111), (200), (220) and (311) planes and averaged to reduce the experimental error [57-59].

3.2.5 Nitrogen physisorption

A Micromeritics ASAP2020 physisorption analyzer was used to perform nitrogen physisorption at -196 °C. Before analysis, each sample (ca. 0.15 g) was degassed under vacuum at 200 °C for 4 hours. The Brunauer-Emmet-Teller (BET) surface area was calculated from the nitrogen adsorption isotherm between $0.05 \leq P/P_0 \leq 0.3$ [60]. The Barrett-Joyner-Halenda (BJH) method was used to calculate the pore volume [61].

3.2.6 Temperature programmed reduction (TPR)

A Micromeritics Autochem II 2920 was used to perform temperature programmed reduction (TPR) using ca. 0.2 g of each sample. The catalyst was heated at 10 °C*min^{-1} in 25 mL/min of 10 mol% oxygen in helium to 450 °C and held at 450 °C for 1 hour before cooling it to 0 °C at 15 °C*min^{-1}. Then, the catalyst was heated up to 1000 °C with a

ramp rate of 10 °C*min^{-1}, in a 10 mol% hydrogen in argon. The gas mixture exiting the reactor was monitored using a thermal conductivity detector (TCD). A blank experiment was performed to establish a baseline TCD signal over the entire temperature range.

3.2.7 Quantification of oxygen vacancies

Oxygen storage capacity measurements were performed to quantify concentration of oxygen defect sites using a Micromeritics Autochem II 2920 with ca. 0.2 g of each sample. First, the sample was heated to 300 or 450°C in a flow of 25 mL*min^{-1} of 10 mol% oxygen in helium. Next, the sample was held at 200, 300 or 450 °C for an hour before being reduced at the same temperature in a 10 mol% hydrogen in argon stream. The temperature of the sample was held constant for 30 minutes after which O_2/He was pulsed over the sample until no further uptake was detected (3 consecutive peaks of approximately equal area).

3.2.8 Reactivity studies

The performance of the catalysts for hydrodeoxygenation of guaiacol was studied using a vertical stainless steel trickle bed reactor with a diameter of 0.25 inches. The catalyst was a powder with a particle size in the range of 75-90 µm. The liquid feed was introduced into the reactor by a Teledyne ISCO 500D series syringe pump through a line preheated to 80 °C. Hydrogen was supplied with a Brooks SLA 5850 mass flow controller. Temperature and pressure were controlled with a Eurotherm 2416 temperature controller and an Equilibar EB1HP1-SS316 back pressure regulator, respectively. Products were analyzed with an online Aglient 7890A gas chromatograph (GC) with an HP-5 column and an flame-ionization detector. Whenever necessary, unknown products were identified by manual injection of known compounds into the gas chromatograph or

by gas chromatograph-mass spectrometer (GC-MS) analysis using a Varian GC attached to a Bruker mass spectrometer (MS). The GC column was aVF-35ms

Reactions were performed at various temperatures and flow rates. Each set of conditions was held constant for ten hours for a total time on-stream of 70 hours. In a typical experiment, approximately 0.5 g of catalyst was placed in the reactor, and a reactant stream containing guaiacol (33.7 $g*L^{-1}$), decane (702 $g*L^{-1}$) as solvent, and octane (5.9 $g*L^{-1}$) as an internal standard was fed to the reactor. A different reactant stream comprised of methanol (4.4 $g*L^{-1}$) and phenol (12.8 $g*L^{-1}$) was co-fed over Ce82 at 400 °C and 1 bar and a weight to feed ratio (W/F) of 1.4 h in one experiment to understand the reaction pathway to HDO products. The flow rate of hydrogen was kept constant at 40 $mL*min^{-1}$. The flow rate of the liquid reactant mixture was varied between 0.001 $mL*min^{-1}$ and 0.08 $mL*min^{-1}$ for a W/F of 0.1 to 11.2 h. The temperature was varied from 275 °C to 400 °C, and the pressure in the reactor was held constant at 1 bar. Conversion of guaiacol, X, was calculated as:

$$X\,[\%] = \frac{\dot{F}_{g,in} - \dot{F}_{g,out}}{\dot{F}_{g,in}} * 100 \qquad (3.1)$$

Where $F_{g,in}$ is the molar flow rate of guaiacol into the reactor and $F_{g,out}$ is the molar flow rate of guaiacol out of the reactor.

Yield of product, Y_p, is defined as:

$$Y_p\,[\%] = \frac{\dot{F}_{p,out}}{\dot{F}_{g,in} - \dot{F}_{g,out}} * 100 \qquad (3.2)$$

Where $F_{p,out}$ is the molar flow rate of the product of interest out of the reactor.

Selectivity of product is defined as:

$$S_p = \frac{Y_p}{X} \tag{3.3}$$

3.3 Results

3.3.1 Characterization

3.3.1.1 Composition and morphology

Characterization results of all samples are summarized in Table 3.1. The mixed metal oxide abbreviations were chosen based on their elemental composition determined by PIXE analysis. Besides cerium, zirconium, and oxygen only a small (less than 0.3 mol%) hafnium impurity was detected [63]. All mixed oxides were calcined at 500 °C and had surface areas that were higher than that of pure ceria, but lower than that of pure zirconia. Among the mixed oxides samples, the highest surface area was 93 $m^{2}{\cdot}g^{-1}$ for Ce60.

Table 3.1 Physciochemical properties ceria-zirconia catalysts

Composition of Mixed Oxide[a]	Abbreviation	BET surface area (m^2*g^{-1})	Pore width (nm)	Pore volume (cm^3*g^{-1})	Crystallite size (nm) [b]
CeO_2	Ce100	63	9.3	0.123	9.3
$Ce_{0.82}Zr_{0.18}O_2$	Ce82	85	3.8	0.081	4.3
$Ce_{0.60}Zr_{0.40}O_2$	Ce60	93	2.7	0.019	3.2
$Ce_{0.46}Zr_{0.54}O_2$	Ce46	79	2.5	0.011	5.3

[a] Composition of mixed oxide determined by PIXE analysis
[b] Calculated from XRD

All ceria-zirconia catalysts had a smaller average pore width than ceria. Ce60 and Ce46 both had smaller average pore widths than zirconia. Mixed oxide samples had pore volumes of 0.05 $cm^3 \cdot g^{-1}$ or below, which is smaller than the pore volume of pure ceria or zirconia.

The x-ray diffractograms of the mixed oxides were dominated by the same four prominent peaks as the diffractogram of pure ceria [66-68]. The length of the unit cell of ceria was determined to be 5.40 Å [69]. The crystallite sizes calculated by the Scherrer equation were between 3.2 and 5.3 nm and reached a minimum for Ce60 (Table 3.1). All ceria-zirconia mixed oxides had smaller crystallite sizes than pure ceria or zirconia. A more detailed description of the physiochemical properties of the ceria-zirconia catalysts is found in Chapter 2.

3.3.1.2 Temperature-programmed reduction (TPR)

A first assessment of the redox properties of ceria-based catalysts was obtained by temperature programmed reduction (TPR) (Figure 3.1). In particular, the formation of oxygen vacancies by surface reduction under typical reactions conditions for the

conversion of hydrocarbon feedstocks (i.e. below 450 °C) is expected to have a strong influence on the performance of these catalysts [44, 55, 74].

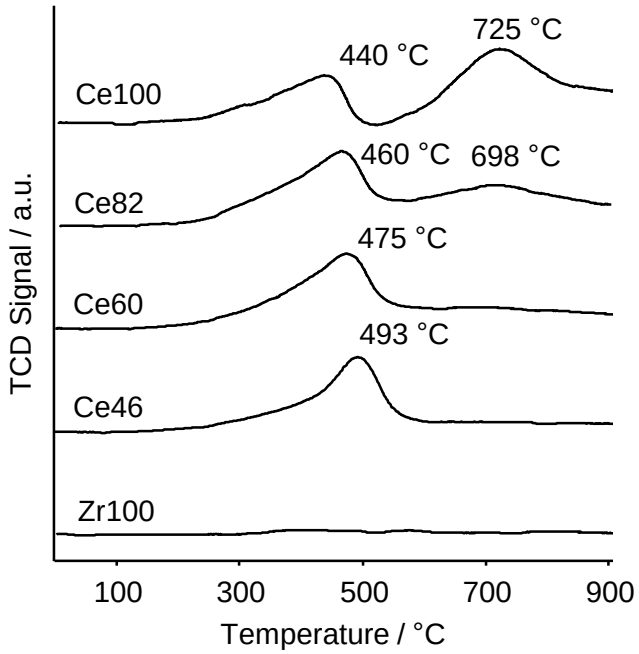

Figure 3.1 TPR of ceria-zirconia catalysts calcined at 500 °C.

No hydrogen consumption was observed for pure zirconia (Figure 3.1). Pure ceria had two main peaks from hydrogen consumption at 440 ℃ and 725 ℃. The low temperature peak at 440 ℃ can be attributed to surface reduction, while the high temperature peak is assigned to bulk reduction [44]. Addition of zirconia caused the high temperature ceria peak to shift to lower temperatures. Consequently, bulk reduction was difficult to distinguish from surface reduction in ceria-zirconia mixed oxides. A shoulder formed at the low temperature side of the first peak and its intensity depended on the amount of zirconia that was incorporated into the crystal lattice. This indicated that

surface reduction was occurring at lower temperatures with the incorporation of zirconia. The maximum of the low temperature peak shifted to higher temperatures as the amount of zirconia was increased due to an increasing contribution of reduction of the bulk oxide.

3.3.1.3 Low temperature oxygen storage capacity

The concentration of oxygen vacancies formed during reduction at 200, 300 or 450 °C was quantified by titration with O_2 (Table 3.2).

Table 3.2 Number of oxygen vacancies for mixed oxides at 200, 300 and 450 °C.

Composition of Mixed Oxide	Number of Oxygen Vacancies ($\mu mol*g^{-1}$)		
	200 °C	300 °C	450 °C
Ce100	0	80	276
Ce82	0	146	596
Ce60	0	144	780
Ce46	0	92	656
Zr100	0	0	0

As expected, no oxygen vacancies were formed on zirconia over at any temperature studied. At 200 °C, no oxygen consumption was measured for any ceria based samples. However, from the TPR experiment, some amount of hydrogen was consumed by all ceria based samples below 200 °C. This observation is significant because it shows that hydrogen is adsorbed on the surface before the reduction of the surface begins. It also indicates that adsorbed hydrogen does not contribute to the consumption of O_2 during titration. At 300 °C, a notable number of oxygen vacancies were formed for ceria and all ceria-zirconia samples. The concentration of oxygen vacancies per mass of catalyst was the highest for Ce82 and Ce60. At 450 °C, a significantly larger number of oxygen vacancies were formed for all samples (Table 3.2). The quantity of oxygen vacancies in

ceria-zirconia were at least 2 times that of ceria. The largest number of vacancies was found for Ce60.

3.3.2 Reactivity for HDO of guaiacol

3.3.2.1 Stability of catalysts

Tests for stable catalytic performance started at the highest temperature of 375 °C. The temperature was lowered by 25 °C every 10 hours until the temperature of 275 °C was reached. Finally, the temperature was increased back to 375 °C, and the reactivity was compared to the start of the run to probe whether catalyst deactivation had occurred. Over a 72 hour reaction, the change in conversion was less than 2% for all catalysts tested. This indicated that none of the catalysts were deactivated over the course of the reaction.

3.3.2.2 Product distribution over different catalysts

The conversion of guaiacol and the corresponding product distribution over different ceria and ceria-zirconia catalysts was compared at 375 °C and a W/F of 1.4 h (Table 3). Over ceria, the product mixture contained 67 mol% phenol, 10 mol% catechol, 7 mol% cresols, and 1 mol% benzene. Methanol and methane were not detected as products for Ce100. The lack of methanol in the product stream can be tentatively explained by consumption to produce cresols as well as methanol decomposition to produce CO and hydrogen [116]. The selectivity to phenol increased with increasing zirconia content of the catalyst. Cresols were the other major products over the mixed metal oxide catalysts. In addition, limited amounts of anisole, catechol and methanol

were formed. Oligomeric products were not formed in detectable quantities over ceria zirconia catalysts at 375 °C and a W/F of 1.4 h. Only a small amount of benzene was found in the product stream on pure ceria and ceria-zirconia.

Table 3.3 Product distribution for HDO of guaiacol at 375 °C, 1 bar, and W/F = 1.4 h.

	Conversion	Product distribution / mol%			
Mixed Oxide		Phenol	Benzene	Cresols	Catechol
Ce100	37	67	1	7	10
Ce82	59	73	1	19	0
Ce60	67	88	1	10	0
Ce46	46	93	0	6	0

3.3.2.3 Influence of weight to feed ratios (W/F)

To elucidate the reaction path of guaiacol, the product distribution over Ce82 at 400 °C and 1 bar was studied as a function of W/F (Figure 3.2). The W/F of the liquid feed was varied from 0.1 to 11.2 h.

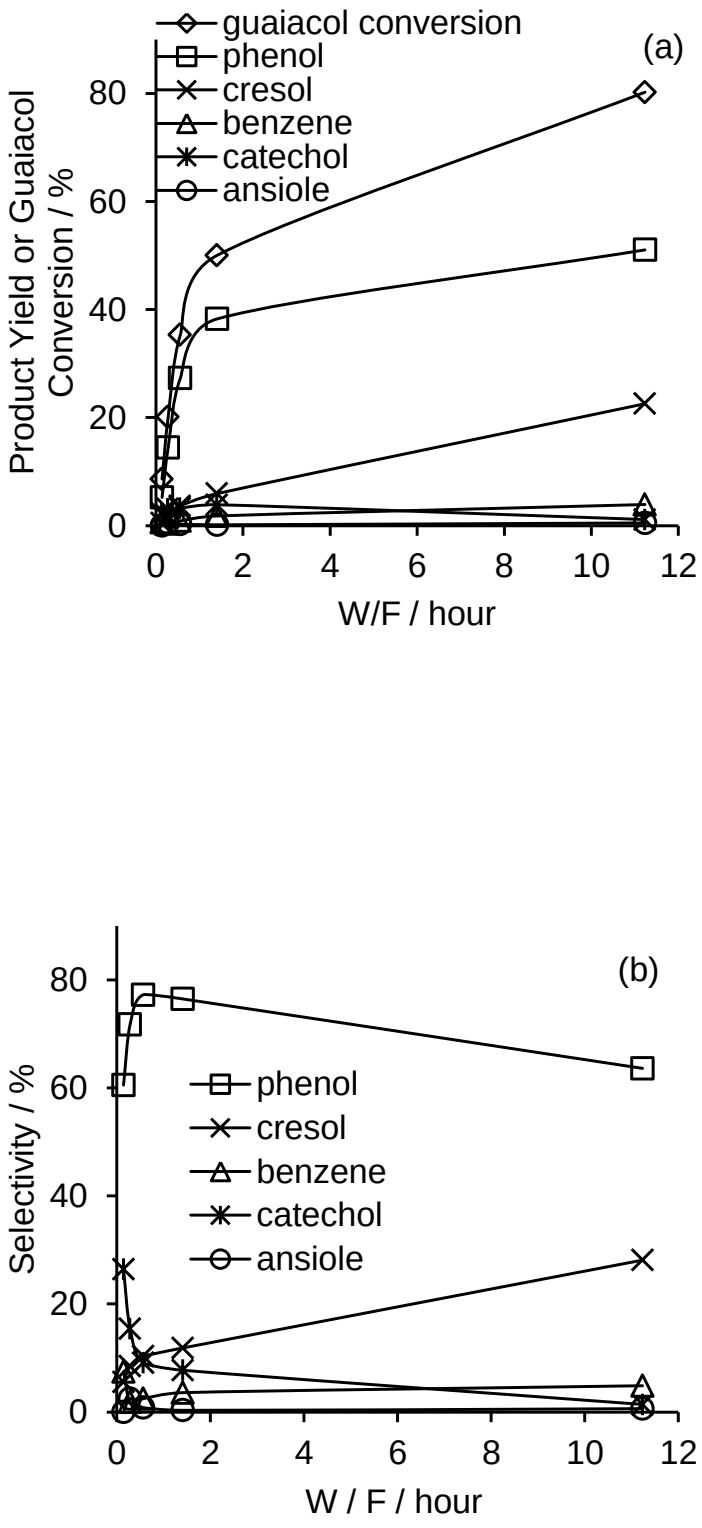

Figure 3.2 (a) Product yield and (b) selectivity of 0.5 g of Ce82 over varying W/F.

As the W/F decreased, the conversion of guaiacol to products decreased. Phenol was the major product under all reaction conditions tested. At low W/F, the yield of catechol was greater than at high W/F. This indicates that catechol is a primary product of guaiacol (Figure 3.2). The yield of cresols decreased with decreasing W/F. Benzene remained a minor product over the range of W/F tested, although the benzene yield steadily increased as the W/F increased.

More information about the reaction network can be obtained from the selectivity to different products (Figure 3.2b). The selectivity to catechol was 28% at the lowest W/F and decreased as the W/F increased. The selectivity towards phenol increased initially with increasing W/F and then began to increase as the W/F increased further. As the phenol selectivity decreased at high W/F, the increase of the selectivity towards cresols became much more pronounced. This observation implies that cresols are produced from phenol as well as from guaiacol. The selectivity towards benzene increased steadily with increasing W/F, but remained below 0.1 even at the highest W/F tested.

An additional experiment was conducted, in which methanol (4.4 $g*L^{-1}$) and phenol (12.8 $g*L^{-1}$) were co-fed over Ce82 at 400 °C and 1 bar and a W/F of 1.4 h. The products found were 90 mol% cresols and 10 mol% benzene. No guaiacol was detected indicating that the deoxygenation of guaiacol to phenol is irreversible and that phenol can be alkylated by methanol. Methanol was not observed in the product stream even though the consumption of methanol for the production of cresols did not account for the entire amount of methanol fed.

3.3.2.4 Influence of temperature

All catalysts exhibited guaiacol conversion over the entire temperature range studied (i.e. 275 – 375 °C). For Ce100, the conversion increased from 2% to 37% as the temperature increased from 275 to 375 °C. At 300 °C and above, all mixed oxides

displayed higher conversion than ceria at the same temperature (Table 3.4). The highest conversions were observed for Ce60 and Ce82. At 375 °C, 67% and 57% of the guaiacol were converted over Ce60 and Ce82, respectively.

Table 3.4 Conversion of guaiacol over ceria-zirconia mixed oxides.

	Conversion (%)					E_a ($kJ*mol^{-1}$)
	275 °C	300 °C	325 °C	350 °C	375 °C	
Ce100	2	2	5	15	37	131
Ce82	3	10	22	39	59	97
Ce60	5	8	24	40	67	111
Ce46	0	5	16	27	46	114

(a)

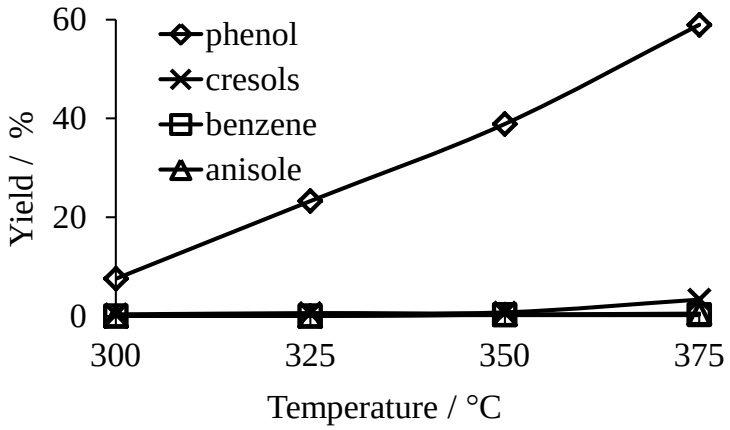
60
40
20
0
Yield / %
phenol
cresols
benzene
anisole
300
325
350
375
Temperature / °C

(b)

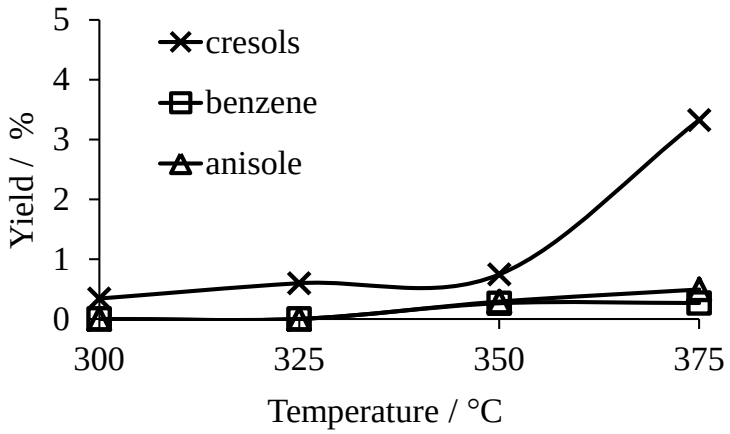
5
4
3
2
1
0
Yield / %
cresols
benzene
anisole
300
325
350
375
Temperature / °C

(c)

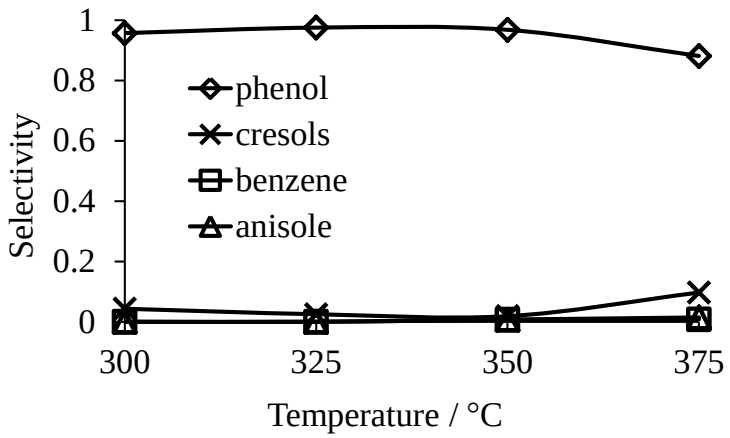

Figure 3.3 (a) Major and (b) minor product yield and (c) selectivity of Ce60.

The yield and selectivity of different products changed with temperature for all ceria-zirconia catalysts. Product distribution for Ce60 is shown in Figure 3.3. The major product at all temperatures was phenol. As temperature increased, the phenol yield increased (Figure 3.3a). The selectivity to phenol began to decrease slightly above 350 °C, while the selectivity towards cresol increased. The yield of cresol was very low up to 350 °C (Figure 3.3b). Benzene and anisole were not detected below 325 °C.

The apparent activation energy for guaiacol conversion over all catalysts was estimated based on the reactivity data between 300 and 375 °C (Table 3.3). The conversion at 275 °C was neglected as the values were too close to the experimental error of the gas chromatograph. The activation energies were calculated based on the simplifying assumption that guaiacol is converted in a single first-order reaction. An apparent activation energy of 131 kJ*mol^{-1} was found for Ce100. The apparent activation energies for the ceria-zirconia catalysts were between 97 and 114 kJ*mol^{-1} and followed the order Ce82 < Ce60 < Ce46.

3.4 Discussion

3.4.1 Structure-property relationships for HDO over ceria zirconia

Hydrodeoxygenation catalysts must be able to cleave C-O bonds and provide dissociatively adsorbed hydrogen to replace the removed oxygen atoms. The most commonly discussed mechanism for HDO over supported noble metal catalysts involves oxygen removal by acid catalyzed dehydration and metal catalyzed hydrogenation of C=O and C=C bonds[22, 98, 117, 118]. For sulfided NiMo and CoMo catalysts, an inverse Mars-van Krevelen mechanism has been suggested, in which the oxygen containing functional groups of the reactant coordinate to defect sites of the sulfide particles [51, 108, 111]. Unfortunately, sulfide catalysts suffer from deactivation when sulfur atoms are replaced by oxygen during HDO [16, 119]. Therefore, oxides with comparable sites have great potential as catalysts for HDO [51].

Chapter 2 demonstrates that hydrogen is readily activated over ceria and ceria-zirconia catalysts. Specifically, isotopic scrambling between H_2 and D_2 occurs over these catalysts at considerable rate, and the activation energy is approximately 23 $kJ \cdot mol^{-1}$ when oxygen vacancies are involved. Up to 10.5 hydrogen atoms per nm^2 participated in isotopic scrambling at 300 °C. Based on these results, it is safe to assume that HDO reactions over these catalysts are limited by the amount of hydrogen on the surface, when the reaction is performed in a hydrogen rich atmosphere.

In addition, ceria-based catalysts have a substantial oxygen storage capacity in the temperature of interest for HDO (Table 3.2). Specifically, Table 3.2 shows that oxygen vacancies start forming between 200 and 300 °C in a reducing atmosphere. In this temperature range, oxygen vacancies are generated on the surface by the condensation of

singly-bound hydroxyl groups [81]. Once the temperature is around 327-467 °C, bulk oxygen atoms become mobile and migrate to the surface [44, 52]. In this temperature range, bulk and surface reduction become difficult to distinguish. The incorporation of zirconia increases the oxygen storage capacity notably. Zirconium has a slightly smaller ionic radius than cerium and it causes a slight strain in the ceria-zirconia crystal lattice that allows more oxygen defects to form than in pure ceria at the same conditions [52, 53]. Consequently, ceria-zirconia catalysts fulfill all requirements for an HDO catalyst.

The reactivity studies show that this potential translates into catalytic activity for HDO of guaiacol. The catalytic activity became notable at approximately the same temperature (i.e. around 300 °C) as the formation of oxygen vacancies. Guaiacol conversion over ceria zirconia catalysts was higher than over pure ceria over the entire temperature tested, and it increased with increasing temperature as expected (Table 3.4). While differences in surface area might account for some of the differences in activity, they are insufficient to account for the differences by themselves. In fact, a linear correlation was observed between the concentration of oxygen vacancies at 300 °C and guaiacol conversion at the same temperature (Figure 3.4). Note that at 300 °C the conversion of guaiacol was still low enough to provide differential conditions. The correlation between the concentration of oxygen vacancies and the activity of the catalyst is a clear indication that oxygen vacancies play a critical role in the conversion of guaiacol. However, the trend line in Figure 3.4 had an intercept at a vacancy concentration of 24.6 μmol O_2*g^{-1} indicating that a minimum density of defect sites is required for catalytic activity. I speculate that two oxygen vacancy sites are necessary to deoxygenate guaiacol to produce phenol. In order for oxygen removal to occur over ceria-based catalysts, the defect sites must coordinate the two O-H functional groups in guaiacol. This means that the vacancy sites must be close enough to each other to activate the C-O bond in sterically hindered guaiacol. Thus, a minimum density is required to observe guaiacol conversion.

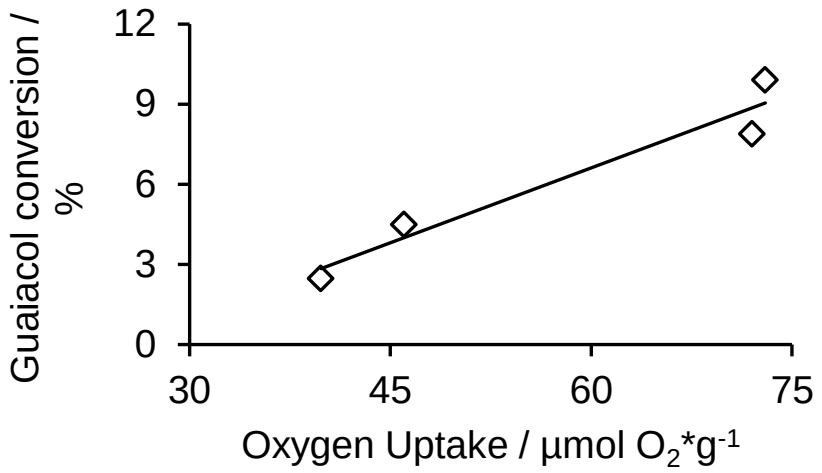

Figure 3.4 Comparison of the concentration of oxygen vacancy sites (Table 3.2) and guaiacol conversion over ceria and ceria-zirconia at 300 °C (Table 3.4).

Differences in the concentration of surface oxygen vacancies could explain the differences in activity over different catalysts at higher temperatures (Table 3.3). Specifically, the same conversion was observed over Ce60 and Ce82 up to 350 °C, while the conversion was significantly higher over Ce60 at 375 °C. A similar trend was observed for the oxygen storage capacity over these catalysts at different temperatures (Table 3.2). However, it is not possible to directly quantify the number of oxygen vacancy sites on the surface with oxygen titration above approximately 330°C due to increasing mobility of bulk oxygen atoms [44, 52]. Consequently, titration with O_2 at 450 °C will likely also saturate sub-surface and bulk vacancies. Thus, the oxygen titration experiment at 450 °C determines an upper limit for the number of oxygen vacancies that

are available as active sites at the surface. Note that it is possible that sub-surface vacancies could have an influence on the catalytic performance in HDO reaction reactions, but this phenomenon is beyond the scope of this work.

3.4.2 Apparent activation energy

Reports on apparent activation energies for HDO vary over a considerable range even when catalysts with similar are compared [22, 120]. For example, for HDO of guaiacol over sulfided CoMo and NiMo supported on Al_2O_3 values of 50-112 $kJ*mol^{-1}$ have been reported depending on the reaction conditions [22]. HDO of guaiacol on transition metal phosphide hydroprocessing catalysts had activation energies of 23-63 $kJ*mol^{-1}$ [120]. In most studies, apparent activation energies are calculated based on simplifying assumptions. In particular, the conversion of a reactant is treated as a single, first-order reaction, whereas parallel reactions of different orders may well be involved. In addition, it has to be considered that the concentration of active sites may be a function of the reaction temperature. Specifically, the generation of defect sites in sulfide and oxide catalysts can be facilitated at elevated temperature, and it has been proposed that these are the active sites for the inverse Mars-van Krevelen mechanism over such catalysts [51].

It is recognized that the issues outlined above will likely affect the apparent activation energies for HDO of guaiacol over ceria-based oxide catalysts. Nevertheless, apparent activation energies were determined based on the assumption of a single, first-order reaction to provide a semi-quantitative comparison with other types of catalysts. Ceria-zirconia mixed oxides had activation energies between 97-114 $kJ*mol^{-1}$, which is within the range found for sulfided CoMo and NiMo catalysts. However, it is significantly higher than the activation energy reported for transition metal phosphides [120]. Zhao et. al. reported values of 23-63 $kJ*mol^{-1}$ for HDO of guaiacol. The low

activation energy was speculated to be the result of hydrogenation of the aromatic ring followed by the elimination of water. Comparison with the apparent activation energy for pure ceria (131 $kJ*mol^{-1}$) shows that the incorporation of a certain amount of zirconia lowers the apparent activation energy. I speculate that the decrease in the crystallite size that occurs with zirconia addition lowers the activation energy for the mixed oxides. It is well known that a decrease in the crystallite size also increases the number of oxygen defect sites due to preferential reduction at corner and edge sites [95]. A smaller crystallite size will not only increase the number of oxygen defect sites available for reaction, it will allow for more oxygen defect sites to be close enough to bind the two oxygen containing functional groups present in guaiacol. However, the apparent activation energy increased with increasing zirconia content of the mixed metal oxides. I speculate that this is due to a change in the Lewis acidity of the surface. It has been speculated that Lewis acidity is responsible, at least in some part, for HDO activity [16].

3.4.3 Reaction network for HDO over ceria-zirconia catalysts

Hydrodeoxygenation of guaiacol has been studied over a variety of different catalysts, including sulfided NiMo and CoMo [105, 121], noble metals [117, 122], nitrides [123], phosphides [120], and oxides. However to my knowledge, no work has been done on HDO of guaiacol over reducible metal oxides. Guaiacol is an ideal model compound for assessing the performance of different catalysts because it is a major constituent of pyrolysis oils as well as one of the most difficult methoxyphenols to deoxygenate [22]. Several reaction networks have been suggested [16, 117, 122]. The bond energies of the C-O bonds in guaiacol increase in the order H_3C-OAr < MeO-Ar < HO-Ar [21]. Thus, it is not surprising that the hydrogenolysis of the H_3C-OAr bond (i.e. demethylation) was proposed as the first step in many reaction paths. Catechol and methane are formed in this reaction. Methane was observed over various catalysts

including Pt-Sn monoliths,[117] sulfided $CoMo/Al_2O_3$ [21, 105], Pt/MgO [124], and Fe/SiO_2 [125]. In many cases, demethylation activity is attributed to the metal sites on these catalysts [117, 122]. An alternative pathway is the demethoxylation (i.e. cleavage of the MeO-Ar bond) to produce phenol and methanol. This pathway was observed over CoMo sulfides supported on alumina and zirconia [51, 100, 121, 126] Bui et al. reported that this reaction step is favored over catalysts with amphoteric support, such as zirconia [21]. The primary reaction products can be dehydroxylated to ultimately yield completely deoxygenated products. However, over many catalysts, the aromatic ring must be hydrogenated before the last –OH group can be removed in a dehydration step [127]. In addition to deoxygenation, transalkylation reactions are often observed during HDO of guaiacol, in particular, over Lewis acidic catalysts [128]. Consequently, the major reaction products in different HDO studies included phenol, catechol, cresol, benzene, cyclohexane, and cyclohexene [129].

While most studies on HDO of guaiacol were conducted over supported metals on metal oxides or sulfided catalysts, there were a limited number of reports on oxide catalysts. Hydrodeoxygenation of acrolein, acetone, hexanone, cyclohexane, and anisole was performed over a metal free MoO_3 [50, 51]. In case of anisole as a reactant, deoxygenated aromatic products were formed with significant yields, while no products saturated rings were detected [51]. MoO_3 accumulated a certain amount of coke, but it was readily regenerated by calcination. The concentration of oxygen vacancies was found to play a critical role for the HDO activity of MoO_3 [50]. Ceria-zirconia is a well-known redox catalyst that easily forms vacancy sites, and its reducibility can be tuned by adjusting the Ce:Zr ratio and by controlling the morphology of the sample [91]. Thus, it provides a unique opportunity for studying the involvement of oxygen vacancies in different paths for HDO.

The reaction pathway of guaiacol over the present ceria-zirconia catalysts can be derived from the changes of the yields to different products as a function of contact time

(Figure 3.2). When the curves are extrapolated to the origin, positive slopes are obtained for phenol and catechol indicating that these compounds are primary products of the conversion of guaiacol. At the lowest W/F of 0.14 h, the yield to phenol was 2.3 times higher than the yield to catechol, which shows that the demethoxylation of guaiacol to phenol is faster than the demethylation to cresol. This observation is in line with a previous report, in which the amphoteric character of zirconia was proposed to favor the demethoxylation of guaiacol [128]. Moreover, the lack of detectable quantities of methane in the product stream is in agreement with the limited relevance of the demethylation path. Methanol, which is formed during the conversion of guaiacol to phenol, is converted in other reactions (vide infra). Not surprisingly, the low yield to anisole showed that the cleavage of the strong HO-Ar bond in guaiacol was not kinetically relevant [21].

The maximum of the catechol yield at intermediate contact times showed that this species is further deoxygenated to form phenol. Consequently, only limited amounts of catechol were found as the contact time increased. In contrast to the high reactivity of catechol, the deoxygenation reaction of phenol to benzene was slow, and the benzene yield never exceeded 3.9 even at the largest W/F of 11.2 h. Similar observations were reported for the deoxygenation of guaiacol and the intermediate cresol over a vanadium oxide on alumina catalyst [130]. It was proposed that the oxygen atoms in the 1,2 positions on the aromatic ring form a chelated complex with a partially reduced vanadium atom. Since the redox activity of vanadia and ceria-based oxides is comparable, I suggest that the same mechanism is relevant for the catalysts in the present study. It is interesting to note that guaiacol was less reactive than anisole over Pd/C in the presence of H_3PO_4, which was explained with the stabilization of the carbocation transition state by the adjacent hydroxyl group [98].

Due to the absence of the activating chelate interaction, the cleavage of the last Ar-OH bond is slow as indicated by the high yields to phenol and limited benzene yields.

The Ar-OH bond is the strongest C-O bond in guaiacol (and other phenol derivatives), and several studies suggested that that it needs to be weakened by hydrogenation of the aromatic ring before it can be cleaved [98, 110, 131]. In the present study, the product stream contained no partially or completely hydrogenated ring structures, while benzene was formed in limited amounts. This shows that ceria-zirconia catalysts have some activity for complete HDO of guaiacol without hydrogenation of the aromatic ring. I speculate that this activity could be enhanced by the presence of surface sites, which interact with the aromatic ring while the phenol group binds to an oxygen vacancy.

In addition to HDO, phenol can undergo a transalkylation to different cresol isomers (Figure 5[98, 131]. Several studies reported that this reaction requires Lewis acidic sites that facilitate the formation of a methyl cation as transition state of the alkylation reaction [21, 128, 132]. On the other hand, it was proposed that amphotheric metal oxides, such as ceria, are good catalysts for the ortho-methylation of phenol with methanol[133]. I speculate that the surface methoxy species resulting from the conversion of guaiacol to phenol can react with an oxygen vacancy to be reduced to surface bound methyl groups, which participate in the transalkylation reaction.

Another important observation from the co-feeding of methanol and phenol is that of the irreversibility of the deoxygenation of guaiacol. While methanol was found in the product mixtures under some conditions, its concentration was never significant. As mentioned above, surface methoxy species are consumed in the alkylation of phenol to produce cresol. However, production of cresol does not account for all of the methoxy species/methanol produced by methoxylation of guaiacol. The likely explanation for this observation is that methanol can be decomposed over ceria-based catalysts to produce CO and H_2[116]. With the instruments available for the present study, it was not possible to detect CO and H_2.

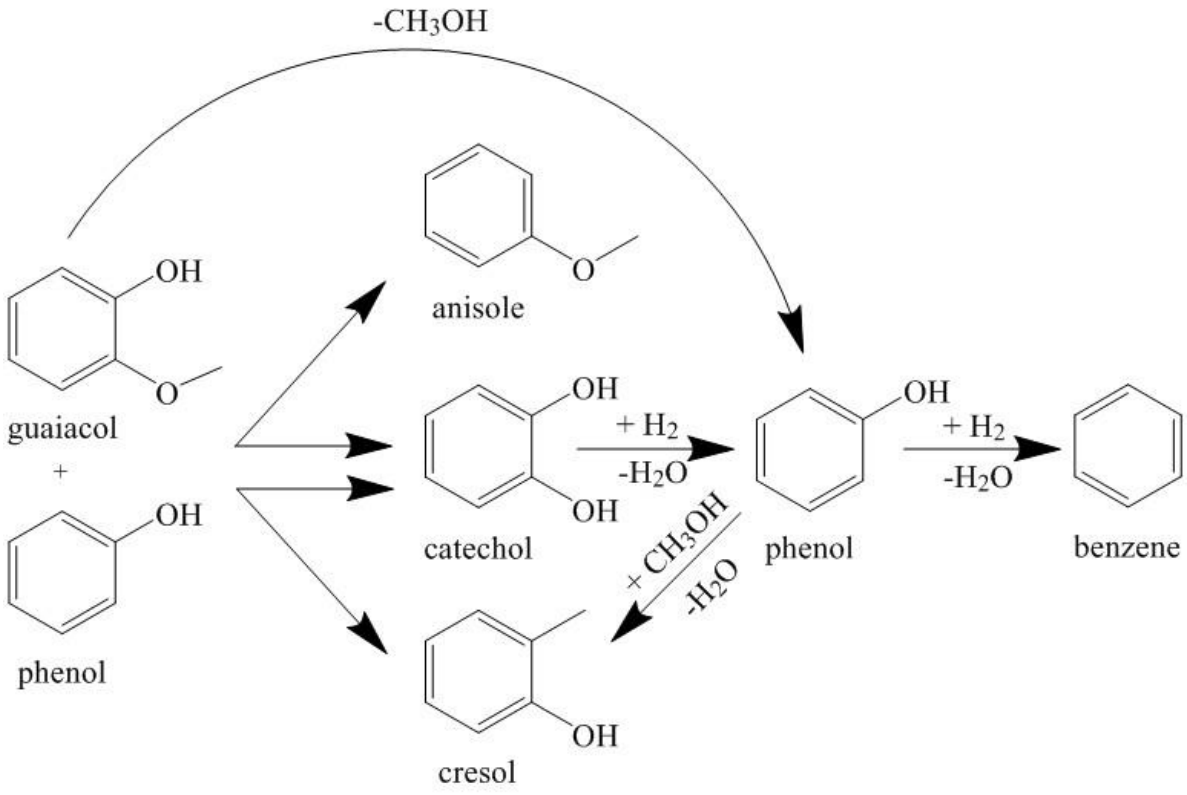

Figure 3.5. Reaction scheme for the deoxygenation of guaiacol to products.

3.4.4 Stability of catalytic activity

In many studies, it was shown that traditional HDO catalysts are deactivated by rapid coke formation. [22] The same problem was reported for ceria catalysts during wet oxidation of phenol at 120 - 160 °C [134, 135]. In the present study, oligomeric products were only detected over pure ceria, while no such species were detected over the ceria-zirconia catalysts. Since even the ceria catalyst showed stable activity for 72 h, it is safe to suggest that the oligomeric products do not cause deactivation under the experimental condition applied in this study.

In addition to coking, the loss of active sites has to be considered. Specifically, water is always formed as a by-product in HDO, and water dissociatively adsorbs on

ceria-zirconia surfaces saturating defects sites [136]. Therefore, it is imperative to perform HDO reactions over ceria-zirconia catalysts under reaction conditions that allow for surface reduction and, thus, the regeneration of defect sites. The sustained activity observed over all ceria-based catalysts in this study shows that it is achieved above approximately 300 °C under 1 bar of hydrogen (Table 3.4).

3.5 Conclusions

Ceria-zirconia catalysts had a higher conversion of guaiacol to deoxygenated products as well as a higher selectivity towards phenol than pure ceria. They did not deactivate over the course of the reaction due to coking or due to the presence of water in the feed as other common catalysts HDO catalysts do. They did not produce any hydrogenated ring products indicating that, compared to traditional HDO catalysts, they did not consume as much hydrogen and, besides not needing supported metals, have the potential to be more economical. The reaction products that were found minimized the loss of carbon. Ceria-zirconia catalysts are promising HDO catalysts for the first step of deoxygenation.

Structure-property relationships exist between guaiacol conversion and oxygen vacancies. When more oxygen vacancies are present on the surface of ceria-zirconia a higher guaiacol conversion is achieved. At low temperatures, where oxygen mobility in the mixed oxide is low, oxygen titration experiments are sufficient to quantify the number of oxygen vacancies present on the surface. These parameters can be modified by changing the synthesis technique to optimize the amount of guaiacol converted as well as the product distribution.

Future work should address the second step of deoxygenation. Often, there is a trade-off between hydrodeoxygenation activity and ring hydrogenation. The most successful hydrodeoxygenation strategy will most likely be a combination of more than

type of catalyst in series possibly at different reaction conditions. Future work could also include increasing oxygen defect sites on the surface by synthesizing ceria-zirconia nanoparticles to increase guaiacol conversion.

CHAPTER 4

STABILITY OF RU/ ZRO_2 CATALYSTS FOR HYDROGENOLYSIS OF GLYCEROL IN HOT LIQUID WATER WITH ACIDIC AND BASIC PH

4.1 Background

Fuels and chemical production from renewable feedstocks are necessary to meet growing demands as petroleum diminishes in supply [4]. Thus, it is important to develop sustainable processes to produce value-added chemicals and fuels from a renewable source. Ligno-cellulosic biomass could be a good option as an alternative resource because it is very abundant and inexpensive, and bio-refineries are often implemented to integrate multiple processes to produce fuels and chemicals economically from renewable, carbon neutral feedstocks.[5, 12, 137] One of the major downsides to biofuel production is the high cost. However, this cost can be decreased if the by-products or waste can be transformed into valuable co-products [137].

One biofuel currently commercially available is biodiesel. Biodiesel is comprised of fatty acid methyl esters (FAME) produced through base-catalyzed transesterification of triglycerides with methanol [12, 138, 139]. The transesterification reaction also produces crude glycerol, which contains 50% glycerol and other impurities with a pH of 9.7-10.4 [140, 141]. Some of these impurities include 12-16 wt% alkalis in the form of alkali hydroxides and soap and 8-12 wt% methanol [141]. These impurities can cause water pollution and other environmental problems, and the cost for disposal of crude glycerol is high [142]. There is a market for glycerol in the cosmetics industry; however, the demand for glycerol only comprises a fraction of the current biodiesel production. Glycerol was identified by the DOE as a top-12 building block chemical that can be

converted to a high-value biomass derived chemical [13]. For these reasons, it has been suggested that glycerol upgrading to valude-added chemicals be pursued to make biodiesel production more economical [5]. Thus, it is important to study glycerol upgrading to improve the economics of a bio-refinery in an effort to make biodiesel production more cost effective.

One method of upgrading glycerol is through hydrogenolysis to produce ethylene glycol and propylene glycol. Ethylene glycol is produced by cleavage of a carbon-carbon bond which yields methanol which degrades into methane [13]. Propylene glycol is 1,2-propandiol of glycerol and 1,3 propandiol produced through cleavage of a carbon-oxygen bond in glycerol [14]. Industrially, both propanediols are high added-value chemicals and are primarily produced from nonrenewable petroleum based sources, and thus, it is highly desired to find an alternative production route [15].

Glycerol hydrogenolysis has been studied extensively in literature [14, 15, 25, 26, 143, 144]. The reaction is typically carried out in liquid phase in a batch reactor at pressures from 3.0-4.5 MPa of H_2 and approximately 200 °C. Common supports include activated carbon, acidic zeolite and zirconia [13, 15, 138, 145, 146].Supported metals such as Pt, Ru and Rh are the active metal phase for catalytic activity, and as the active component, surface acidity and basicity change so do the intermediates and reaction pathways [13, 25].

Although some progress has been made towards understanding glycerol hydrogenolysis, almost all of the literature focuses on reactivity of catalysts with pure glycerol. One study on upgrading crude glycerol exist, and the final conclusion is that catalysts must show resistance to fatty acids and alkali metals which alter the pH of the aqueous medium [147]. Because of this, it is important to examine the effects of different aqueous solutions at various pHs to mimic realistic conditions in a biorefinery for upgrading glycerol. Most importantly the stability of the catalysts under such conditions must be assessed and improved if needed.

This chapter of the thesis focuses on the effects of acidic and basic aqueous environments on Ru/ZrO_2, a typical glycerol hydrogenolysis catalyst known for producing propylene glycol and ethylene glycol. The catalysts were exposed to hot liquid water at different pH at 225 °C for 72 hours and characterized by a suite of physicochemical techniques before and after the hydrothermal treatment. Glycerol hydrogenolysis was used as a test reaction to determine the effects of hydrothermal treatment on reactivity and thus hydrothermal stability.

4.2 Materials and methods

4.2.1 Chemicals

A monoclinic ZrO_2 (catalog number: 4385) was purchased from Alfa Aesar. $RuCl_3$ (catalog number: 208523), acetic acid (ACS Reagent >99.7%), NaOH (ACS Reagent >97.0%), glycerol (>99.5%), ethylene glycol , and propylene glycol were purchased from Sigma Aldrich. All of these compounds were used without further purification. Hydrogen was purchased from Airgas with ultra-high purity (UHP Grade 5). Deionized water was purified to 18.2 MΩ/cm with a Barnstead NANOpure ultrapure water system.

4.2.2 Catalyst preparation

All catalysts were prepared by incipient wetness impregnation of $RuCl_3$ on ZrO_2 [148]. The quantity of water necessary for synthesis was determined by adding deionized water to 1 gram of ZrO_2 until the sample appeared wet. The quantity of water was scaled up for the desired quantity of catalyst. The $RuCl_3$ precursor was dissolved in deionized water and added to 20 grams of ZrO_2. The mixture was stirred for 1 hour. The resulting solid was dried for 12 hours at 100 °C. After drying, the samples were heated to 400 °C at 5 K/min for 3 hours in 100 mL/min of 10 mol% hydrogen in argon.

4.2.3 X-ray diffraction

A Philips X'pert diffractometer equipped with an X'celerator module using Cu Kα radiation (λ = 1.54 Å) was used to measure powder x-ray diffraction (XRD) patterns. Diffractograms were measured from 2θ = 8-80° with 0.016711° as the step size. The Scherrer equation was used to calculate crystallite size for zirconia using the largest peak of 2θ = 28.2° [57-59].

4.2.4 Nitrogen Physisorption

A Micromeritics ASAP2020 physisorption analyzer was used to perform nitrogen physisorption at -196 °C. Before analysis, each sample (ca. 0.30 g) was degassed under vacuum at 200 °C for 2 hours. The Brunauer-Emmet-Teller (BET) surface area was calculated from the nitrogen adsorption between $0.05 \leq P/P_0 \leq 0.3$ [60]. The Barrett-Joyner-Halenda (BJH) method was used to calculate the pore volume [61]. The experimental error was assessed by repeating the analysis of Ru/ZrO_2 hydrothermally treated at pH 7 multiple times and was found to be ± 2.9%

4.2.5 H_2 chemisorption

H_2 chemisorption was performed on a Micromeritics ASAP2020 physisorption analyzer at 308 K and 10-30 kPa of H_2. Before analysis the samples were treated in flowing 10 mol% H_2/Ar at 623 K for 2 hours and subsequently evacuated at the same temperature for 2 hours. The experimental error was quantified with a 5 wt% Pt/Al_2O_3 standard and was found to be ± 2.2%.

4.2.6 Pyridine adsorption followed by infrared (IR) spectroscopy

Pyridine adsorption followed by IR spectroscopy was studied using a Nicolet 8700 Fourier transform (FT) IR spectrometer with a MCT/A detector. The samples were pressed into self-supported wafers and loaded into a custom built vacuum chamber. The catalyst was first activated at 450 ^{o}C and < 10^{-6} mbar for 1 hour (heating rate 10K/min). The temperature was then lowered to 150 ^{o}C, and a background spectrum was collected. Pyridine was dosed into the chamber at 0.1 mbar for 20 min until adsorption equilibrium was reached. The chamber was then evacuated for 30 min until desorption equilibrium was reached and a spectrum was collected. The acid site concentration at 150 ^{o}C was defined as the total site concentration. The averaged extinction coefficients obtained from Tamura et.al. were used to quantify the amount of Lewis acid sites on the samples [149]. No Brønsted acidity was detected on any of the samples tested.

4.2.7 Scanning electron microscopy

Scanning electron micrographs were obtained using a LEO 1550 Thermally-Assisted Field Emission (TFE) Scanning Electron Microscope (SEM). The samples were deposited on carbon tape supported by an aluminum stub. All images were captured at 30,000x magnification and an accelerating voltage of 4 kV using Ziess Software.

4.2.8 Transmission electron microscopy

Transmission electron micrographs were obtained using a FEI Tecnai F30 TEM at 300 kV. The samples (c.a. 0.005 g) were suspended in 10 mL of acetone and placed in a sonicator for 10 minutes. After 10 minutes, one drop of each sample was deposited on a 200 mesh carbon coated copper grid and allowed to dry at room temperature for 72 hours.

4.2.9 Stability studies

Hydrothermal treatments of ruthenium on zirconia were performed in a Teflon-lined autoclave. Approximately 2 g of reduced sample were used in a slurry of deionized water (20 mL) degassed with nitrogen and adjusted to pH 3, 5, 7, 9 or 11 with acetic acid or sodium hydroxide. The reduced samples were loaded into the Teflon liners and degassed in a glove box with nitrogen for 30 minutes. After sealing the autoclave, the samples were loaded into a rotary oven and heated at 225 °C for 72 hours. The vapor pressure of water under these conditions is 25 bar [150]. Since the fraction of evaporated water is minor, it is safe to assume that the catalyst samples are covered by liquid water during the hydrothermal treatment. The samples were removed and cooled in flowing water. The samples were then filtered, rinsed with deionized water and dried in an oven overnight at 100 °C.

4.2.9 Reactivity studies

The following procedure was adapted from Wang et. al. [25]. The catalytic activity of the different Ru/ZrO_2 samples for hydrogenolysis of glycerol was dertermined at 200 °C under 60 bar of hydrogen pressure. An aqueous slurry of Ru/ZrO_2 (c.a. 0.3 g in 10 mL DI water) was loaded into a 100 mL Parr reactor. At room temperature, the free space was flushed with 20 bar of hydrogen for 10 minutes to remove any oxygen. Next, the slurry was heated to 200 °C over approximately 30 minutes. Once the autoclave reached 200 °C, the reaction was started by injecting a concentrated glycerol solution (c.a. 15 mL) under a hydrogen pressure of 60 bar, thus leading to a total glycerol concentration of 10 wt%. Aliquots were withdrawn from a liquid-sampling line over 3

hours. After each sample was taken, the reactor was re-pressurized to 60 bar with hydrogen. The samples were analyzed on an Agilent Technologies 1200 HPLC with a Refractive index detector (RID). Conversion of glycerol (X) as well as the yield (Y_p) and selectivity (S_p) to propylene glycol or ethylene glycol was calculated as:

$$X\,[\%] = \frac{C_{g,initial} - C_g}{C_{g,inital}} * 100 \tag{4.1}$$

Where $C_{g,\,initial}$ is the initial concentration of glycerol in mols*L^{-1} the batch reactor and C_g is the concentration of glycerol in mols*L^{-1} found in each aliquot.

$$Y_p\,[\%] = \frac{m_{c,p}}{m_{g,inital}} * 100 \tag{4.2}$$

Where $m_{c,p}$ is the number of moles of carbon found in the product of interest and $m_{g,consumed}$ is the number of moles of carbon consumed by glycerol conversion.

$$S_p\,[\%] = \frac{Y_p}{X} * 100 \tag{4.3}$$

4.3 Results and discussion

4.3.1 Physiochemical properties

Physicochemical properties of all samples are found in Table 4.1. The samples are abbreviated as Ru/ZrO_2-pH X where X is the pH during the hydrothermal treatment. ZrO_2 and Ru/ZrO_2 are defined as pure zirconia and 2 wt% ruthenium on zirconia without additional treatment. The BET surface area of the ZrO_2 support was 102 m^2*g^{-1}, and the pore volume and average pore width were 0.32 cm^3*g^{-1} and 12.1 nm, respectively. When Ru/ZrO_2 samples were prepared by incipient wetness impregnation, the BET surface area, pore width and pore volume decreased by 9%, 25% and 16%, respectively. The decrease in surface properties detected by nitrogen physisorption was most likely a result of reduction at 400 °C in the final step of the synthesis method. However, the formation of ruthenium particles in the mesopores of zirconia may have contributed to the decrease as well [151]. After treatment at 225 °C for 72 hours in acidic or basic aqueous solutions, the surface area and average pore volume decreased, while the average pore width increased. This indicates that the hydrothermal treatment caused smaller pores to merge together to produce fewer, large pores. No apparent correlation was found between the pH during the hydrothermal treatment and properties characterized by nitrogen physisorption.

Table 4.1 Physicochemical properties of ZrO_2 and Ru/ZrO_2 catalysts before and after treatments in hot liquid aqueous solutions[a]

Sample	BET Surface Area (m^2*g^{-1})	Pore Width (nm)	Pore Volume (cm^3*g^{-1})	Dispersion (%)[b]	Total Number of Lewis Acid Sites ($\mu mol*g^{-1}$)
ZrO_2	102	12.1	0.32	N.A.	N.R.[c]
Ru/ZrO_2	93	9.0	0.27	2.1	60
Ru/ZrO_2-pH 3	85	9.8	0.24	4.3	47
Ru/ZrO_2-pH 5	89	10.1	0.25	5.0	17
Ru/ZrO_2-pH 7	86	9.9	0.24	5.4	2
Ru/ZrO_2-pH 9	87	10.0	0.25	5.7	28
Ru/ZrO_2-pH 11	87	10.0	0.25	5.0	7

[a] All catalysts were reduced at 400 °C for 3 hours
[b] Calculated from H_2 chemisorption
[c] Not reported.

Figure 4.1 shows the x-ray diffraction (XRD) patterns of ZrO_2 and Ru/ZrO_2 samples. The diffraction peaks at 24.2°, 28.2°, 31.5° and 34.3° can be assigned to monoclinic ZrO_2 [152]. After ruthenium was supported on ZrO_2, the monoclinic crystal structure was retained. An additional peak at 44° can be attributed to the (101) plane of hexagonal close packed Ru [153]. The crystallite size for ZrO_2, Ru/ZrO_2 and all hydrothermally treated samples was ca. 9 nm as calculated by the Scherrer equation using the most intensive peak at $2\theta = 28.2°$. The crystallite size of zirconia did not change with metal loading or hydrothermal treatment, indicating that the bulk crystal structure of zirconia was stable under treatment conditions.

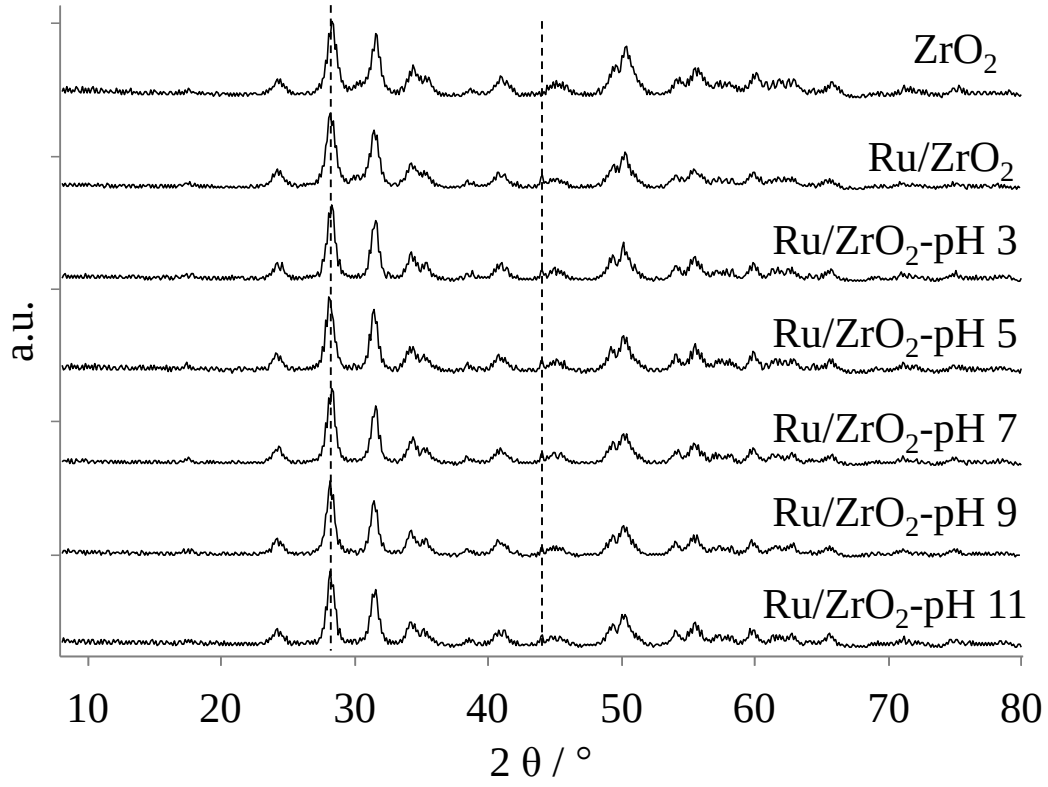

Figure 4.1 XRD patterns of ZrO_2 based samples.

While bulk properties of the support were not directly affected by hydrothermal treatments, there were changes to the surface of Ru/ZrO_2. The fresh Ru/ZrO_2 sample had a dispersion of 2.1% as determined by hydrogen chemisorption (Table 4.1). This value was notably higher after all hydrothermal treatments. As the pH of the hydrothermal treatment increased, the dispersion of ruthenium on the zirconia support increased until a pH of 11 where the dispersion decreased slightly. Importantly, even at neutral pH, the dispersion was 2.5 times that of the fresh catalyst. A pH of 6.9 was observed for a 10 wt% glycerol solution, which is one of the common feed compositions in literature [25, 154]. The change in dispersion after 3 hours of reaction conditions at pH 7 indicates the instability of the ruthenium particles on the surface during hydrothermal treatment.

Further supporting this observation, the Lewis acidity of the samples changed greatly (Table 4.1). Fresh Ru/ZrO_2 had the largest concentration of Lewis acid sites at 60 $\mu mol*g^{-1}$. The concentration of Lewis acid sites decreased during hydrothermal treatment under all conditions tested. The smallest concentrations of Lewis acid sites were found on Ru/ZrO_2-pH7 and Ru/ZrO_2-pH11. The impact of pH on the concentration of Lewis acid sites is not obvious with the data available. I speculate that there is a complex reorganization of the surface at an atomic level that is not possible to completely understand based on the current data set.

Analysis of the scanning electron micrographs of Ru/ZrO_2 before and after hydrothermal treatment revealed morphological changes to the surface on a 1 μm scale (Figure 4.2). The surface of the fresh Ru/ZrO_2 sample appeared similar to Ru/ZrO_2-pH3. Ru/ZrO_2-pH5 stood out from the other micrographs as the surface appeared the smoothest. As the pH of the hydrothermal treatment increased, agglomerates formed on the surface and it became increasingly rougher. The new features on the surface were not large enough to be detected by XRD, indicating that the hydrothermal treatments impact the surface structure, but the transformations do not propagate to the bulk.

(a)

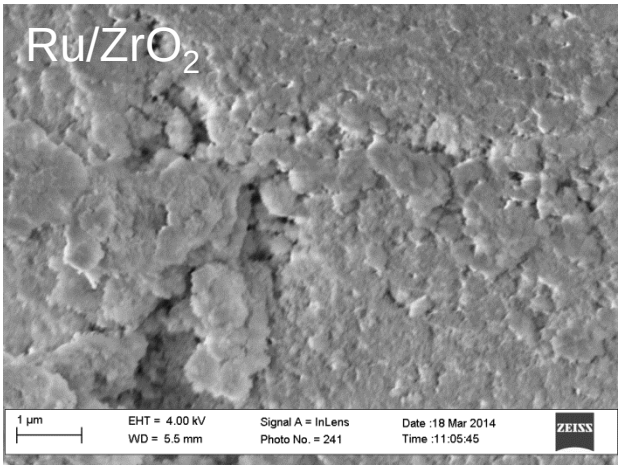

Figure 4.2 Scanning electron micrographs of Ru/ZrO_2 samples.

(b)

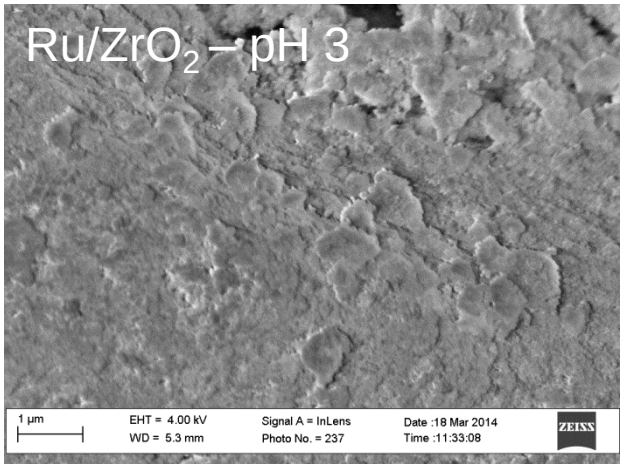

(c)

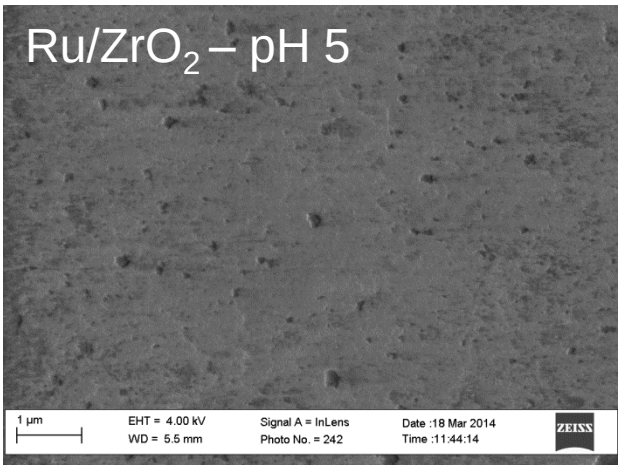

(d)

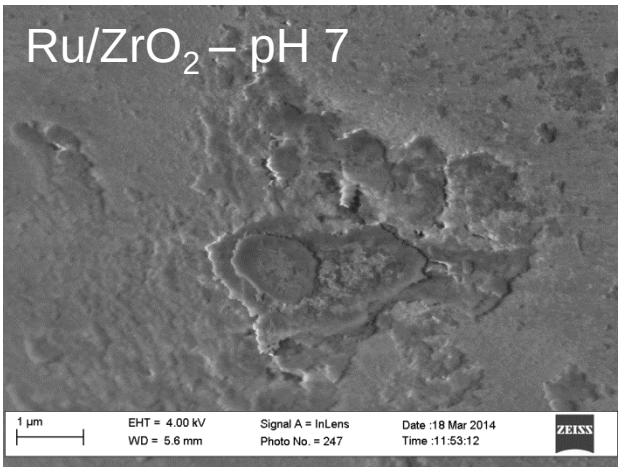

Figure 4.2 continued.

(e)

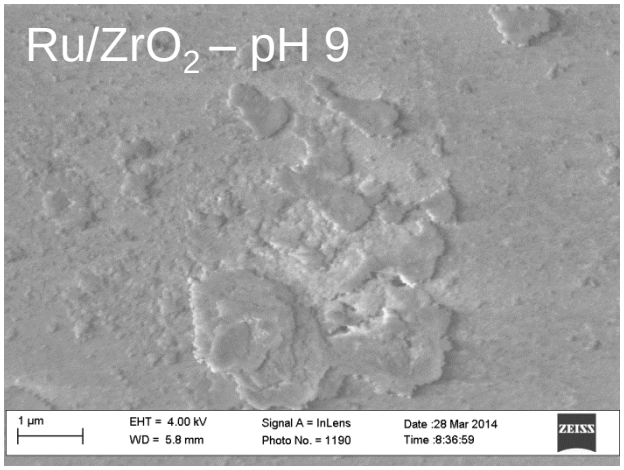

(f)

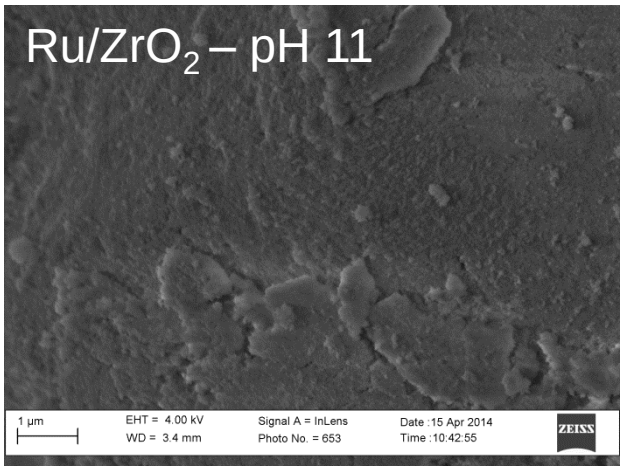

Figure 4.2 continued.

The effects of the hydrothermal treatments were also observed in transmission electron micrographs of fresh Ru/ZrO_2 (Figure 4.3). The first step in extracting meaningful information from a transmission electron micrograph is the identification the metal particles. For this purpose, energy dispersive x-ray spectroscopy (EDX) was used to distinguish between different elements. The EDX spectrum showed the presence of Zr,

Ru, Cu and C (Figure 4.3a). The presence of zirconium and ruthenium indicate that ruthenium is located on or near the surface of zirconia. The additional copper and carbon signals in the EDX spectra are attributed to the grid used to support the sample. Figure 4.3b displays the transmission electron micrograph of fresh Ru/ZrO_2. The zirconia support was found to have well defined crystal planes. However, it was not possible to obtain a well resolved image of ruthenium particles due to the poor contrast between ruthenium and zirconium.

(a)

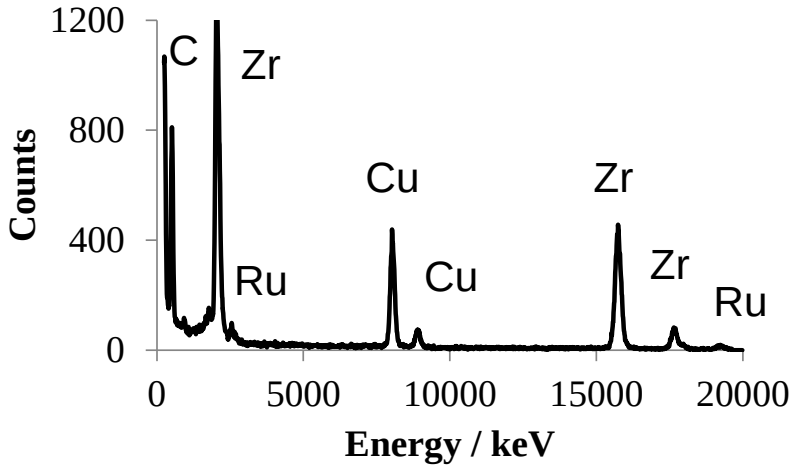
1200
800
400
0
Counts
C
Zr
Ru
Cu
Cu
Zr
Zr
Ru
0
5000
10000
15000
20000
Energy / keV

(b)

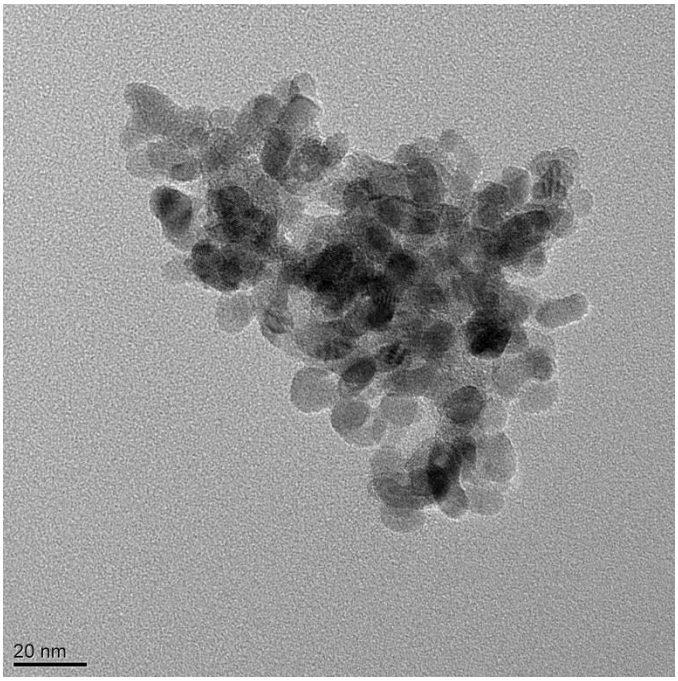
20 nm

Figure 4.3 (a) EDX spectrum and (b) transmission electron micrograph of fresh Ru/ZrO_2.

(a)

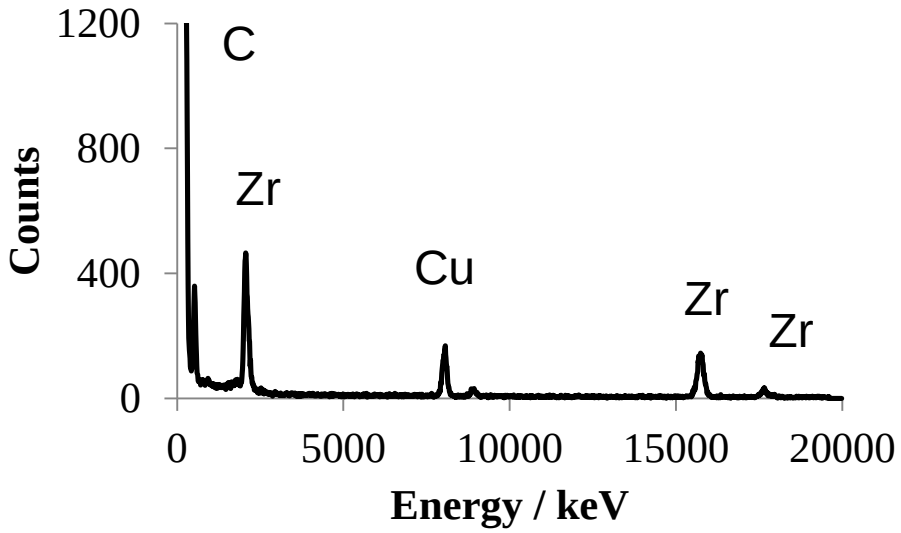

(b)

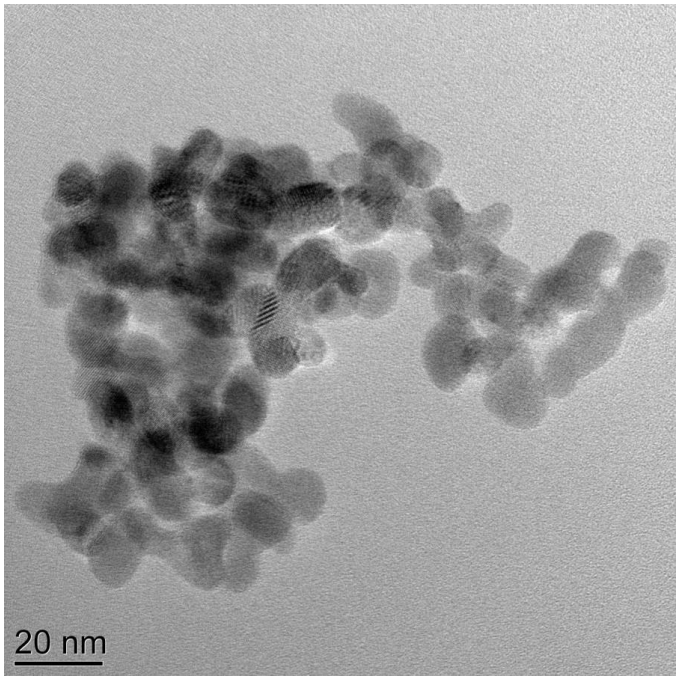

Figure 4.4 (a) EDX spectrum and (b) transmission electron micrograph of Ru/ZrO_2-pH3.

The transmission electron micrographs of Ru/ZrO_2 after treatment at pH 3 and 225 °C for 72 hours appeared no different from the transmission electron micrographs for fresh Ru/ZrO_2 (Figure 4.4). The zirconia particles appear uniform and approximately the same size for both pH 3 and the fresh sample (Figure 4.3b and Figure 4.4b). The major difference was found with the ruthenium particles. From EDX, it was impossible to detect ruthenium present on the surface of any of the samples supported on the grid (Figure 4.4a). It was determined from Figure 4.3a that ruthenium was present on the surface of the fresh sample. ICP analysis of a sample of the hydrothermal treatment at pH 3 filtrate shows that less than 1% of the ruthenium present on the surface was leached into the acidic solution. Therefore, the ruthenium present on the surface of Ru/ZrO_2-pH 3 must be too small to be resolved by TEM. This indicates an increase in dispersion of ruthenium during the hydrothermal treatment. As the dispersion increases, the particle size of ruthenium must decrease, making energy peak separation in EDX and identification difficult.

4.3.2 Glycerol hydrogenolysis

Glycerol hydrogenolysis is used as a test reaction to determine the effects of treatments in hot liquid water at acid and basic pH on the conversion and the selective cleavage of C-C and C-O bonds in hydrodeoxygenation of polyols [155]. Commonly studied supported metals are Ru, Rh, Pt and Pd due to their high activity [13, 144, 156-159]. The main products of glycerol hydrogenolysis over supported ruthenium catalysts are propanediols, ethylene glycol and methane [25]. The product distribution and overall conversion are highly dependent on the surface morphology and chemical properties as

well as the particle size, although the trends found in literature are inconsistent [13]. A simplified reaction scheme is proposed below (Figure 4.5).

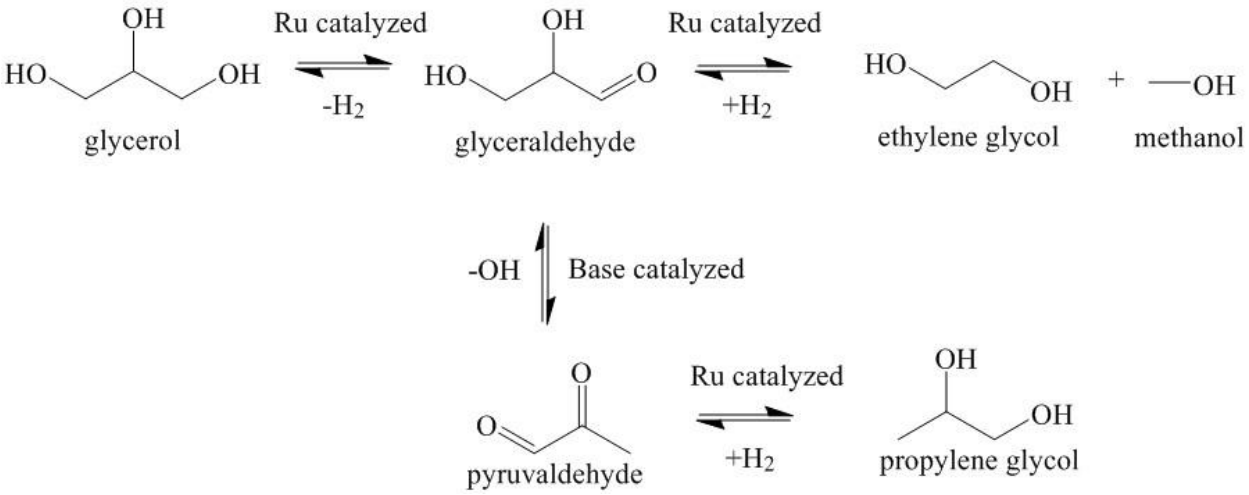

Figure 4.5 Simplified reaction pathway of glycerol hydrogenolysis to ethylene glycol and propanediols adapted from Maris and Davis [13].

First, glycerol undergoes a metal catalyzed dehydration reaction to produce glyceraldehyde as an intermediate. Next, ruthenium can cleave a C-C bond to produce ethylene glycol and methanol. Methanol can then degrade into methane. Alternatively, glyceraldehyde can undergo a base catalyzed dehydration and then subsequently hydrogenate to produce propylene glycol.

Table 4.2 Yield and selectivity at 200 °C and similar conversion for all samples.

Sample	Conversion / %	Time / Minutes	Y_{eg}	Y_{pg}	S_{eg}	S_{pg}	S_{pg}/S_{eg}	Carbon Balance
Ru/ZrO_2	16	45	1.0	1.1	6	7	1.1	86
Ru/ZrO_2-ph 3	9	45	0.8	1.7	9	18	2.1	93
Ru/ZrO_2-ph 5	12	165	0.7	1.2	6	10	1.7	90
Ru/ZrO_2-ph 7	12	45	0.4	0.8	3	6	2.0	89
Ru/ZrO_2-ph 9	13	75	0.7	1.4	5	11	2.1	89
Ru/ZrO_2-ph 11	15	165	0.5	0.8	4	6	1.6	86

Glycerol hydrogenolysis was used as a test reaction to investigate the influence of hydrothermal treatment at acidic and basic pH on the selectivity and yield of two valuable products, ethylene glycol and propylene glycol at similar conversions (Table 4.2). The carbon balance was closed to at least 86% (Ru/ZrO_2 and Ru/ZrO_2-pH11). The carbon in the batch reaction is mostly accounted for by unreacted glycerol. In fact, only 1-2% of the carbon balance was accounted for with propylene or ethylene glycol. Analysis of the liquid phase, showed that the only compounds present were ethylene glycol, propylene glycol, glycerol and water. This indicates that a majority of the products formed from glycerol hydrogenolysis were gaseous products. Common gaseous products formed in glycerol hydrogenolysis are methane, CO and CO_2 [25]. The primary gaseous product formed is methane. Methane is formed from the cleavage of a C-C bond in glycerol or ethylene glycol [24, 145]. CO and CO_2 are degradation products that can also be hydrogenated to form methane. The temperature of the reaction was 200 °C, which was high enough to favor deep hydrogenolysis reactions to form large amounts of methane [25]. The exact mechanism and the quantity of gaseous products formed are outside the scope of this work. Since the purpose of this work is to assess the hydrothermal stability of Ru/ZrO_2 in different pH environments, the focus of the glycerol hydrogenolysis test reaction is on the yield and selectivity of the most desired products relative to each other.

Fresh Ru/ZrO_2 yielded approximately equal amounts of ethylene and propylene glycol. After Ru/ZrO_2 was subjected to hydrothermal treatment at 225 °C for 72 hours, the yield of ethylene glycol decreased regardless of the pH. Generally, as the pH during the hydrothermal treatment deviated from neutral pH, the yield of ethylene glycol increased. The only deviation from this trend is the yield of ethylene glycol at pH 11. These trends loosely follow the total Lewis acid site concentrations found in Table 4.1. As the number of Lewis acid sites increased, the yield of ethylene glycol increased (Figure 4.6).

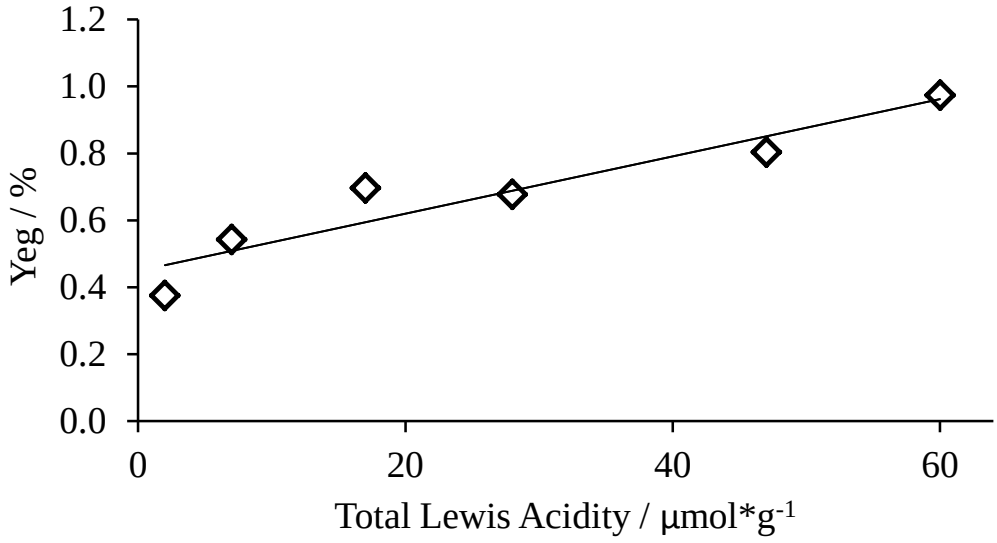

Figure 4.6. Relationship of yield of ethylene glycol and total Lewis acidity.

With the exception of Ru/ZrO_2-pH 7 and Ru/ZrO_2-pH 11, the yield of propylene glycol increased after hydrothermal treatment. The decreased yield of propylene glycol over Ru/ZrO_2-pH11 can be explained by the blockage or transformation of active sites by water in alkaline conditions. Literature shows that treating Ru/ZrO_2 in alkaline conditions can introduce more hydroxyl groups on the surface as compared to a fresh sample [151]. Furthermore, a water layer is found to be present on Ru/ZrO_2 at basic pHs that can block active sites [151]. I speculate that water blocks at least some of the active sites for C-O

bond cleavage in the hydrothermal treatment at pH 11. However, I believe that the effect of Lewis acidity on the reaction pathway is more complex.

Fresh Ru/ZrO_2 had selectivities toward ethylene glycol and propylene glycol of 6% and 7%, respectively. This indicates that before Ru/ZrO_2 underwent hydrothermal treatment, the glycerol hydrogenolysis reaction was relatively indiscriminate. After hydrothermal treatment, the selectivities changed, although no clear trend emerged with regard to the pH of the aqueous medium. In order to compare the rate of C-C and C-O bond cleavage, the ratio of the selectivity of propylene glycol to ethylene glycol was compared. While this comparison is often performed in glycerol hydrogenolysis literature, in order to be completely accurate, the carbon consumed from cleavage of the C-C bond in glycerol, should be included in the ratio of selectivities with ethylene glycol. Since this data is not available, it is excluded with the caveat that the trend shown in Figure 4.7 is not entirely accurate. Only a general positive or negative trend can be extrapolated. Figure 4.7 shows the effect of ruthenium dispersion on the ratio of the selectivity of ethylene glycol to propylene glycol.

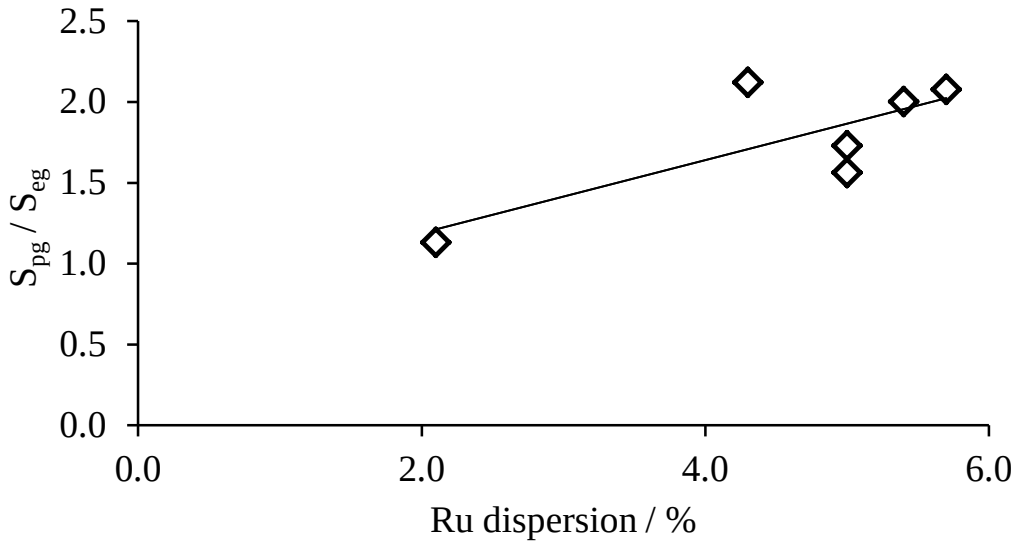

Figure 4.7. The effect of ruthenium dispersion on the ratio of propylene glycol to ethylene glycol selectivities.

When compared at similar conversion, an increase in ruthenium dispersion increased the selectivity ratio of propylene glycol to ethylene glycol. A larger Ru particle size will correspond to a lower dispersion. Larger Ru particles are known to promote cleavage of a C-C bond of glycerol to produce ethylene glycol. [25]. Thus, the general positive trend depicted in Figure 4.7. From this data, I can speculate that the decrease in the Ru particle size increases surface interactions between glycerol and vacancy sites that promote C-O bond cleavage over C-C bond cleavage. These results have large implications on industrial applications of Ru/ZrO_2 for glycerol hydrogenolysis. Hydrothermal treatments in acidic and basic pH affect the dispersion of Ru on zirconia. This indicates that metal particles must be mobile in some way. The mobility of the metal particles causes the observed changes in selectivity. The mobility of a metal on a surface is undesirable because the metal could potentially be washed off the surface of the catalyst in flow conditions causing a loss of catalytic activity.

4.4 Conclusions

Hydrothermal treatment under acidic and basic conditions had an impact on the surface characteristics of Ru/ZrO_2. Most importantly, the dispersion of ruthenium and the Lewis acidity of the surface greatly changed without major alterations to the surface area, pore volume, pore size or crystal structure. An increase in Ru dispersion showed an increase in the selectivity to propylene glycol relative to ethylene glycol. A decrease in total Lewis acid site concentration was correlated with a decrease in the ethylene glycol yield. These findings have important implications on application in industry. As this research shows, there are great differences between selectivity and yield upon exposure

to hot liquid water at different pH. This indicates that stability of catalysts in realistic industrial environments is crucial to the selection of the best catalyst for a reaction.

APPENDIX A

SUPPLEMENTARY INFORMATION FOR CHAPTER 2

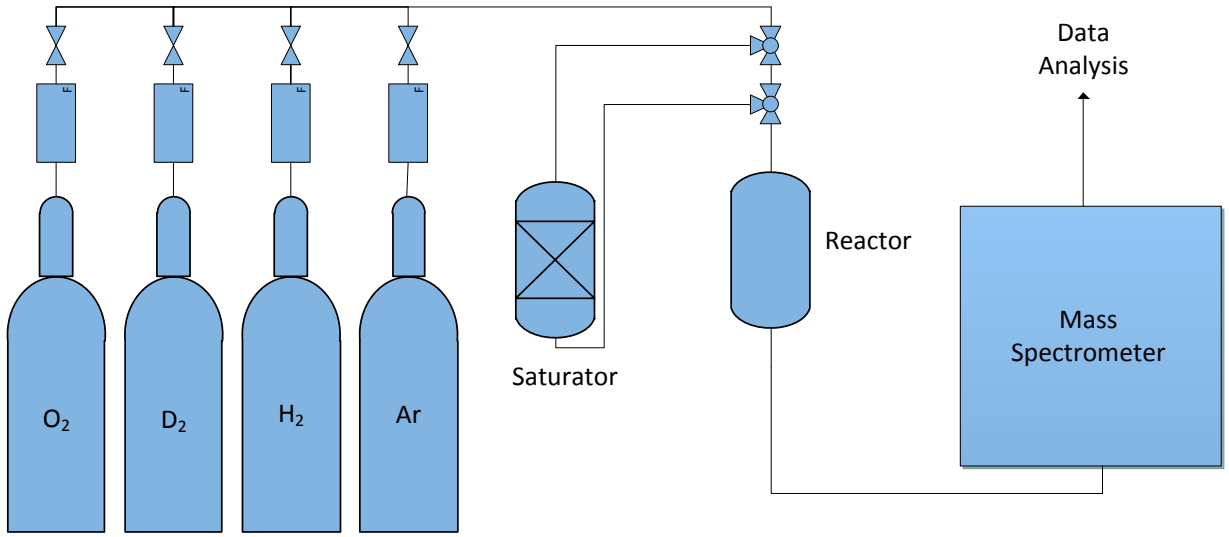

Figure A.1 Custom Built Flow Reactor for H_2-D_2 exchange reaction.

A 0.25 inch quartz tube serves as the reactor. Mass flow controllers (Brooks SLA5850s for hydrogen and deuterium and Brooks 4800 for argon) supply gas flows to a 4 way valve with the option to flow directly to the reactor or bypass the reactor. The purpose of

the bypass is to gain experimental data for the inlet stream with no catalyst present and no reaction occurring. The composition of the gas stream was analyzed downstream by a Stanford Research Systems QMS300 gas analyzer. The mass flow controllers, a pressure transducer and the mass spectrometer were controlled by a custom made Labview program. The temperature of the reactor was controlled using a Lindberg Blue M Minimite Tube Furnace. An additional thermocouple was used to monitor and record the temperature of the sample as the exchange reaction proceeded.

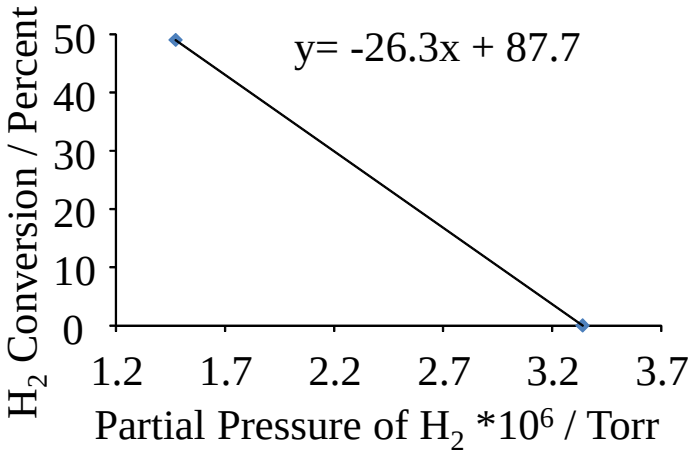

Figure A.2 Mass spectrometer equilibrium calibration.

Calibration is performed using hydrogen for all catalysts. A background "blank" reading is recorded for 30 minutes at room temperature with no catalyst present. An equilibrium composition is recorded at 700 °C for 30 minutes. The equilibrium conversion is calculated using the equilibrium constant equation [62].

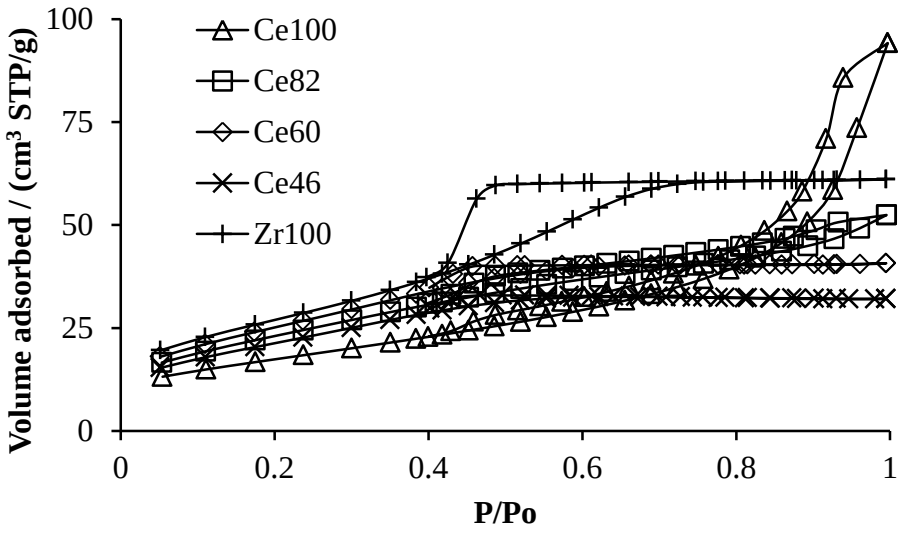

Figure A.3 Nitrogen adsorption isotherms at 77 K for ceria-zirconia mixed metal oxides.

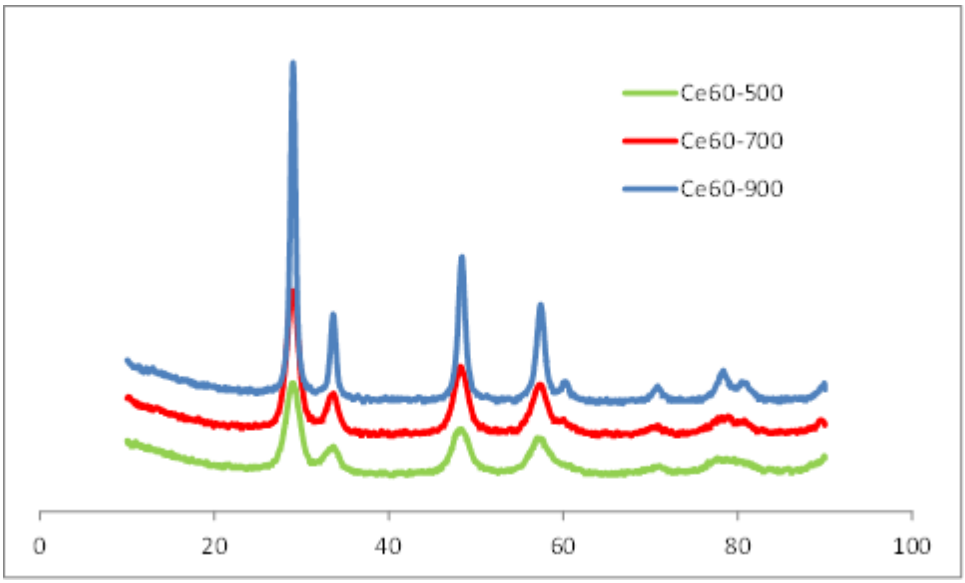

Figure A.4 X-ray diffractogram of Ce60 calcined at 500, 700 and 900 °C.

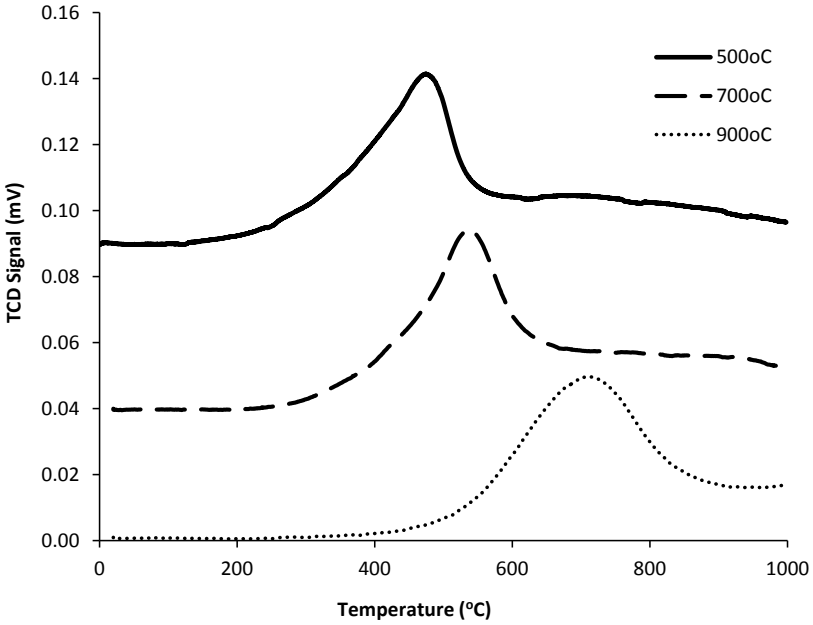

Figure A.5 Temperature-programmed reduction of Ce60 at 500, 700 and 900 °C.

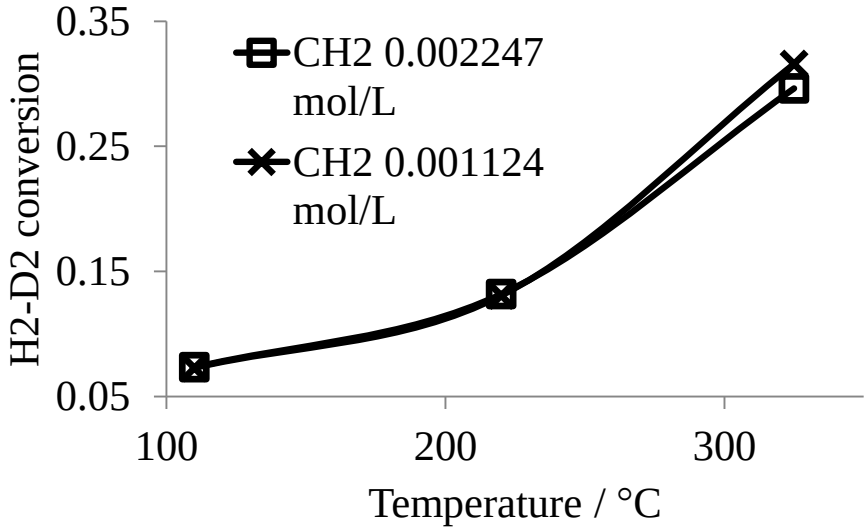

Figure A.6 External mass transport limitations of Ce60 at 110, 220 and 325 °C at constant space velocity. Transport limitations were tested by keeping space velocity and catalyst mass constant. The inlet concentration of hydrogen and hydrogen flow rate were varied.

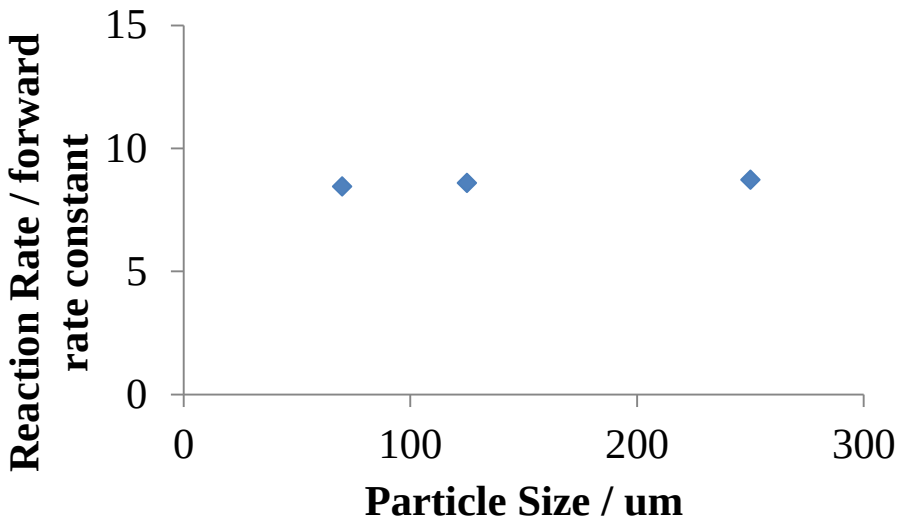

Figure A.7 Intraparticle mass transport for Ce60 catalysts at 300 °C.

Reaction rate is calculated as : $r = k_1([H_2] - \frac{[HD]}{K_{eq}})$

The difference between the reaction rate at the smallest and largest particle size is 3.1% which is within the range of error of the mass spectrometer.

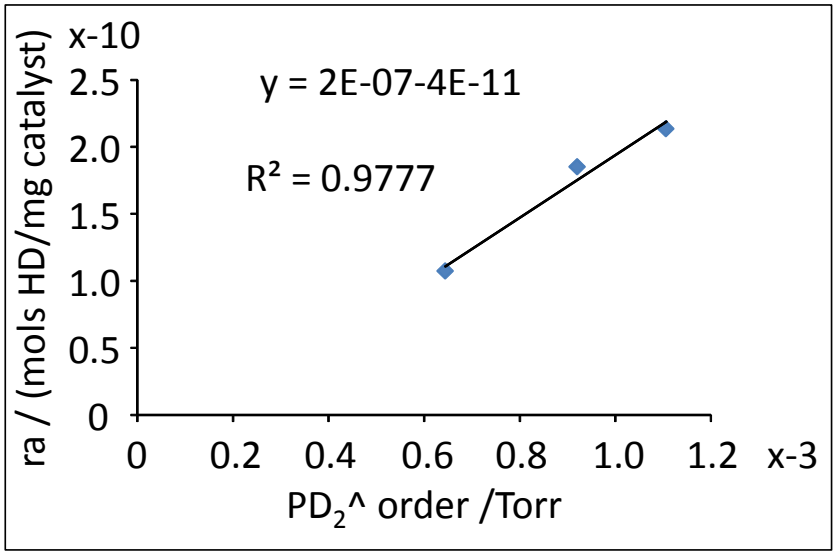

Figure A.8 Find reaction order for deuterium.

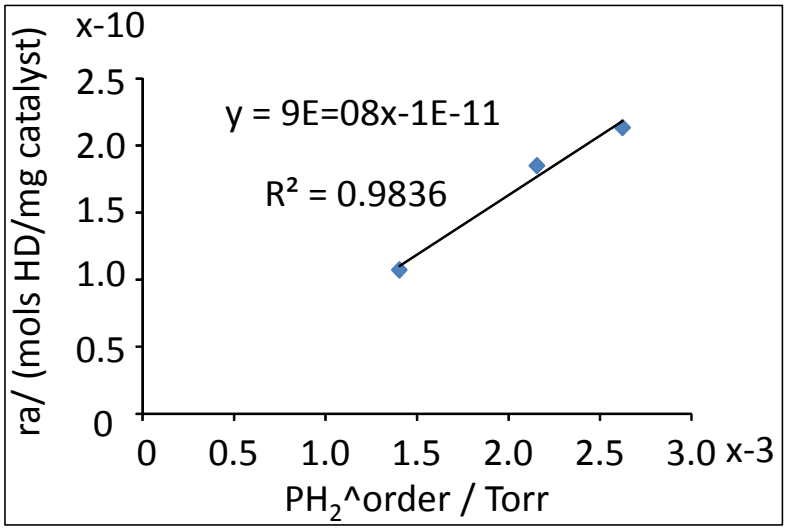

Figure A.9 Find reaction order for hydrogen.

Procedure for finding reaction order:

For Ce82, at 110 °C, conversion ~0.05, so we can assume differential reactor conditions.

Ra=molar outflow of HD/catalyst weight

Plot Ra vs inlet pressures of hydrogen and deuterium raised to an order, N

When a straight line is achieved, N is the order

If N = 0.5: Since R^2 value is high for deuterium and hydrogen at N= 0.5, the order w.r.t each gas is 0.5 with an overall reaction order of 1.

Table A.1 Comparison of steady-State conversion with ramp conversion for Ce60.

Temperature / ° C	Steady- State Conversion / %	Ramp Conversion / %
110	7	5
220	13	14
325	30	29

The purpose of this experiment was to ensure that the kinetic data extracted from ramped data was at steady state. The reaction at steady state was recorded for 1 hour and the conversion was averaged. Since the conversion at steady state and the conversion from the ramped data are close in the temperature range of interest, it was assumed that a ramp rate of 2 K/min was sufficient.

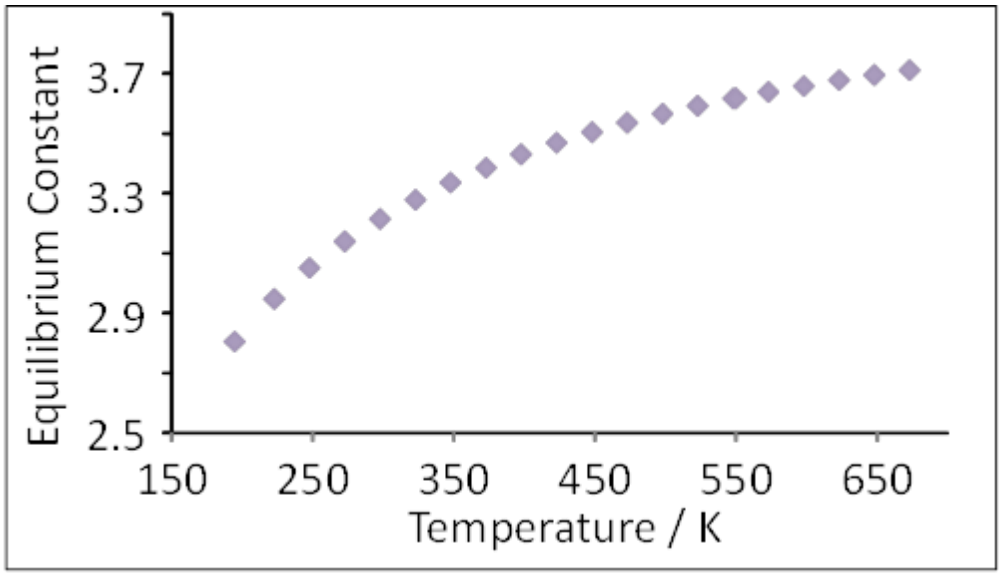

Figure A.10 Equilibrium constant for H_2-D_2 exchange reaction as it varies with temeperature.

(a)

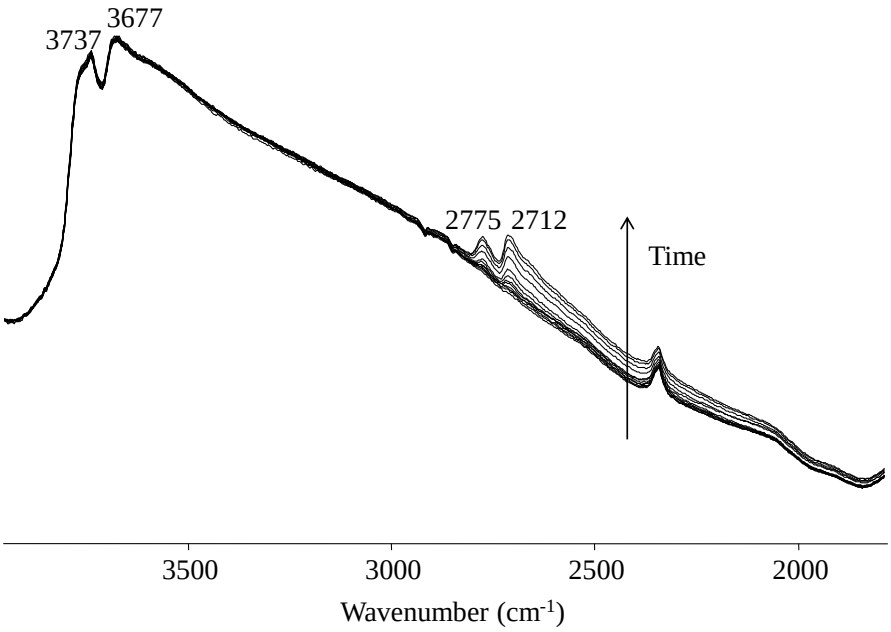

(b)

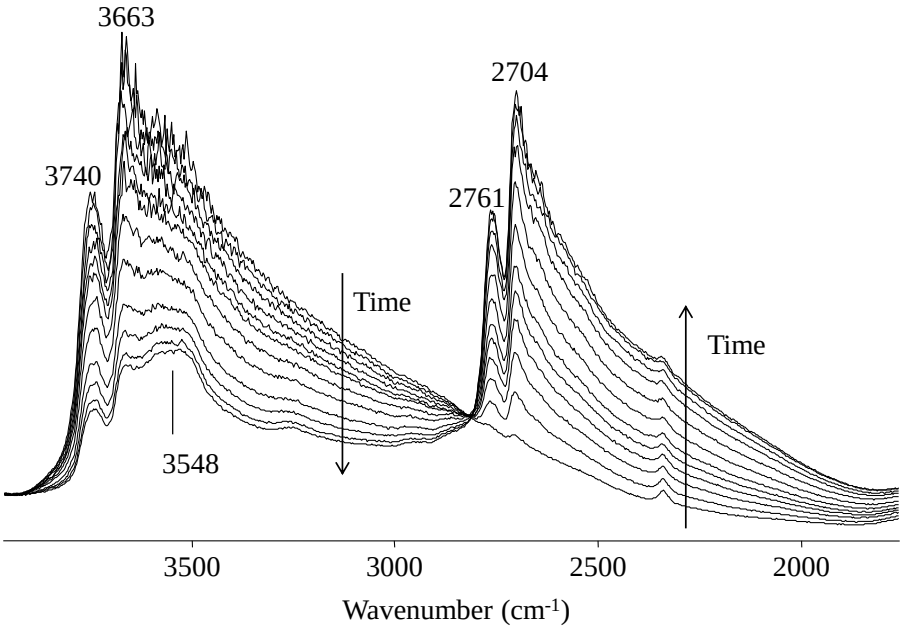

Figure A.11 FTIR spectra of isotopic hydrogen exchange for zirconia at (a) 150 °C and (b) 350 °C.

REFERENCES

[1] M.M. Rahman, S.B. Mostafiz, J.V. Paatero, R. Lahdelma, Renew. Sust. Energ. Rev. 29 (2014) 108.

[2] D. Mohan, C.U. Pittman, P.H. Steele, Energ. Fuel 20 (2006) 848.

[3] B. van Ruijven, D.P. van Vuuren, Energ. Policy 37 (2009) 4797.

[4] A. Demirbas, Prog. Energy Combust. Sci. 33 (2007) 1.

[5] M. Stocker, Angewandte Chemie-International Edition 47 (2008) 9200.

[6] V.A. Yakovlev, S.A. Khromova, O.V. Sherstyuk, V.O. Dundich, D.Y. Ermakov, V.M. Novopashina, M.Y. Lebedev, O. Bulavchenko, V.N. Parmon, Catal. Today 144 (2009) 362.

[7] H. Pacini, S. Silveira, A.C. da Silva Filho, European Energy Journal 3 (2013) 1.

[8] A.J. Ragauskas, C.K. Williams, B.H. Davison, G. Britovsek, J. Cairney, C.A. Eckert, W.J. Frederick, J.P. Hallett, D.J. Leak, C.L. Liotta, J.R. Mielenz, R. Murphy, R. Templer, T. Tschaplinski, Science 311 (2006) 484.

[9] C. Briens, J. Piskorz, F. Berruti, Int. J. Chem. React. Eng. 6 (2008).

[10] F.S. de Oliveira, L.S.G. Teixeira, M.C.U. Araujo, M. Korn, Fuel 83 (2004) 917.

[11] T. Issariyakul, A.K. Dalai, Can. J. Chem. Eng. 90 (2012) 342.

[12] L. Reijnders, M.A.J. Huijbergts, Biofuels for Road Transport: A Seed to Wheel Perspective, Springer, 2009.

[13] E.P. Maris, R.J. Davis, J. Catal. 249 (2007) 328.

[14] C.H. Zhou, H. Zhao, D.S. Tong, L.M. Wu, W.H. Yu, Catalysis Reviews-Science and Engineering 55 (2013) 369.

[15] L. Ma, D.H. He, Chinese Journal of Catalysis 30 (2009) 471.

[16] P.M. Mortensen, J.D. Grunwaldt, P.A. Jensen, K.G. Knudsen, A.D. Jensen, Appl. Catal. A 407 (2011) 1.

[17] T.R. Carlson, G.A. Tompsett, W.C. Conner, G.W. Huber, Top. Catal. 52 (2009) 241.

[18] A.V. Bridgwater, G.V.C. Peacocke, Renew. Sust. Energ. Rev. 4 (2000) 1.

[19] R.H. Venderbosch, W. Prins, Biofuel Bioprod. Bior. 4 (2010) 178.

[20] G.W. Huber, S. Iborra, A. Corma, Chem. Rev. 106 (2006) 4044.

[21] V.N. Bui, D. Laurenti, P. Afanasiev, C. Geantet, Appl. Catal. B 101 (2011) 239.

[22] E. Furimsky, Appl. Catal. A 199 (2000) 147.

[23] D.C. Elliott, Energ. Fuel 21 (2007) 1792.

[24] T. Miyazawa, S. Koso, K. Kunimori, K. Tomishige, Appl. Catal. A 329 (2007) 30.

[25] S. Wang, K. Yin, Y. Zhang, H. Liu, ACS Catalysis 3 (2013) 2112.

[26] S.H. Zhu, Y.N. Qiu, Y.L. Zhu, S.L. Hao, H.Y. Zheng, Y.W. Li, Catal. Today 212 (2013) 120.

[27] A. Jones, Temperature-Programmed Reduction for Solid Materials Characterization, Marcel Dekker, Inc., New York, New York, 1986.

[28] Isotope Effects in Gas-Phase Chemistry, in: J.A. Kaye (Ed.), Americal Chemical Society, 1992.

[29] C.N.R.R.a.B. Raveau, Transition Metal Oxides, VCH Publishers, Inc., New York, New York, 1995.

[30] L.E. Briand, Investigation of the Nature and Number of Surface Active Sites of Supported and Bulk Metal Oxide Catalysts through Methanol Chemisorption, in: J.L.G. Fierro (Ed.) Metal Oxides: Chemistry and Applications, CRC Press, Boca Ration, FL, 2006.

[31] L. Vivier, D. Duprez, ChemSusChem 3 (2010) 654.

[32] A. Trovarelli, C. de Leitenburg, M. Boaro, G. Dolcetti, Catal. Today 50 (1999) 353.

[33] N. Ichikawa, S. Sato, R. Takahashi, T. Sodesawa, H. Fujita, T. Atoguchi, A. Shiga, J. Catal. 239 (2006) 13.

[34] K.M. Dooley, A.K. Bhat, C.P. Plaisance, A.D. Roy, Appl. Catal. A 320 (2007) 122.

[35] J. Kaspar, P. Fornasiero, M. Graziani, Catal. Today 50 (1999) 285.

[36] A. Trovarelli, Cat. Rev. - Sci. Eng. 38 (1996) 439.

[37] Q.A. Yu, X.X. Wu, C.J. Tang, L. Qi, B. Liu, F. Gao, K.Q. Sun, L. Dong, Y. Chen, J. Colloid Interface Sci. 354 (2011) 341.

[38] S.M. Sager, D.I. Kondarides, X.E. Verykios, Appl. Catal. B 103 (2011) 275.

[39] P. Gelin, M. Primet, Appl. Catal. B 39 (2002) 1.

[40] V.V. Kharton, F.M.B. Marques, A. Atkinson, Solid State Ionics 174 (2004) 135.

[41] S. McIntosh, R.J. Gorte, Chem. Rev. 104 (2004) 4845.

[42] R.M. Ormerod, Chem. Soc. Rev. 32 (2003) 17.

[43] J.W. Fergus, J. Power Sources 162 (2006) 30.

[44] F. Giordano, A. Trovarelli, C. de Leitenburg, M. Giona, J. Catal. 193 (2000) 273.

[45] W.C. Conner, J.L. Falconer, Chem. Rev. 95 (1995) 759.

[46] D. Martin, D. Duprez, J. Phys. Chem. 100 (1996) 9429.

[47] Catalysis by Ceria and Related Materials, Imperial College Press, London, 2002.

[48] B.B. Gianvito Vile, Jonas Wichert, and Javier Perez-Ramirez, Angew. Chem. 51 (2012).

[49] E. Aneggi, M. Boaro, C. de Leitenburg, G. Dolcetti, A. Trovarelli, J. Alloys Compd. 408 (2006) 1096.

[50] D.R. Moberg, T.J. Thibodeau, F.G. Amar, B.G. Frederick, J. Phys. Chem. C 114 (2010) 13782.

[51] T. Prasomsri, T. Nimmanwudipong, Y. Roman-Leshkov, Energy Environ. Sci. 6 (2013) 1732.

[52] P. Fornasiero, G. Balducci, R. DiMonte, J. Kaspar, V. Sergo, G. Gubitosa, A. Ferrero, M. Graziani, J. Catal. 164 (1996) 173.

[53] F. Fally, V. Perrichon, H. Vidal, J. Kaspar, G. Blanco, J.M. Pintado, S. Bernal, G. Colon, M. Daturi, J.C. Lavalley, Catal. Today 59 (2000) 373.

[54] W.G. Reimers, M.A. Baltanas, M.M. Branda, Appl. Surf. Sci. 274 (2013) 1.

[55] M.V. Ganduglia-Pirovano, A. Hofmann, J. Sauer, Surf. Sci. Rep. 62 (2007) 219.

[56] S. Rossignol, Y. Madier, D. Duprez, Catal. Today 50 (1999) 261.

[57] A.K. Cheetham, A.P. Wilkinson, Angew. Chem. Int. Ed. Engl. 31 (1992) 1557.

[58] B.D. Cullity, Elements of X-Ray Diffraction, Addison-Wesley Pub. Co., 1956.

[59] A.E. Nelson, K.H. Schulz, Appl. Surf. Sci. 210 (2003) 206.

[60] S. Brunauer, P.H. Emmett, E. Teller, J. Am. Chem. Soc. 60 (1938) 309.

[61] E.P. Barrett, L.G. Joyner, P.P. Halenda, J. Am. Chem. Soc. 73 (1951) 373.

[62] D.A. McQuarrie, Statistical Mechanics, University Science Books, 2000.

[63] L.S. Birks, E.J. Brooks, Anal. Chem. 22 (1950) 1017.

[64] D.E. K. Sing, R. Haul, L. Moscou, R. Pierotti, J. Rouquerol, T. Siemieniewska., Pure Appl. Chem. 57 (1985) 603.

[65] C.G.V. Burgess, D.H. Everett, J. Colloid Interface Sci. 33 (1970) 611.

[66] S. Rossignol, F. Gerard, D. Duprez, J. Mater. Chem. 9 (1999) 1615.

[67] P. Fornasiero, T. Montini, M. Graziani, J. Kaspar, A.B. Hungria, A. Martinez-Arias, J.C. Conesa, Phys. Chem. Chem. Phys. 4 (2002) 149.

[68] V.S. Escribano, E.F. Lopez, M. Panizza, C. Resini, J.M.G. Amores, G. Busca, Solid State Sci. 5 (2003) 1369.

[69] B. Akhlaghinia, H. Ebrahimabadi, E.K. Goharshadi, S. Samiee, S. Rezazadeh, J. Mol. Catal. A-Chem. 357 (2012) 67.

[70] R. Srinivasan, R.J. De Angelis, G. Ice, B.H. Davis, J. Mater. Res. 6 (1991) 1287.

[71] R. Srinivasan, S.F. Simpson, J.M. Harris, B.H. Davis, J. Mater. Sci. Lett. 10 (1991) 352.

[72] S.M. Sun, X.L. Zhao, H. Lu, Z.D. Zhang, J.J. Wei, Y.Z. Yang, CrystEngComm 15 (2013) 1370.

[73] B. Choudhury, P. Chetri, A. Choudhury, Rsc. Advances 4 (2014) 4663.

[74] S. Bernal, J.J. Calvino, G.A. Cifredo, J.M. Gatica, J.A.P. Omil, J.M. Pintado, J. Chem. Soc. Faraday Trans. 89 (1993) 3499.

[75] D.E. Mears, Industrial & Engineering Chemistry Process Design and Development 10 (1971) 541.

[76] R.P. Chambers, M. Boudart, J. Catal. 6 (1966) 141.

[77] D. Martin, D. Duprez, J. Phys. Chem. B 101 (1997) 4428.

[78] L. Masgrau, A. Gonzalez-Lafont, J.M. Lluch, Theor. Chem. Acc. 110 (2003) 352.

[79] A. Badri, C. Binet, J.C. Lavalley, J. Chem. Soc. Faraday Trans. 92 (1996) 4669.

[80] F.C. Gennari, T. Montini, N. Hickey, P. Fornasiero, A. Graziani, Appl. Surf. Sci. 252 (2006) 8456.

[81] M. Daturi, C. Binet, J.C. Lavalley, A. Galtayries, R. Sporken, Phys. Chem. Chem. Phys. 1 (1999) 5717.

[82] B. Azambre, I. Atribak, A.n. Bueno-López, A. García-García, J. Phys. Chem. C. 114 (2010) 13300.

[83] M. Daturi, E. Finocchio, C. Binet, J.C. Lavalley, F. Fally, V. Perrichon, J. Phys. Chem. B 103 (1999) 4884.

[84] S.E. Collins, J.M. Cíes, E. del Río, M. López-Haro, S. Trasobares, J.J. Calvino, J.M. Pintado, S. Bernal, J. Phys. Chem. C. 111 (2007) 14371.

[85] C. Binet, A. Badri, J.C. Lavalley, J. Phys. Chem. 98 (1994) 6392.

[86] C. Morterra, G. Cerrato, L. Ferroni, L. Montanaro, Mater. Chem. Phys. 37 (1994) 243.

[87] K.H. Kim, J.R. Kim, S.K. Ihm, J. Hazard. Mater. 167 (2009) 1158.

[88] C.C. Chuang, H.I. Hsiang, J.S. Hwang, T.S. Wang, J. Alloys Compd. 470 (2009) 387.

[89] C. Binet, M. Daturi, J.C. Lavalley, Catal. Today 50 (1999) 207.

[90] J.H. Hwang, T.O. Mason, Zeitschrift Fur Physikalische Chemie-International Journal of Research in Physical Chemistry & Chemical Physics 207 (1998) 21.

[91] A. Trovarelli, Catalysis Reviews-Science and Engineering 38 (1996) 439.

[92] E. Iglesia, D.G. Barton, J.A. Biscardi, M.J.L. Gines, S.L. Soled, Catal. Today 38 (1997) 339.

[93] G. Vile, B. Bridier, J. Wichert, J. Perez-Ramirez, Angewandte Chemie-International Edition 51 (2012) 8620.

[94] D. Martin, D. Duprez, Stud. Surf. Sci. Catal. 77 (1993) 201.

[95] U.M. Bhatta, D. Reid, T. Sakthivel, T.X.T. Sayle, D. Sayle, M. Molinari, S.C. Parker, I.M. Ross, S. Seal, G. Mobus, J. Phys. Chem. C 117 (2013) 24561.

[96] M. Benkhaled, C. Descorme, D. Duprez, S. Morin, C. Thomazeau, D. Uzio, Appl. Catal. A 346 (2008) 36.

[97] D. Duprez, Catal. Today 112 (2006) 17.

[98] C. Zhao, J. He, A.A. Lemonidou, X. Li, J.A. Lercher, J. Catal. 280 (2011) 8.

[99] P. McKendry, Bioresour. Technol. 83 (2002) 37.

[100] N.B. Van, D. Laurenti, P. Delichere, C. Geantet, Appl. Catal. B 101 (2011) 246.

[101] C.S. Song, Catal. Today 86 (2003) 211.

[102] J.D. Holladay, J. Hu, D.L. King, Y. Wang, Catal. Today 139 (2009) 244.

[103] X.L. Ma, K.Y. Sakanishi, I. Mochida, Ind. Eng. Chem. Res. 33 (1994) 218.

[104] P.R. Wentrcek, H. Wise, J. Catal. 51 (1978) 80.

[105] A.L. Jongerius, R. Jastrzebski, P.C.A. Bruijnincx, B.M. Weckhuysen, J. Catal. 285 (2012) 315.

[106] E. Laurent, B. Delmon, J. Catal. 146 (1994) 281.

[107] A.Y. Bunch, X.Q. Wang, U.S. Ozkan, J. Mol. Catal. A-Chem. 270 (2007) 264.

[108] F.E. Massoth, P. Politzer, M.C. Concha, J.S. Murray, J. Jakowski, J. Simons, J. Phys. Chem. B 110 (2006) 14283.

[109] E.M. Ryymin, M.L. Honkela, T.R. Viljava, A.O.I. Krause, Appl. Catal. A 389 (2010) 114.

[110] P.M. Mortensen, J.D. Grunwaldt, P.A. Jensen, A.D. Jensen, Acs Catalysis 3 (2013) 1774.

[111] O.I. Senol, T.R. Viljava, A.O.I. Krause, Appl. Catal. A 326 (2007) 236.

[112] L.F. Liotta, A. Macaluso, A. Longo, G. Pantaleo, A. Martorana, G. Deganello, Appl. Catal. A 240 (2003) 295.

[113] S. Bernal, Chemical Reactivity of Binary Rare Earth Oxides, in: G. Adachi (Ed.) Binary Rare Earth Oxides, Kluwer Academic Publishers, 2004.

[114] E.S. Putna, T. Bunluesin, X.L. Fan, R.J. Gorte, J.M. Vohs, R.E. Lakis, T. Egami, Catal. Today 50 (1999) 343.

[115] D.E. Resasco, J. Phys. Chem. Lett. 2 (2011) 2294.

[116] N. Yi, R. Si, H. Saltsburg, M. Flytzani-Stephanopoulos, Appl. Catal. B 95 (2010) 87.

[117] M.A. Gonzalez-Borja, D.E. Resasco, Energ. Fuel 25 (2011) 4155.

[118] W. Zhang, J.Z. Chen, R.L. Liu, S.P. Wang, L.M. Chen, K.G. Li, Acs Sustainable Chemistry & Engineering 2 (2014) 683.

[119] E. Furimsky, F.E. Massoth, Catal. Today 52 (1999) 381.

[120] H.Y. Zhao, D. Li, P. Bui, S.T. Oyama, Appl. Catal. A 391 (2011) 305.

[121] Y.-C. Lin, C.-L. Li, H.-P. Wan, H.-T. Lee, C.-F. Liu, Energ. Fuel 25 (2011) 890.

[122] A. Gutierrez, R.K. Kaila, M.L. Honkela, R. Slioor, A.O.I. Krause, Catal. Today 147 (2009) 239.

[123] I.T. Ghampson, C. Sepulveda, R. Garcia, B.G. Frederick, M.C. Wheeler, N. Escalona, W.J. DeSisto, Appl. Catal. A 413 (2012) 78.

[124] T. Nimmanwudipong, C. Aydin, J. Lu, R.C. Runnebaum, K.C. Brodwater, N.D. Browning, D.E. Block, B.C. Gates, Catal. Lett. 142 (2012) 1190.

[125] R.N. Olcese, M. Bettahar, D. Petitjean, B. Malaman, F. Giovanella, A. Dufour, Appl. Catal. B 115 (2012) 63.

[126] G. de la Puente, A. Gil, J.J. Pis, P. Grange, Langmuir 15 (1999) 5800.

[127] J. Horacek, G. St'avova, V. Kelbichova, D. Kubicka, Catal. Today 204 (2013) 38.

[128] V.N. Bui, D. Laurenti, P. Delichere, C. Geantet, Appl. Catal. B 101 (2011) 246.

[129] M. Saidi, F. Samimi, D. Karimipourfard, T. Nimmanwudipong, B.C. Gates, M.R. Rahimpour, Energy Environ. Sci. 7 (2014) 103.

[130] J. Filley, C. Roth, J. Mol. Catal. A-Chem. 139 (1999) 245.

[131] R.K. Sharma, N.N. Bakhshi, Can. J. Chem. Eng. 69 (1991) 1071.

[132] R. Wandas, J. Surygala, E. Sliwka, Fuel 75 (1996) 687.

[133] S. Sato, K. Koizumi, F. Nozaki, Appl. Catal. A 133 (1995) L7.

[134] J.J. Delgado, X. Chen, J.A. Pérez-Omil, J.M. Rodríguez-Izquierdo, M.A. Cauqui, Catal. Today 180 (2012) 25.

[135] S. Keav, A. Martin, J. Barbier-Jr, D. Duprez, Comptes Rendus Chimie 13 (2010) 508.

[136] C. Liu, A. Karim, V. Lebarbier, D. Mei, Y. Wang, Top. Catal. 56 (2013) 1782.

[137] J.R.M. Almeida, L.C.L. Favaro, B.F. Quirino, Biotechnology for Biofuels 5 (2012).

[138] D. Duran-Martin, M. Ojeda, M.L. Granados, J.L.G. Fierro, R. Mariscal, Catal. Today 210 (2013) 98.

[139] D.M. Alonso, J.Q. Bond, J.A. Dumesic, Green Chemistry 12 (2010) 1493.

[140] Q.G. Xie, W. Taweepreda, C. Musikavong, C. Suksaroj, Water Sci. Technol. 65 (2012) 1158.

[141] Q.G. Xie, Taweepreda, W. Musikavong, C. Suksaroj, C., Songklanakarin J. Sci. Technol. 33 (2011) 699.

[142] S.S. Yazdani, R. Gonzalez, Curr. Opin. Biotechnol. 18 (2007) 213.

[143] Y. Nakagawa, Y. Shinmi, S. Koso, K. Tomishige, J. Catal. 272 (2010) 191.

[144] Y. Nakagawa, K. Tomishige, Catalysis Science & Technology 1 (2011) 179.

[145] T. Miyazawa, Y. Kusunoki, K. Kunimori, K. Tomishige, J. Catal. 240 (2006) 213.

[146] A. Konaka, T. Tago, T. Yoshikawa, A. Nakamura, T. Masuda, Appl. Catal. B 146 (2014) 267.

[147] A. Konaka, T. Tago, T. Yoshikawa, H. Shitara, Y. Nakasaka, T. Masuda, Ind. Eng. Chem. Res. 52 (2013) 15509.

[148] M. Behrens, Angew. Chem. Int. Ed. 49 (2010) 2095.

[149] M.I. Zaki, M.A. Hasan, F.A. Al-Sagheer, L. Pasupulety, Colloids and Surfaces a-Physicochemical and Engineering Aspects 190 (2001) 261.

[150] C.-T. Liu, W.T. Lindsay, Journal of Chemical & Engineering Data 15 (1970) 510.

[151] G.B. Zhou, X.H. Tan, Y. Pei, K.N. Fan, M.H. Qiao, B. Sun, B.N. Zong, Chemcatchem 5 (2013) 2425.

[152] W. Li, H. Huang, H. Li, W. Zhang, H. Liu, Langmuir 24 (2008) 8358.

[153] C. Fan, Y.A. Zhu, X.G. Zhou, Z.P. Liu, Catal. Today 160 (2011) 234.

[154] S.H. Zhu, Y.L. Zhu, S.L. Hao, H.Y. Zheng, T. Mo, Y.W. Li, Green Chemistry 14 (2012) 2607.

[155] A.M. Ruppert, K. Weinberg, R. Palkovits, Angewandte Chemie-International Edition 51 (2012) 2564.

[156] K.L. Deutsch, D.G. Lahr, B.H. Shanks, Green Chemistry 14 (2012) 1635.

[157] J. Oh, S. Dash, H. Lee, Green Chemistry 13 (2011) 2004.

[158] S.H. Zhu, X.Q. Gao, Y.L. Zhu, Y.F. Zhu, X.M. Xiang, C.X. Hu, Y.W. Li, Appl. Catal. B 140 (2013) 60.

[159] L. Ma, D.H. He, Top. Catal. 52 (2009) 834.